18, Twelfth Ave
St. Lucia, QLD 4067
Tel. (07) 38713472
31st May 2002

The Dean
Faculty of Engineering
University of Queensland
St. Lucia, QLD 4072

Dear Sir,

In accordance and partial fulfillment of the requirements for the degree of Bachelor of Engineering (Honours) in the division of Electrical Engineering at the University of Queensland, I hereby submit for your consideration this thesis entitled "TEM Horn Antennas for Landmine Detection Applications". This work was performed under the supervision of Dr. Chris Leat.

I declare that all the work submitted in this thesis is my own, except as acknowledged in the text, and have not been previously submitted for a degree at the University of Queensland or any other institution.

Yours sincerely,

Buan Sen Tan

TEM Horn Antennas for Landmine Detection Applications

by

Buan Sen Tan

School of Information Technology and Electrical Engineering
University of Queensland

Submitted for the degree of Bachelor of Engineering (Honours)
in the division of Electrical Engineering
31st May 2002

TEM Horn Antennas for Landmine Detection Applications

by

Buan Sen Tan

Abstract

In recent years, considerable amount of efforts have been put into the research and development of Ground Penetrating Radars (GPR) for landmine detection. The advancement in Ultra-Wideband (UWB) technology paves way for a new category of GPRs, capable of detecting small objects underground. Using an ultra-wide bandwidth, these GPRs are able to provide the depth penetration and resolution required for detection of both metal and plastic objects. Thus, the design of an antenna capable of performing in a wide range of frequencies becomes an important factor in determining the success of the GPR. The purpose of this thesis is to provide a comprehensive analysis on the design and development of an UWB TEM horn antenna. This thesis begins with an introduction of the UWB GPR systems and the important parameters affecting the design of antennas. These concepts provide the essential knowledge needed for the analysis of the design process based on a combination of numerical and empirical methods. The work of this thesis mainly concentrates on three experimental design phases. Each of these phases includes the change in dimensions and added structures, such as the balun and the bell shaped antenna plate. Results from these simulations are continually assessed and each phase sees numerous simulations using different parameters in an attempt to achieve the best overall performance in these antennas. Measured results from the final prototype showed relatively good agreement with its simulations. In addition, results from a field test conducted using a SF-GPR provides a testament to the success of this design. These studies will provide the essential knowledge for future development of TEM horns based on an empirical approach.

Acknowledgements

Special thanks to my supervisor, Dr. Chris Leat for his patience and encouragement throughout the whole course of the project. The completion of this thesis would not be possible without his guidance and the invaluable time spent in explaining important concepts in designing the antenna.

To my family, especially my dearest dad and mum, I would like to say a word of thanks for your constant support and patience throughout all these years. Without your support, I would never have gotten this far.

Finally, I would like to thank those who have helped me throughout the course of the project, especially the guys from the UQ Electrical Engineering workshop, Keith and Wayne for rendering their professional skills to the completion of the prototype. And to Dr. David Lloyd, who spent an entire day setting up the GPR system for the field test.

Contents

List of Figures

List of Tables

Introduction

Introduction to Landmines

Every year, thousands of innocent people are killed or crippled by landmines. Although the 'Ottawa Convention' signed by 84 countries in 1999 prohibits usage, production and transfer of Anti Personnel Landmines, millions of unexploded landmines have already been scattered over many post-war countries. A statement published by the US Department of State [1] website cited:

> *"The 1993 edition of Hidden Killers reported some 65 to 110 million uncleared landmines scattered in 56 countries. The 1994 version of the report stated that as many as 80-110 million antipersonnel mines were scattered in 64 countries. These numbers are merely estimates from military archives dated back into World War I, with many more that were unrecorded."*

The presence of landmines in areas outside combat zones in many post-war countries, made it difficult for people to get back to their prior homes, for fear of getting killed by these unexploded ordnances. Vast areas of land that could be used for agriculture or other industrial interests are wasted due to the presence of landmines. The close proximity of landmines to residential and commercial areas in the post-war countries has a left an adverse effect on the revival of its war-torn economy [2].

Landmines are no longer made only using metals; statistics show that more than 50% of the landmines manufactured are made of plastic [1]. There has been an extensive use of plastic landmines in recent conflicts. These plastic landmines proved to be an obstacle to traditional mine detection techniques using metal detectors. As a result, mine detection technologies called for a revolution, a new technique for detection of both metallic and non-metallic landmines.

Complete clearance of a minefield is required to restore public confidence. Therefore, mine-detection techniques require extremely high detection rates. Although research and development of detection techniques has been going on for years, no single technique is deemed suitable for all de-mining scenarios. Nonetheless, the Ground Penetrating Radar (GPR) has emerged as one of the most promising mine detection technology in the recent years.

Overview of the Ground Penetrating Radar

Researches on detection of underground objects have been an ongoing project in the past decades. The initial development of the Ground Penetrating Radar (GPR) in 1926 by Hülsenbeck was not follow up by any major research until the late 1950s. The need for surveys of underground objects resulted in a revival of the GPR. Since the 1970s, this technology has been widely used in civil engineering sectors. Presently, GPRs are widely used in the location of gas pipes, cables, tunnels, coal layers, etc. Further researches on the applications of GPRs have been conducted in the recent years. The International GPR Conference held every 2 years is evidence of the growing interest in the GPR system. This conference showcases new applications and modeling techniques developed over the recent years. Recent publications include the use of GPR on the Mars Netlander, gold mining operations and profiling of dry valleys in the Antarctica. Soil moisture profiling is also made possible using the GPR's ability to detect variations on dielectric properties [3].

The past decade has seen an enormous advancement in the development of GPR for landmine detection. Its ability to perform accurate classification of both metallic and non-metallic objects buried underground contributed to its success in landmine detection. Unlike classic GPRs discussed above, these GPRs operate in the ultra wideband frequency range, which is required for better classification of small-buried objects, such as landmines. In operation, a classic Ultra-Wideband GPR using air-launched antennas is usually mounted on a mobile unit, scanning a suspected minefield in a lateral direction. Information on the location of the landmines is then made available through signal processing of the echoed signals. Accurate information on the location of the landmine will aid de-miners in clearing the minefields.

The Need for Ultra-Wideband Antenna

The antenna is a critical component of the GPR. It has a huge influence on the overall performance of the entire system. Because of the relatively small dimensions of landmines, the GPR is required to provide good range resolution for optimal detection and classification of these buried objects.

The operating frequency range for GPRs used for landmine detection is often in the range of a few hundreds of Megahertz to a few Gigahertz. With this frequency range, a GPR is able to provide both high range resolution and a good penetration depth. The choice of frequency range is largely dependent on these parameters, which is in turn, dependent on the dimensions and depth of the targeted object.

From the GPR requirements, it is clear that an ultra-wideband antenna is needed to provide the required range resolution. This ultra-wideband antenna is able to provide a consistent performance throughout its operating range of frequencies. One particular category of antennas, known as frequency independent antennas offers extremely high bandwidths, making them the best choice for this application. Among the numerous wideband antennas described in literature, the TEM horn is chosen for the subject of this thesis.

Overview of this Thesis

The main aim of this thesis is to investigate and provide a literature review on the development of the TEM horn prototype used in conjunction with an Ultra-Wideband Ground Penetrating Radar using Synthetic Aperture Radar (SAR) for landmine detection.

This thesis is presented in 7 chapters. Chapter 1 introduces the Ground Penetrating Radar used for landmine detection. This chapter covers its basic operating principles and important parameters related to the development of the TEM horn antenna. Chapter 2 provides information on the fundamentals of antenna design and the properties of frequency independent antennas. This is followed by a literature review on various wideband antennas commonly used in GPR systems. A brief summary of Dr. Bart's PhD thesis on Ultra-Wideband Ground Penetrating Radar (UWB GPR) using a dielectric-filled TEM horn antenna will be included as a reference for this thesis.

Chapter 3 presents a complete analysis on the area of study. The chapter starts with an overview on the design of the TEM horn, followed by its theoretical analysis. The section on analytical theory of the TEM horn provides a comprehensive empirical approach on its analysis along with methods employed in numerical analyses. A technical description on the design methodology of the TEM horn will also be presented. This provides an overview of the entire design process using both numerical and empirical approach. Chapter 4 serves as an extension to the design phases of mentioned in the preceding chapter. Results from simulations and methods used in the process of converging antenna parameters to optimal values are reviewed. The chapter concludes with a summary on the formulation of the final TEM horn design.

The physical construction of the antenna and implications due to its integration with the GPR are discussed in chapter 5. The results from both tests conducted in the anechoic chamber and field are analyzed and a comparison between simulated and measured results will also be presented. A brief evaluation on the entire thesis will be presented in Chapter 6. Chapter 7 concludes with a summary on the thesis and its potential topics for future development.

Chapter 1. The Ground Penetrating Radar

The aim of this chapter is to provide an overview on the basic operation of the Ground Penetrating Radar used for mine detection. This chapter provides detailed definitions on some important parameters used in GPR terminology. Knowledge of these parameters will be essential for the understanding of the design specification of the antenna. This chapter also presents the theory on the ultra-wideband technology employed in this system.

1.1 Ground Penetrating Radar Operating Principles

1.1.1 Basic Operating Theory of a GPR System

The Ground Penetrating Radar works on the same principle as a classic radar system. Electromagnetic (EM) waves propagate through the transmitting antenna towards the ground and an echoed wave results from reflections by the target. Contrasts between dielectric properties of the ground and the buried object result in a reflection of EM waves with different electrical properties. Upon receiving these reflected waves, an identical receiving antenna sends them to a post processing system for analysis.

The electrical properties of the EM waves that are backscattered vary with the dielectric properties in the ground. These electrical properties are namely, relative permittivity,

relative permeability and conductivity. However, not all three parameters provide useful information to the GPR. Conductivity generally affects the penetration depth of the GPR due to absorption of the radar signals in the medium. Soil with high moisture content increases the electrical conductivity, thus decreasing penetration. On the other hand, due to the lack of magnetic content in earth's soil, relative permeability is hardly provides any useful information because it offers little contrast in the radiated EM pulses. Contrastingly, relative permittivity, which corresponds to the dielectric constant of the medium, provides the highest degree of contrast in the reflected wave, thus resulting in good characterization of the ground. Therefore, the contrast in permittivity usually leads to the reflection in the EM pulse.

The GPR's ability to differentiate an object buried underground relies heavily on its operating frequency range. Most applications for GPRs operate with a bandwidth of about 1 GHz. These applications are mainly used for location of large structures, such as gas pipes, underground cables and coal layers. Such applications require good penetration depth as the targeted objects are usually buried deep underground. On the other hand, GPRs used for landmine detection operates with a much higher bandwidth. Higher bandwidth is required for a better range resolution, which is critical for detection of small objects, such as landmines. Thus, the GPR used for landmine detection uses the ultra-wideband technology for higher range resolution, which results in better classification of objects, in the expense of penetration depth.

The backscattered signals received by the receiving antenna typically consist of a series of echoes in the time domain. The first and largest echo usually represents reflection from the air-ground interface, while subsequent echoes may result from reflections from the target or clutter [4]. Clutter is defined as spurious reflections caused by unwanted scattering. Scattering is essential in any radar detection process. Without scattering, no reflection will occur. Unlike clutter, scattering resulting from the target of interest provides information on its geometry and dielectric properties through contrasts in permittivity with the ground.

1.1.2 Classification of GPR systems

Time Domain Impulse GPR System

GPRs are classified into two broad categories; time domain and frequency domain. The first GPRs developed operate in the time domain and have been the dominating technology in this field. The operation principle of a time domain GPR is fairly straightforward. The system sends out an EM pulse and waits for a backscattered echo. The receiving antenna sends this backscattered signal to the post processing system, which processes the signal for contrast in its electrical parameters. This process is shown graphically in Fig 1.1.

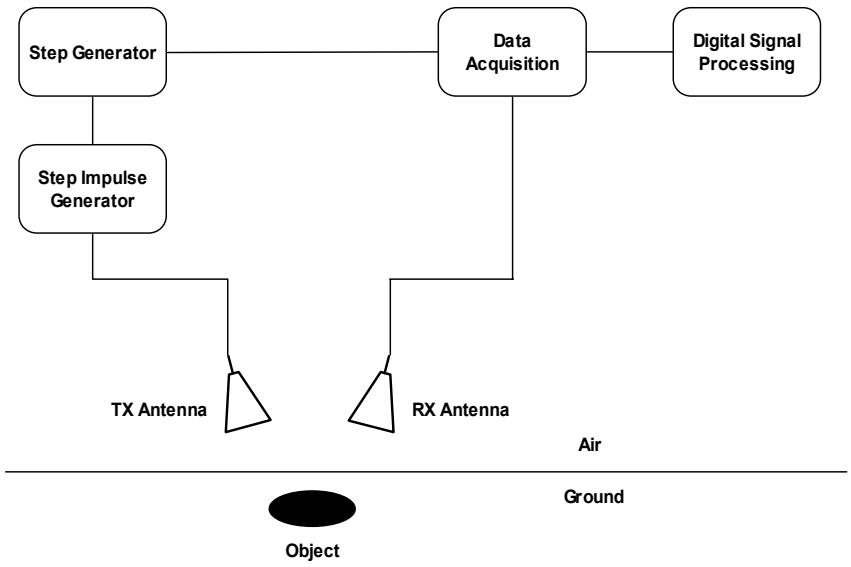

Fig 1.1. Simplified block diagram of a Time-Domain GPR system.

These time domain GPRs are further classified into two categories: the amplitude modulated and carrier free GPRs [4]. Amplitude-modulated GPRs are often used in commercial applications such as road profiling, location of gas pipes and coal mining. The bandwidth requirements for these applications generally range between a few tens of Megahertz to 1GHz. On the other hand, GPRs used for landmine detection have much higher bandwidth requirements. This led to the development of the carrier free GPR, also known as the Ultra-Wideband (UWB) GPR.

Stepped Frequency GPR system

The second category of GPRs operates in the frequency domain and one of the more popular ones is the Stepped Frequency GPR (SF-GPR). The antenna developed in this thesis will be integrated with the SF-GPR that is currently used by the UQ Mining Research Group.

The first of SF-GPRs was developed in 1972 and its results shows improved performance in range over time domain impulse GPRs for a given range resolution, ΔR. This GPR also provide significant improvement in performance in mean processing energy and available bandwidth. But it failed to make an impact in the industry due to its complexity in design and high cost of development. However, technological advancements in wideband and digital signal processing techniques revived the interest in SF-GPRs. Much effort has since been put into its research and development and good results have been obtained from recent developments [9]. Some advantages of the SF-GPRs are [6],

- Higher penetration depth.
- Higher mean transmission power.
- Flexibility in signal processing.
- High range resolution.
- Ability to compensate dispersion effects caused by the medium.
- Ability to efficiently sample received signals with low speed A/D converters.
- Better DSP capabilities for filtering unwanted signals.

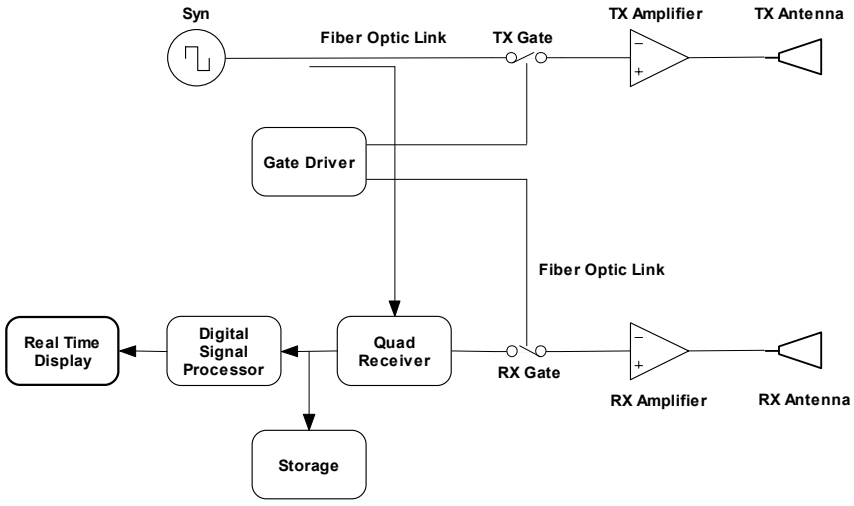

Fig 1.2. Simplified diagram of the Stepped Frequency GPR system.

In operation, the SF-GPR transmits and receives narrowband pulses in series of bursts. Each burst consists of N pulses stepped between its lowest operating frequency, f_L and its highest frequency, f_H in linear increments of Δf . These pulses are generated using frequency synthesizers and radiated towards the targeted area by antennas.

Reflected signals from the ground consist of a change in amplitude and phase, which provides raw information of the target. These signals then undergo pre-processing using a quadraphase modulator (QM) to maintain its coherence. Following that, the signal is sampled and processed by an Inverse Discrete Fourier Transform (IDFT) and put through a series of filtering process. These filtering processes result in an output voltage that resembles a sampled sine wave because of its linear increments. A representation of the target's reflectivity is obtained by converting this signal into its digital equivalent. The Inverse Digital Fourier Transform (IDFT) is then used to convert all the signals to their time domain equivalent after a complete burst is received. This time domain response is known as the target's complex range profile. Variations in the echoed pulse are represented by changes in its amplitude and phase. The phase changes with the range of the target while the amplitude changes are affected by the target's cross section area. Thus, with this information, a 3-D profile of the target can be achieved [6].

1.2 Important parameters for GPR systems

1.2.1 Frequency Band Selection for GPR

Choosing the operating frequency for a GPR is an important step in the successful identification of a target of interest. This ranging signal bandwidth generally defines the range of dimensions of the desired target and to a certain extent, its depth. Frequency band selections usually involve two main parameters: the range resolution (ΔR) and the maximum depth penetration (R_{MAX}). Furthermore, signal attenuation due to ground properties has to be taken into consideration.

Lower Frequency Limit

Attenuation in microwave frequencies in most ground materials varies exponentially with its carrier frequency f_C, and is expressed as,

$$L_{Att} \approx exp(4\pi f_C R / QV_M) \quad \textbf{(1.1)}$$

where Q is the quality factor for a given medium for $f \geq 10MHz$ and R is the range of the target. V_M is the velocity of wave propagation in the medium. From this relationship, it is obvious that a low carrier frequency is needed for minimum attenuation, thus good penetration. This condition generally limits the lower frequency range of the GPR.

Upper Frequency Limit

Range resolution for any radar system is expressed as the minimum distance from which two identical sources can be distinguished using only their distances from the radar itself. It is expressed as,

$$\Delta R \approx V_M / 2(f_H - f_L) = V_M / 2B \quad \textbf{(1.2)}$$

where f_H and f_L represents the highest and lowest frequencies in the ranging signal bandwidth, respectively, and B is the bandwidth. As seen in (1.2), a high range resolution required in the GPR system leads to a high upper frequency limit. As a result, a GPR with low carrier frequency limit due to ground attenuation and high range resolution leads to the utilization of an ultra-wide bandwidth.

Ranging Signal Bandwidth

The ranging signal bandwidth of the GPR is commonly characterized by its fractional bandwidth,

$$B_F = 2(f_H - f_L)/(f_H + f_L) \quad \textbf{(1.3)}$$

A common definition states that a radar is considered ultra-wideband if its fractional bandwidth is greater than 0.25. However, this definition made no distinction between a GPR and a UWB GPR. With this definition, most GPRs would have been classified as ultra-wideband. Thus, a more specific definition states that a fractional bandwidth greater than 100% is required for a GPR to be considered ultra-wideband.

Selected Frequency Band for UWB GPR system

The frequency band for the UWB GPR system sets the specification for the design of the antenna. This frequency range is chosen such that it is within the range of the antennas presently realizable. Most practical wideband antennas are able to handle bandwidths up to a few Gigahertz. The range resolution determines the minimum distance where two objects can be discriminated by the GPR at a standoff distance. Thus, a relatively high upper frequency of 6 GHz is chosen. Since there is a lack of requirement for deep penetration in landmine detection, a relatively high lower cut off frequency at 800 MHz is used.

1.2.2 Definition of Terms used in UWB GPR Systems

Range Resolution in UWB GPR Systems

As seen from the preceding section, the range resolution is inversely proportional to the ranging signal bandwidth of the GPR. Consequently, a good range resolution is readily achievable in a UWB system. The resolution of two signals can be obtained by comparison between their sinc functions in the time domain. However, backscattered signals from the ground suffer exponential attenuation (1.1), which results in distortions. Such distortions generally lead to a decrease in range resolution. Furthermore, Cherniakov and Donskoi [5] show that the width of the impulse response depends on the absolute bandwidth and ground attenuation properties, not f_H or f_L. It is also shown that signals at high attenuating medium suffer from serious pulse broadening, even with extremely wide bandwidth.

Penetration

As defined in the previous section, attenuation of EM waves traveling in the ground is an exponential function of the carrier frequency. This condition limits the effectiveness of the conventional GPR for detection of small objects buried deep underground, especially in high attenuating mediums. Fortunately, GPRs used for landmine detection generally do not need a good penetration depth, as landmines are often laid shallow. This gives a room for trade off in improving range resolution in the expense of penetration. A penetration depth of 20cm is usually sufficient for such purposes [4]. The maximum depth of penetration for a GPR, R_{MAX}, is given by [6],

$$R_{MAX} = \left[\frac{P_T G_T G_R c^2 \sigma_T}{(4\pi)^3 f^2 S_{\min} L} \right]^{\frac{1}{P}} \tag{1.4}$$

where P_T is the transmitted power, G_T and G_R are the transmitter and receiver gains of the antenna respectively. σ_T is the cross section are of the radar, expressed in m^2

and $S_{\min}$ is the required minimum detectable signal in Watts. The value of L defines the power reduction factor due to absorption, while P is a value between 2 to 4, depending on the target.

1.3 Synthetic Aperture Radar

A radar's antenna capability to detect object is often judged by the size of its aperture. With a larger antenna, one can generally obtain more information on an object, thus providing better resolution. However, these antennas are not practical a due to its size and cost of construction. The invention of the Synthetic Aperture Radar (SAR) provides the means of simulating large aperture using an antenna with a fraction of its aperture.

Fig 1.3. B-scans of several objects above the ground using a SF-GPR (SAR) with double ridged horn antennas. The hyperbolic shapes are the result of averaged pulses over a synthetic aperture.

The SAR uses advanced Digital Signal Processing (DSP) techniques to simulate a large aperture by moving the radar in a direction perpendicular to the object. By transmitting many pulses as the radar is moved, a single object may be detected many times and the reflected pulses are averaged over distance. For landmine detection, the detected objects are shown in a hyperbolic shape as the radar is moved across the object (shown in Fig 1.3). Through this process, the SAR is able to eliminate any noises, which are

constant throughout the entire detection process, such as cross coupling between the transmitting and receiving antennas.

In realizing the full potential of the SAR, an antenna with a wide beamwidth is required. A wide beam antenna provides a larger detection coverage as the antenna is moved across the object, which means the object is averaged over a larger number of reflected pulses, thus increasing the accuracy of the results.

1.4 Summary

The GPR is no ordinary radar, it possess the ability to penetrate ground for the detection of underground objects. In the past, this is only used for detecting large objects. However, recent advancement in ultra-wideband technology drove researchers into developing high resolution GPRs, which are able to discriminate objects with small dimensions, such as landmines. Two basic models of GPRs are also presented. The SF-GPR, which will be used in the implementation of the UWB antenna, has been briefly discussed as field results in the later chapters will require some understanding of its operation. The range resolution and depth penetration determines the upper and lower frequency limits. A good understanding of these parameters will aid in the design and analysis of the antenna in the succeeding chapters.

Chapter 2. Ultra-Wideband Antennas

Ultra-wideband antennas are found in applications with requirements for high bandwidth, such as radar systems. These antennas often require constant performance over several Gigahertz, thus commonly termed “frequency independent”. The aim of this chapter is to provide an analysis on the characteristic of these frequency independent antennas. Various wideband antennas will be investigated in literature. This chapter will also provide an overview on some of the important parameters associated to wideband antennas. A brief summary on Dr. Scheer’s UWB GPR System using TEM Horns will be presented at the end of the chapter.

2.1 The Frequency Independent Antenna

2.1.1 Basic Principles of a Frequency Independent Antenna

Frequency independence in antennas is an important factor for achieving optimal performance over wide range of frequencies. This is especially important for the design of a wideband antenna. An antenna can be defined as frequency independent if it exhibits constant performance, invariant to the change in scale, which is inversely proportional to the change in frequency [7]. That is, when dimensions of an antenna are doubled and its frequency halved, its performance, such as gain, impedance, beamwidth

etc., remain unchanged. This condition holds when the antenna is of infinite length and constructed using perfect conductors and dielectrics. If an antenna is completely determined by angles, such as a biconical antenna, the antenna will satisfy the above condition. However, for practical usage, the biconical antenna, which is theoretically infinite, has to be truncated. As a result to this change in geometry, the performance of the truncated antenna will not produce exact results as its infinite counterpart. Although the truncation principle defines that similar results from the antenna are required for both infinite structure and its truncated equivalent; it also imply that current *I,* approaches zero away from the terminals and that the architecture of the finite structure approaches its physical limit with increasing frequency [7]. Therefore, the truncation principle holds for any practical frequency independent antenna.

Practical frequency independent antennas only produce relatively constant performance over a finite range of frequencies. The frequency limits for these antennas generally depend on its dimensions. The maximum dimension of the antenna sets the limit of the lower cut-off frequency. On the other hand, the higher cut-off frequency is determined by the preciseness of the construction on its feedpoint.

The curvature in the structure of a frequency independent antenna provides means for attenuating the current towards the edge of the structure. The curve is essential in directing the current flow towards the radial direction. The magnitude of this curvature has been proved to increase the attenuation of current [7].

2.1.2 Parameters used in Characterizing Antennas

Antennas are generally described using parameters such as gain, radiation pattern, directivity, impedance and beamwidth. In addition, this section will cover topics on far field and near field measurements.

Gain

Gain is commonly used in describing the efficiency and directional capabilities of an antenna. There are several ways of describing the gain of an antenna, all of which will be covered in this section.

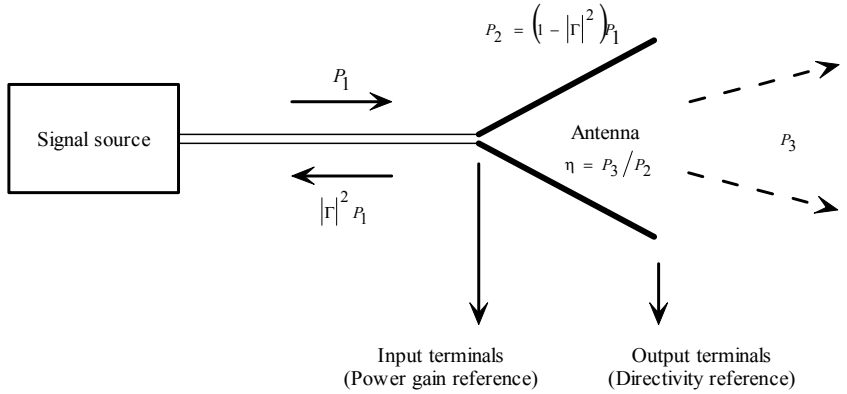

Fig 2.1. Schematic of a simple transmitting antenna and its reference points for gain and directivity.

A schematic of a transmitting antenna is shown in Fig 2.1 to help illustrate the definition of gain. The transmitting antenna is connected to the signal source with a (time averaged) power P_1, via a transmission line. Upon reaching the feedpoint of the antenna, the power incident from the source is reduced to P_2, where

$$P_2 = \left(1 - |\Gamma|^2\right)P_1 \tag{2.1}$$

where $|\Gamma|^2$ is the power reflection coefficient. Due to finite conductivity of the antenna, the radiated power P_3, is a fraction of its input, P_2. This fraction is known as the radiation efficiency.

$$\eta = P_3/P_2 \tag{2.2}$$

The gain of an antenna can be generally defined as the ratio of its radiation intensity in a particular direction, to a reference power. The magnitude of these reference powers

are expressed as the power emitted from an isotropic antenna. An isotropic antenna by definition radiates and receives radio waves equally at all directions. Thus, the radiation intensity of these references is taken as the power divided by 4π.

$$G(z) = \frac{4\pi}{P_n} P_o = 4\pi \frac{intensity\ of\ the\ antenna\ in\ direction\ z}{reference\ power} \tag{2.3}$$

where P_n is the reference power. Three definitions of gain are usually used in antenna characterization. They depend on the reference power, as indicated in Fig 2.1. These common definitions are,

- Realized gain $G_1(z)$ where $P_n = P_1 = Power\ incident\ from\ signal\ source.$
- Power gain $G_2(z)$ where $P_n = P_2 = Power\ at\ feedpoint\ of\ the\ antenna.$
- Directivity $D(k)$ where $P_n = P_3 = Power\ radiated\ by\ the\ antenna.$

The power gain, sometimes known as the relative gain will be used in measurements later in this thesis. And it is expressed as,

$$Gain = 4\pi \frac{U(\theta,\phi)}{P_{in}(isotropic)} \tag{2.4}$$

$$= \frac{intensity\ of\ the\ antenna}{intensity\ of\ an\ isotropic\ radiator\ with\ same\ input\ power}$$

Gain has no dimensions but it is often expressed in its decibel (dB) value. Gain with respect to an isotropic radiator is sometimes expressed in dBi. By default, the power gain is taken from the direction with maximum radiation.

Directivity

Directivity of an antenna is defined as the ratio of its radiation intensity in a specified direction to its averaged radiation intensity in all directions. The average radiation intensity can be taken as the total radiation power divided by 4π. This is expressed in the following equation,

$$D = \frac{U}{U_o} = 4\pi \frac{U}{P_{rad}} \tag{2.5}$$

where U is the maximum radiation intensity and U_o is the radiation intensity of an isotropic source, which is the total power radiated divided by 4π. By default, the direction with maximum radiation intensity is taken as its referenced direction. From Fig 2.1, it can be seen that directivity is taken as gain, referenced from the point where the waves propagates into free space.

Radiation Pattern

The figure shown in Fig 2.2 shows a three-dimensional view of a classic radiation pattern for an antenna seen from its far field. The radiation pattern is used as a visualization tool for antenna analysis and is defined as its variation in field intensity as an angular function with its axis.

The pattern radiation in Fig 2.2 shows several lobes originating from the phase center of the antenna. These lobes are contains radiation energy that are stronger than the regions bounded by it. The main lobe shown in the figure indicates the direction where maximum radiation occurs, while the sidelobes, sometimes referred to as minor lobes are generally radiation in undesired directions. The back lobe is a minor lobe located at the back of the antenna or more specifically, radiation that occurs at a direction opposite to the main lobe. Each lobe is bounded by nulls, which is defined as the area with minimum radiation relative to the maximum radiation in its referenced lobe.

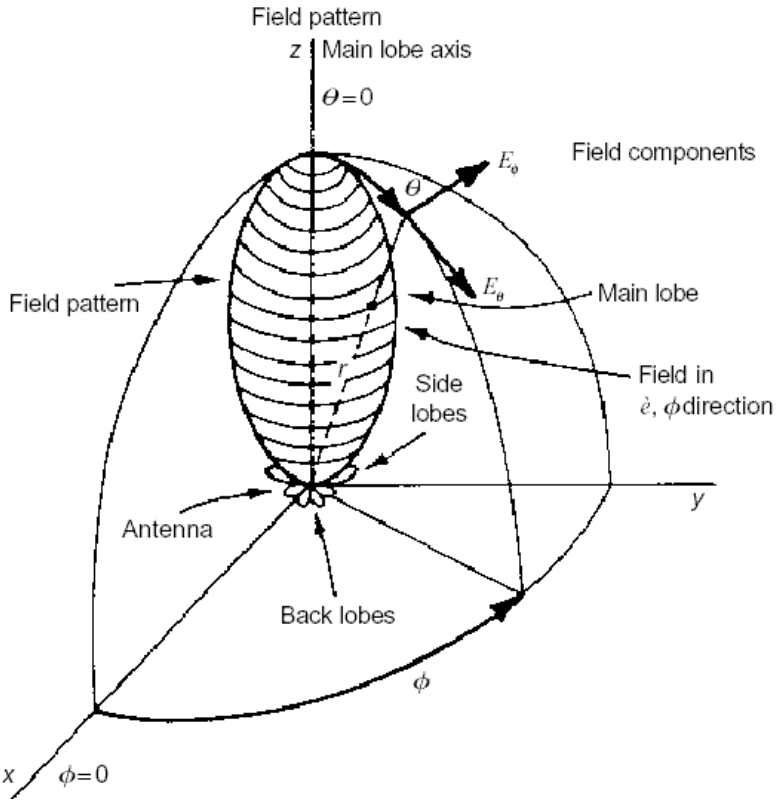

Fig 2.2. 3-D view of a common radiation pattern [26].

Minor lobes are undesirable and thus, have to be avoided or suppressed through careful design of the antenna. Typical ratios of 20dB or more between the main lobe and the sidelobes are achieved in antenna applications. Radar applications generally require high ratios between the main lobe and the sidelobes to avoid false target indications.

Field Regions

The antenna is often assumed to be radiating in infinite free space. This free space can be divided into three regions, known as, (a) reactive near-field, (b) radiating near-field and (c) far-field (Fraunhofer) regions. These regions are used to define the regions in which an antenna is to be characterized, depending on the parameters of interest.

The reactive-near field is defined as the region from the antenna where reactive fields dominate the radiating field. The distance between the surfaces of the antenna to the

outer boundary is commonly taken as $R = 0.62\sqrt{D^3/\lambda}$ for most antennas. The wavelength is denoted by λ and the largest dimension of the antenna by *D*.

The radiating near field region, which exists between the reactive near-field and the far field regions, is defined as the immediate zone where radiating field begins to dominate. However, its dominance does not go beyond the extent of defining independence between the angular distribution of the radiating field and its distance from the antenna (*r)*. Thus, the usual antenna pattern can not be accurately obtained in this region. Its inner and outer boundaries are taken as $R \geq 0.62\sqrt{D^3/\lambda}$ and $R < 2D^2/\lambda$ respectively.

Defined as the region beyond the reactive/radiating regions, the far-field (Fraunhofer) region is described as the field region where the angular distribution of a field is independent of its distance from the antenna (*r*). Thus, the reactive fields in this region are deemed negligible. The inner boundary of this region is taken as $R \geq 2D^2/\lambda$. This region is commonly used for obtaining radiation patterns of an antenna.

Beamwidth

The beamwidth is a measurement on the directiveness of a directional antenna. It is defined as the angle between two half-power (-3dB) points on either side of the main lobe. The antenna's beamwidth is a function of gain, wavelength and its aperture. To aid the understanding of the dependence of beamwidth on the wavelength and its aperture, consider a segment of the antenna's aperture shown in Fig. 2.3; maximum radiation is produced in the direction when the EM waves are in phase $(\theta = 0)$. On the other hand, nulls are produced when there is a phase difference of $\lambda/2$ between each wavefront corresponding to the points A to C. When viewed from its far-field, these points interfere with their adjacent wavefronts destructively to produce a null in a particular direction, normal to its boresight, denoted by θ. The first null in the radiation pattern is thus given by,

$$\sin\theta = \frac{\lambda}{L} \tag{2.6}$$

where λ is the wavelength and L is the azimuth/elevation length of the antenna's aperture. Therefore, it can be seen that the first null beamwidth is 2θ. The general relationship between the beamwidth, gain, wavelength and its aperture can be defined through the gain of an aperture antenna, G, defined as,

$$G = \eta \frac{30{,}000}{BW_\theta BW_\phi (deg)} = \eta \frac{4\pi L_{az} L_{el}}{\lambda^2} = \eta \frac{4\pi A_{eff}}{\lambda^2} \tag{2.7}$$

where BW_ϕ and BW_θ are the beamwidths in the azimuth and elevation planes respectively. The effective area of the aperture is denoted by A_{eff} and is the multiplication of both azimuth length L_{az} and elevation length L_{el} of the aperture.

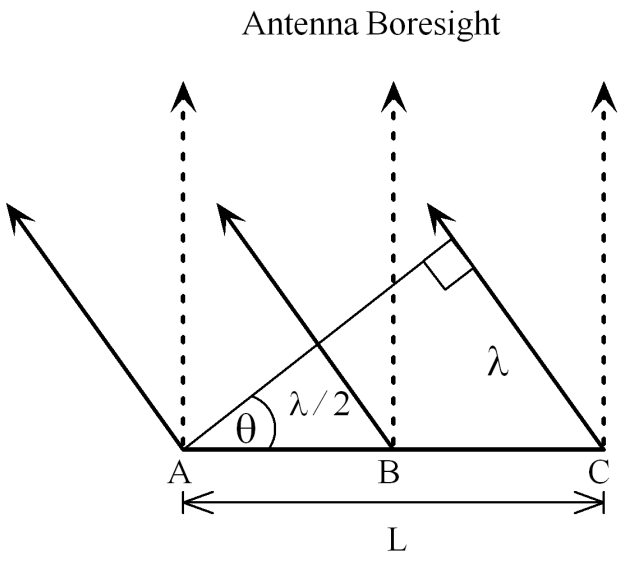

Fig 2.3. Relationship between beamwidth and wavelength.

Impedance

The antenna impedance often relates the transfer of power from the generator to the antenna for a transmitting antenna and conversely, the transfer of power from the antenna to the load when used as a receiver. Maximum power transfer can only be achieved when the impedance of the antenna is matched to those of the load, which requires the antenna impedance to be the complex conjugate of the load impedance.

For a UWB antenna used for GPR application, an impedance mismatch between the antenna and its load results in serious ringing problems. In radar systems, ringing usually leads to false indication of targets distortion of signals. Impedance matching has been particularly difficult in UWB antennas, since its impedance has to remain constant over a wide range of frequency. However, with careful design and employing appropriate mechanisms, such as resistive loading [8], a good match can be achieved over a wide range of frequency. Practical results with a reflection coefficient of -10dB or lower are generally well accepted for most applications. For a 50Ω load, this means an impedance value between 40Ω and 60Ω.

2.2 Different Types of Wideband Antennas

2.2.1 Air-filled TEM Horn Antenna

The need for a wideband antenna with non-dispersive characteristic for UWB GPRs led to the development of a TEM horn. Furthermore, the TEM horn provides higher gain and directivity through its end-fire traveling wave structure. Since the TEM horn is completely characterized by shapes and angles, it fulfills the criteria of a frequency independent antenna. In addition, results have verified the truncation principle by showing a decrease in current distribution away from its input terminals [9].

The basic structure of the TEM horn is fairly simple, with two isosceles triangular plates separated by an elevation angle. The combination of the azimuth and elevation

angles determines the impedance of the antenna. The real part of the impedance has to be maintained at a matched over the desired frequency range to ensure minimum ringing within the antenna. The lower cut-off frequency of the antenna generally puts a minimum limit on its length. This length must be at least one half wavelength of the lower cut-off frequency. As a result, the antenna is usually not practical for conventional GPR systems for due to its excessive size requirements at low frequencies.

The typical TEM horn is able to achieve a bandwidth of about 4GHz – 8GHz with relatively good reflection coefficient. Despite its good performance over a large bandwidth, various modifications on its design have been suggested to overcome impedance matching problems and reducing dimensions. The more notable ones are the tapered TEM horn and the dielectric TEM horn.

2.2.2 Vivaldi Antennas

The Vivaldi antenna, presented by Gibson [10] in 1979 paves a new channel for the development of extremely wideband frequency independent antennas. Being completely realized in microstrips, this antenna provides easy integration with other microstrip circuits. Bandwidths of up to 800GHz have been reported when used as a single traveling wave antenna [12]. However, its bandwidth reduces to about 2GHz – 5GHZ when employed in phased arrays for large aperture antennas.

The structure of the Vivaldi antenna resembles that of a 2-D tapered horn, realized on microstrips. Its wave-guiding structure, such as slotline of microstrips, increases exponentially towards the direction of propagation, thus forming a flared out structure at its output terminals. Microstrips are usually used as the feed to the input terminals, although recent studies show that a bandwidth of 10:1 is achievable using coax-to-slotline transition. Very often, the method of excitation sets the limits of the antenna's bandwidth, rather the geometrical dimensions of its flare.

Generally, the Vivaldi antenna operates in very high frequencies ranging from1GHz - 18GHz. Their high bandwidth and simplicity in construction have made them popular choices for many wideband applications. The downside of this antenna is its weak structure, which requires a fair amount of support if the dimensions are large. It is also subjected to dispersions [12].

2.2.3 Double Ridged Horns

Horn antennas are commonly used in microwave applications due to its simplicity in construction, ease of excitation, high gain and preferred overall performance. However, due to its limited bandwidth, the horn is unsuitable for wideband applications such as the UWB GPR. This led to the development of the Double Ridged Horn, shown in Fig 2.6.

Fig 2.4. The double ridged horn antenna.

The bandwidth of a rectangular horn is determined by taking the difference between the cut-off of the dominant mode, TE_{10} and the cut-off of its next highest mode. This bandwidth is often limited by its lowest cut-off frequency. Assuming the dimensions of the horn remain unchanged, this bandwidth limit can be eliminated by introducing

ridges inside the horn, as indicated in Fig 2.6. These ridges act like parallel-plate waveguides, which allows TEM mode propagation within the horn. As a result, the frequency of the dominant TE_{10} mode reduces towards a zero frequency value when the ridges converge towards the feedpoint. Contrastingly, the frequency of the next highest mode increases as the ridges converge towards the feedpoint. This phenomenon effectively increases the bandwidth of the antenna.

The loading of ridges in the horn poses another problem in its design: impedance. The impedance of the ridge loaded horn generally limits its usable bandwidth, due to its dependence on frequency. Thus, a compromise usually exists between a good impedance match and a large bandwidth.

2.2.4 Spiral Antennas

The spiral antenna, sometimes also known as the log-spiral antenna or equiangular spiral antenna, is shown in Fig 2.7. This antenna obeys the truncation principle of frequency independent antennas. Its structure is completely defined by angles, thus remains "effectively infinite" when truncated.

Fig 2.5. A typical wideband spiral antenna.

To achieve an equiangular structure, the angle between the tangent of the curve and the distance from the center of the spiral to the point where the tangent is taken, has to be constant throughout the structure. A change in wavelength, which corresponds to a change its radial angle, ϕ_0, is thus equivalent to a rotation if the spiral structure, with

the shape remaining exactly the same. Therefore, the antenna is said to be independent of frequency.

To drive the antenna, a source is connected at the origin of a log-spiral with four spirals. Currents are found to be at its maximum at regions when its radius, $r \cong \lambda/2$ and declines rapidly after that. Therefore, a practical antenna that is truncated at points corresponding to $r \cong \lambda$ will still be "effectively infinite" based on the truncation principle.

The size of the antenna, more specifically, its overall radius, determines the lower frequency limit. On the other hand, its higher frequency limit is determined by the feed of the structure. The antenna exhibits a bi-directional radiation pattern with a 3-dB beamwidth of about 90°.

2.2.5 Vee-Dipoles

Linear Dipoles are essentially narrowband antennas; however, the bandwidth of such antennas can be increased through distributed resistive loading, resulting in utilization of a very wide bandwidth. Unfortunately, dipoles lack the directivity needed in applications such as the GPR. Thus, the Vee-Dipole is introduced. With its enhanced directiveness, the Vee-Dipole has been developed for use in GPRs for mine-detection.

Its design is fairly simple, with two cylindrical arms of length *h* and radius *a*, separated at an interior angle α. The interior angle, which determines the geometrical "aperture" of the antenna is a function of the electrical length of each arm, h/λ. For proper operation, this "aperture" must be larger than the dimensions of the target in order to provide contrasts between the target and its background. Input impedances of the Vee-Dipoles are highly dependent on its geometry and methods of excitation. As a result, feedpoint matching could be difficult [13].

2.2.6 Horn-Fed Bow-Tie Antennas

The Horn-Fed Bowtie antenna was developed to counter disadvantages in most GPR antenna, such as low directivity, ringing, unstable input impedance and radio frequency interference (RFI). This antenna is developed through modifications on a basic bowtie antenna used in GPR applications. A bowtie antenna causes a fairly high amount of ringing due to impedance mismatch at its feed. Matching the impedances between the feed and the cable is hindered by the fact that the source of the bow-tie is in close proximity with the ground. Moreover, due to its radiation patterns, the bow-tie is very sensitive to RFI and other objects in the space directly opposite its main direction (in this case, the ground). This led to the development of the Horn-Fed Bowtie antenna.

The basic structure of the Horn-Fed Bowtie consists of a dielectric filled TEM horn and a bow-tie antenna at its aperture. The transition from the TEM horn to the bowtie is tapered to avoid sudden changes in the impedance of the antenna. This dielectric filled TEM horn essentially functions as an impedance matching section of the antenna. With the addition of this horn, the feed is also moved away from the ground, thus easing its feedpoint match. Dielectric filling with permittivity close to ground is added to the horn to improve low frequency response and decreases RFI on the bowtie.

Results from this antenna have shown significant improvements in ringing over the bowtie, thus improving its overall sensitivity. A wider bandwidth is also achieved with this model [14]. However, this antenna is designed for use in applications requiring close proximity between the antenna and the ground.

2.2.7 Ultra-Wideband Microstrip Quasi-Horn Antennas

This newly developed microstrip based antenna by Nguyen *et al.* [15] departs from the traditional design of a TEM horn. Being completely realized on microstrip line, the antenna requires no transition or balun at its input. Furthermore, microstrip circuits can be fabricated together with the antenna through a photolithographic process.

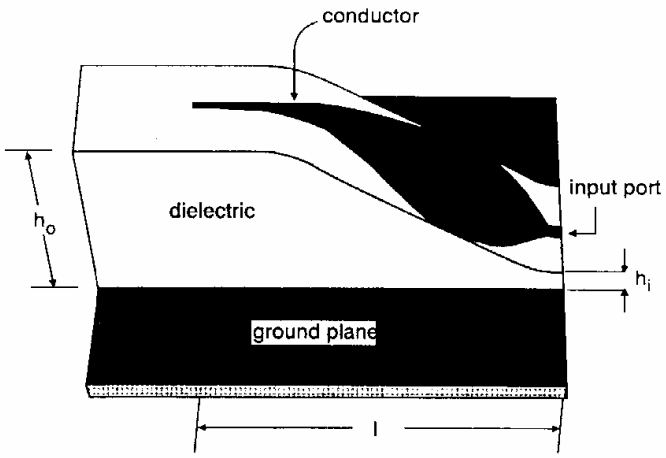

Fig. 2.6. Microstrip quasi-horn antenna

The shape of the microstrip resembles that of a TEM horn, tapered to match the impedance at free space. The antenna is designed in such a way that both transmitter and receiver are separated by only a ground plane, with both microstrips lifted above the ground plane by a dielectric (eg. foam) shaped in a particular way as illustrated in Fig 2.8. This common ground plane acts as a shield between both microstrip quasi-horn antennas, resulting in a high isolation between them [15].

This new design achieved relatively high gain at frequencies from 2.6GHz to 18GHz. Despite its advantages, the antenna exhibits large gain variation, with relatively low gain at the low frequency end [15]. Unfortunately, due to insufficient information on the development of this antenna, this design only serves as a reference for evaluative purposes.

2.3 Dielectric-Filled TEM Horns by Dr. Bart Scheers

This section presents a summary of Dr. Scheers's PhD thesis on UWB GPR for landmine detection. In his thesis, Dr. Bart includes the formulation of both air-filled and dielectric-filled TEM horn. However, the design of the air-filled TEM horn is aimed at achieving an impedance of 80Ω instead of 50Ω used for matching the coaxial feed. The reason behind this particular choice of impedance value is due to the

expected decrease in impedance due to dielectric filling for the design of the dielectric-filled TEM horn.

Filling the TEM horn with dielectric introduces several changes to its propagation characteristics. Firstly, the speed of wave propagation within the horn is reduced by a factor of $\sqrt{\varepsilon_r}$, which in turn increases its electrical length by the same factor. As a result of the decrease in propagation speed, the length of the TEM horn, which is dependent on its wavelength, is reduced by the same factor. Furthermore, the impedance of the antenna is also reduced by $\sqrt{\varepsilon_{r,eff}}$ [4]. If the impedance of the air-filled TEM horn is used, this reduction in impedance will allow further increase in its elevation angle to compensate its effects, thus resulting in a narrower beamwidth. In this thesis, the dielectric-filled TEM horn is preferred over its air-filled equivalent due to its reduced physical dimensions and improved directivity. However, his claim on an increase in directivity over the air-filled horn was refuted by Leat [16] who suggested that directivity is dependent on the wavelength in the propagating medium instead of the wavelength within the antenna.

Despite the advantages of the dielectric filled TEM horn over its air-filled counterpart, there are foreseen problems on its application as an air-launched GPR antenna. The dielectric horn is designed for a system that has the antenna operating in close proximity to the ground. Thus, by matching the dielectric between the antenna plates and the ground would ensure a smooth transition of EM waves between the antenna and the ground. On the other hand, its performance as an air-launched GPR antenna would cause a significant amount of reflection at the aperture when the EM waves make a transition from the dielectric to free space.

2.4 Review and Conclusions

The above literature review describes various wideband antennas that have been developed to be used with GPR systems. However, not all of them are suitable for use

in a UWB GPR for de-mining operations. In this UWB GPR system, its antenna has to satisfy several practical requirements listed below,

1. The antenna must be able to radiate or receive fast electromagnetic transients within a spectrum of 800MHz and 6GHz, which is the –3dB gain bandwidth.
2. The antenna should have relatively high directivity and achieve penetration depth of at least 20 cm in lossy soil.
3. The construction of the antenna must be strong and durable to suit its operation in rough terrain.
4. The antenna is to be connected to a 50Ω coaxial feed and has to be adequately matched at its feedpoint to avoid problems due to reflection.

This set of specification narrows down the choice to both the air-filled and dielectric-filled TEM horns due to their realizable bandwidths and high directivity. However, the UWB GPR is an air-launched unit, which has the antenna mounted on a mobile unit, with the antenna generally facing the horizontal direction. Clearly, the TEM horn with dielectric filling will not result in smoother transition of EM waves between the antenna and the ground by matching their dielectric properties. Therefore, the air-filled TEM horn is chosen as the design for this thesis.

2.5 Summary

A frequency independent antenna is defined as an antenna that exhibits constant performance with frequency. However, practical frequency independent antennas operate over a finite range of frequencies, with variations in its antenna parameters such as gain, radiation patterns and impedance. These common antenna parameters are described in this chapter will be used extensively in the design of the TEM horn. A literature review of some commonly used UWB antennas, reveal that the air-filled TEM horn is best suited for this UWB GPR system used for landmine detection.

Chapter 3. The TEM Horn

3.1 Design Brief of a TEM Horn

From the literature review of the previous chapter, the TEM horn has been chosen as the design for the UWB GPR system. Two of these identical TEM horns will be designed and constructed to be used in the UWB SF-GPR system from the UQ Mining Research Group.

Due to its frequency independent characteristics, parameters such as gain and radiation patterns generally do not vary much over a wide range of frequency. That leaves the impedance as the only parameter that affects the performance of the antenna. The impedance here means the impedance response in frequency domain and the term impedance frequency response will be used throughout this thesis. In order to avoid ringing in the antenna, a good match between the impedance frequency response and the impedance with the input coaxial cable is required. Reflections occur when there is a mismatch within its operating frequency range, resulting in ringing within the antenna.

In our study, the TEM horn will be designed based on a set of dimensions obtained through theoretical calculations. Through experimentation and intuitive reasoning, a series of iterations on dimensional changes on the antenna will be simulated in a software simulation package to achieve the desired performance.

3.2 Analytic Theory of the TEM Horn

3.2.1 Ultra-Wideband Characteristic of the TEM Horn

The performance of the TEM horn is defined as frequency independent as it satisfies the criterion of a frequency independent antenna, which states that an antenna is defined as being frequency independent if its performance can be fully characterized by its shapes and angles. Furthermore, it also satisfies the truncation principle, thus realizing its potential as an ultra-wideband antenna.

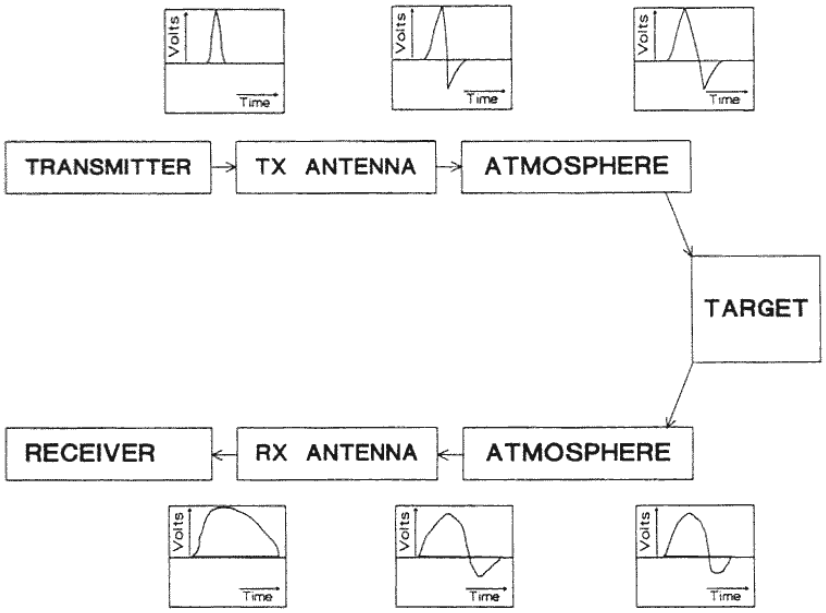

Fig 3.1. Block diagram of the object detection process and the effects of each stage on the transmitted pulse.

The study on UWB TEM horns requires thinking beyond those of conventional antenna analysis. Modeling and analysis of these antennas are not easily achievable through conventional antenna equations. Due to their extreme wide bandwidths, these antennas generally transmit non-sinusoidal wave signals, also known as impulse radiation. The transient signal conditions found in impulse waveforms changes with time, thus, it is easier to characterize such antennas in the time domain. The path taken by the

transmitted impulse signal from the transmitter to its receiver generates a huge amount of change in the signal shown in Fig 3.1. Each stage acts like a filter and their changes are characterized by their impulse response. The radar's ability to pick up a target will be directly dependent on changes incurred in these filters. Since there is little one can do to the impulse response of atmosphere-to-ground interface, all efforts will be placed on preserving the integrity of the transmitted pulse through the TEM horn.

3.2.2 Analysis of a Basic TEM Horn Design

The basic structure of the TEM horn consists of triangular conductive plates, separated by an elevation angle, essentially forming a 3-dimension "V" shape. Its feedpoint is located at the narrowest point between the two plates and its end-fire structure results in a directive antenna with relatively high gain [17]. The TEM horn can be seen as a parallel plate transmission line. Thus, by proper choice of dimensions and methods of excitation, the antenna can be designed to transmit only using TEM mode. In the pure TEM mode, the velocities of all frequency components are constant, which means that all the frequency components generated at its feedpoint will arrive at the aperture at the same time, giving the antenna a non-dispersive characteristic. However, at high frequencies, higher modes starts to appear, thus reducing the performance of the antenna.

Owing to its frequency independent characteristic, the operating frequency range, input impedance and aperture size generally determines the dimensions of the TEM horn. The three main parameters are given by,

- L = Length of the antenna plates at its boresight.
- α = The azimuth half angle of the antenna plates
- β = The elevation half angle between the antenna plates

The length of the antenna plates determines the lowest cut off frequency of the antenna. This length must be at least one half the wavelength of the corresponding frequency. Although the TEM horn is said to be radiating TEM waves, it is capable of supporting

higher modes with suitable dimensions and excitation. In our purpose however, the higher modes are suppressed to avoid effects of dispersion. The higher cut off frequency for a TEM horn-like structure is given by,

$$\lambda_{cutoff} = \frac{2 \cdot B}{n} \tag{3.1}$$

where B is the separation between the plates and n is the mode number of the corresponding TE and TE modes. From (3.1), the highest cut off frequency is inversely proportional to the separation between the plates for a given mode. In practice, higher modes exist and often limit the performance at higher frequencies. Therefore, to achieve a higher cut off frequency, the separation between the plates has to be at its minimum, which corresponds to the separation at its feedpoint. The preciseness on the construction of the feedpoint will thus affect its performance at the higher frequencies.

The azimuth and elevation angles of the horn define the impedance of the antenna. To illustrate this relationship, the antenna is seen as a series of parallel transmission line, with flared dimensions at its aperture. Thus, an approximate analysis on its impedance performance can be achieved using microstrip theory. As can be seen from Fig 3.2 the TEM horn is symmetrical about its x-plane. This model can be simplified by replacing an infinite ground plane on the x-plane. The resulting antenna is formed by the top half of the TEM horn and the infinite ground plane, separated by half the elevation angle of the original horn. With the infinite ground plane, the top plate of the TEM horn casts an exact image on the other side of the x-plane, effectively acting as a TEM horn. This "TEM horn" is then divided into infinitely thin segments. From microstrip theory, these segments are seen as a series of microstrips filled with free-space, each with different width and height corresponding to the characteristic impedance as shown in Fig 3.2. Thus, constant impedance throughout the entire length of the antenna can be achieved by keeping the width-height ratio *(w/h)* constant.

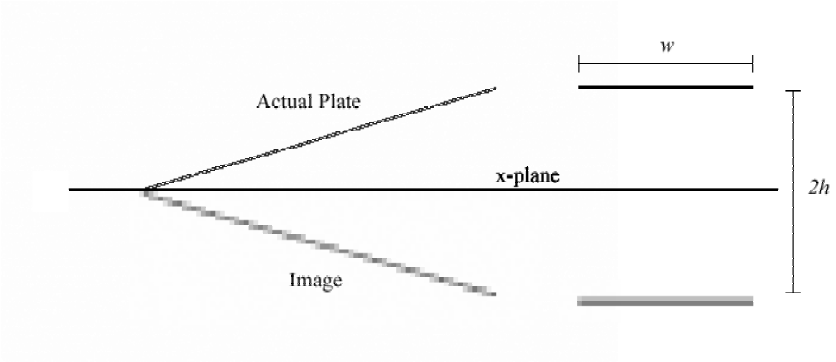

Fig 3.2. Creating a TEM horn using an infinite ground plane and defining its *w/h* relationship.

Maintaining constant impedance throughout the operating bandwidth of the antenna is critically important as a mismatch will cause severe signal degradation due to ringing. Ringing can result from mismatches within the antenna or at any abrupt changes in the transmission medium, such as the antenna-to-free-space interface. When there is a mismatch within the horn, a fraction of the EM wave will be reflected near its aperture back towards the feedpoint, which will in turn reflect a fraction of the wave back towards the aperture. This resonant behavior, if occurred at a large magnitude, will cause severe distortion in the transmitted impulse signal. As a result, the signal received from the receiving antenna may not give an accurate representation of the detected object. Various schemes have been developed to reduce the reflections at the aperture using a combination of resistive loading and shaping of the plates of the TEM horn. However, employing resistive loading methods generally reduces the efficiency of the antenna.

3.2.3 Effects of Dimensional Changes in the TEM Horn

From the previous section, one can see that the performance of the TEM horn is directly dependent its dimensions. The length of the antenna plates, which correspond to the scale factor of the horn, determines its lowest cut-off frequency. Increasing this length results in a scaling effect on the frequency response of the antenna, where its frequency response will be shifted towards the lower end by the same factor.

The impedance of the antenna is directly dependent on its width-to-height ratio (*w/h*). In order to maintain constant impedance, the azimuth and elevation angles must be kept constant throughout. The change in impedance due to the change in dimensions can be explained using simple microstrip theory. By keeping all other parameters constant, an increase in the azimuth angle, which corresponds to the increase in width in the microstrip model, results in a decrease in impedance. Conversely, the same effect can be achieved by decreasing its elevation angle, which corresponds to the decrease in height in the microstrip model.

Although the gain and beamwidth of a frequency independent antenna usually do not vary much over a wide range of frequencies, they are still dependent on the overall dimensions of the antenna. As mentioned earlier, these parameters can be related to each other by (2.7). In practical TEM horn antennas, its beamwidth exhibits a very wide beamwidth at low frequencies. This can be explained by the fact that the lower frequencies effectively see the antenna as a dipole, since the length of its plates is one half the wavelength of its lowest frequency. Therefore, a much lower gain is expected at low frequencies than those in the higher frequency range, where the antenna exhibits a more constant gain frequency response. In addition, the beamwidth also depends on the aperture size, which is directly proportionally with the *w/h* ratio. Therefore, a direct relationship can be drawn between the gain frequency response and the *w/h* ratio.

3.2.4 The Wideband Balun

The TEM horn is essentially a balanced antenna. It can be seen as two conducting transmission lines terminating at free space. However, the 50Ω coaxial cable used as its feed is an unbalanced medium. By terminating the coaxial feed with a balanced antenna, the difference in coupling between the core and outer part of the coaxial to the antenna results in a net flow of current to the ground through the outer layer of the cable. This excess current flow effectively turns the cable into an antenna, which results in undesirable radiation near its feedpoint. Thus, a balun (balanced to unbalanced) is introduced to provide matching for both modes.

The basic function of a balun is to shunt or dissipate excess current that results from an unbalanced feed to a balanced load. In literature, many baluns has been designed and widely discussed. However, only few operate beyond the UHF region and are broadband [18], [19]. A wideband balun can be achieved by connecting the inner conductor of the coaxial line to the upper plate of the TEM horn and the outer conductor to an enlarged lower plate shown in Fig 3.3. The expanded lower section acts as a ground plane for the top plate, realizing this section as an unbalanced antenna. Subsequently, a gradual change into the balanced structure completes its transition. This change in geometry allows the excess current to be dissipated through the expanded ground plane, thus giving the unbalanced feed a gradual transition to a balanced load [4], [7].

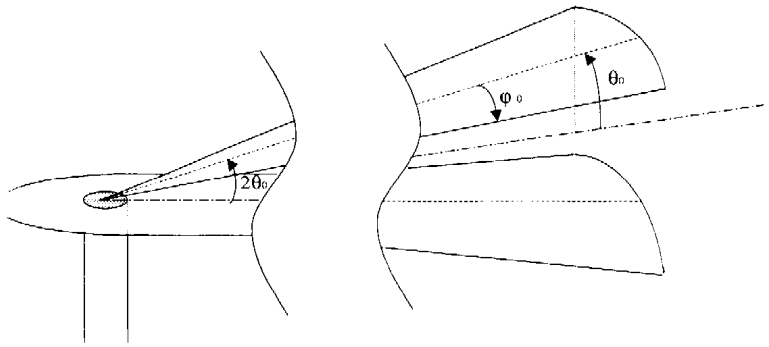

(a) (b)

Fig. 3.3. (a) Unbalanced configuration (b) Balanced configuration [4]

3.3 Design Methodology of the TEM Horn

The 3 Design Phases

Various approximations on the analysis of TEM horns have been discussed in the recent years. Most approximations discussed in literature involve complex and tedious calculations. However the results provide only qualitative agreement with experimental measurements. Thus, most designs on the TEM horn have been largely based on empirical methods. Here, the design process of the TEM horn is divided into three phases. Each phase sees a model with improved performance over its predecessor. The three models are namely, the basic TEM horn, the TEM horn with balun and the TEM horn with non-triangular structure. These models will be simulated using the HFSS simulation package.

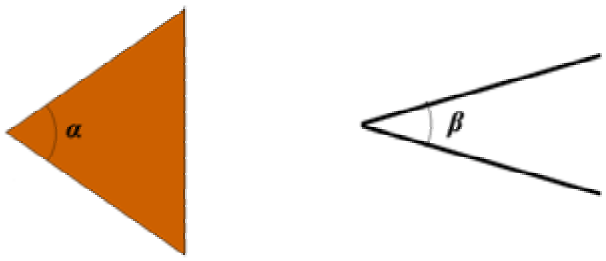

(a) (b)

Fig 3.4 Initial design of the TEM horn used in Phase I. (a) Top view (b) Side view.

The first phase of the design process uses the basic TEM horn structure shown in Fig 3.4. This design consist of two triangular conductive plate separated by an elevation angle at its feedpoint. From the previous section, it is clear that by using the microstrip model of the antenna, the azimuth angle α can be determined using its w/h ratio and elevation angle β [20], [21],

$$\alpha = 2\arctan\left[\frac{w}{2h}\sin(\beta/2)\right] \tag{3.2}$$

where the value of *w/h* for a 50Ω impedance is approximately 4.80 [20]. Using the same angles defined in [20], the azimuth angle α is found to be 67°, corresponding to an elevation angle β, of 32°. The separation between both plates at its feedpoint determines the highest operating frequency. To avoid higher modes in the horn, the minimum separation between the plates from (3.1) should be no larger than 25mm at a frequency of 6GHz. However, in our application, there is no need for a higher cut off frequency; therefore a separation distance of 1mm is used. The length of the antenna plates at boresight is determined by at least one half wavelength of its lower cut-off frequency, which corresponds to 187mm for a frequency of 800MHz. Using this basic model, the azimuth and elevation angles will be modified to provide the best impedance match throughout the operating range of frequencies.

In the second phase, a wideband balun will be integrated with the antenna as shown in Fig 3.5. This high frequency balun will ensure a gradual transition between the unbalanced feed and the balanced antenna, eliminating any net flow of current. To simulate the effectiveness of this balun, the antenna will be simulated with a piece of cylindrical structure at its feed.

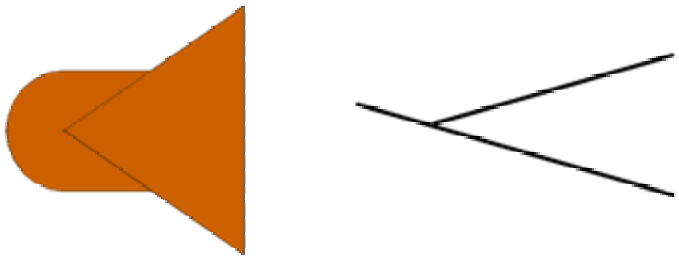

(a) (b)

Fig 3.5 Design of the TEM horn used in Phase II. (a) Top view (b) Side view.

The addition of the wideband balun sees a change in dimensions of the antenna near its feedpoint. This enlarged lower plane acts as an image plane to the unbalanced section of the antenna. Effectively, this doubles the distance between both plates. As a result, the *w*/h ratio is halved, which corresponds to an increase in impedance. However, the impedance increase of a microstrip model does not follow a linear pattern, thus a twofold increase in impedance is only used as an approximation. Since the balun is located near the feedpoint, this increase in impedance will mainly affect the impedance at its higher frequencies. The final phase includes changes to the overall shape of the horn. In this phase, the top plate is shaped in a particular way shown in Fig 3.6 to compensate the effects of the balun.

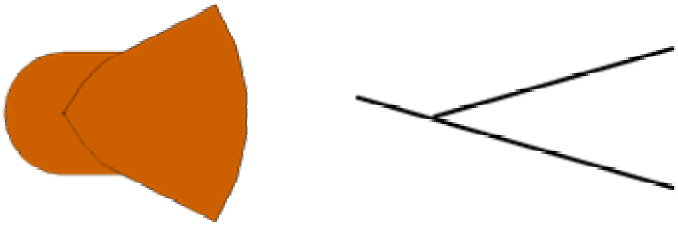

(a) (b)

Fig 3.6 Design of the TEM horn used in Phase III. (a) Top view (b) Side view.

3.4 Summary

The design of a basic TEM is fairly simple; however, this basic design is incapable of matching the input impedance of the antenna. This mismatch results in ringing in the antenna, which is highly undesirable in GPR systems. An analysis of the TEM horn can be approximated using microstrip theory. By dividing this antenna into infinite sections, the impedance of the antenna can be modified with respect to changes in its *w/h* ratio. However, this approximation is not expected to give very accurate results, therefore, the design of the TEM horn will be fully based on experimental models. Three phases of design, each with a unique modification, will be implemented in the

design process. Through these design phases, a balun will be added to match the unbalanced feed, while a non-triangular plate is introduced to compensate the effects of the balun.

Chapter 4. Design and Simulation Results

4.1 Simulations using HFSS

Throughout the design of this antenna, a software simulation package is used to provide a prediction on the performance of the actual antenna before its construction. HFSS, developed by Agilent Technologies for modeling microwave structures as well as antennas, is used to model the TEM horn throughout its whole design process. The main parameters of interest in a TEM horn are:

- Gain
- Radiation patterns (E and H planes)
- Beamwidth
- Reflection coefficient (S_{11})

Besides these parameters, HFSS also displays graphical animation of the antenna radiation.

The TEM horn model is drawn in HFSS using dimensions defined in the previous chapter, where L = 187mm, α = 69°, β = 32° and the feedpoint separation, B = 1mm. Before running the simulation, the software requires a boundary to be defined. A cylindrical boundary is used to simulate the far-field radiation boundary of the antenna.

In HFSS, this boundary must be defined at least a quarter wavelength away from the edges of the antenna.

As the TEM horn operates in an extremely wide frequency range, the abovementioned parameters are simulated at different points in its frequency range to give its frequency response. This can be achieved using two different methods, both with different requirements of computing power. The first method uses a user-defined number of frequency points in either linear of log scale, where HFSS generates results for the gain and reflection coefficients in these frequency points. The downside of this method is that the accuracy of its actual frequency response depends on the number of points defined. Through interpolation between the points, the results tend to show a smoother effect than it actually is. On the other hand, the second method uses a fast frequency sweep. This method allows HFSS to sweep through a user-defined range of frequencies, concentrating on areas with more changes, providing a more accurate representation of the simulated parameters. However, this method requires a comparatively huge amount of computing power. A comparison between both methods shows that simulations running with 10 log points between 400MHz and 10GHz produce relatively accurate results. Therefore, throughout the whole design process, all the models will be simulated using 10 log points between its 400MHz and 10GHz.

The simulation runs in a series of iterations, with a finer mesh defined for every succeeding one. Running a simulation on a finer mesh uses higher computing power, very often resulting in insufficient memory. On the other hand, insufficient number of iterations produces inaccurate results. One way of keeping the computing power at minimum while achieving a high level of accuracy is by introducing symmetry planes to the antenna models.

Recall that a basic TEM horn made up of two equal isosceles triangles is a symmetric about the E-plane and H-plane. Taking advantage of its symmetrical structure, a symmetry plane is introduced in HFSS to reduce the amount of computing power needed. A symmetry plane in HFSS is essentially an infinite plane defined by the user. When introduced to the E-plane, only the top half of the TEM horn is needed to generate similar results in a full TEM horn as the symmetry plane simulates an infinite

ground plane, thus, creating an exact image of the top half of the antenna. Similarly, a symmetry plane at the H-plane produces the same image effect. Effectively, this reduces the antenna size by four times, resulting in a great reduction of simulation time. However, in the second and final phases of the design, only symmetry in the H-plane is achieved due to the inclusion of the wideband balun.

All simulated results obtained in HFSS are readily available, with the exception of impedance. Due to a bug in the software package, the impedance has to be calculated using the reflection coefficient (S_{11}). Post processing on reflection coefficient is accomplished by calculating its real impedance using equations described in Appendix A. Other parameters such as gain, beamwidth and radiation patterns are taken directly from the HFSS console. It is later noted that the gain given in the HFSS console is not taken from its boresight, as HFSS makes no distinction between the boresight and the rest of the antenna. Instead, HFSS calculates gain with reference from its peak value regardless of direction. In Chapter 5, an approximate gain taken from its boresight will be included in the gain frequency response plot of the final design to show the discrepancies between both gains.

4.2 Numerical Simulations and Design Process

The results of the simulations are presented in the order of their corresponding phases. The frequency response plots on impedance, |Z|, reflection coefficient, |Γ| and beamwidth will be presented in this section. The real impedance performance and the reflection coefficient are just different representations of the same data. However, the reflection coefficient takes into account of the comparison between the actual impedance and the load impedance. It should be noted that all the values in the radiation pattern plots are +20dB higher when plotted with MATLAB. A summary of the dimensional parameters are presented in Table 4.1.

Legend	Shape	Mouth	Azimuth	Elevation	Separation	Balun
TEM Horn (tri/flat/69/32/4/nobal)	tri	flat	69	32	4	no
TEM Horn (tri/flat/69/32/1/nobal)	tri	flat	69	32	1	no
TEM Horn (tri/flat/43/18.9/1/nobal)	tri	flat	43	18.9	1	no
TEM Horn (tri/flat/52.4/23.7/1/nobal)	tri	flat	52.4	23.7	1	no
TEM Horn (tri/flat/63.6/32/1/nobal)	tri	flat	63.6	32	1	no
TEM Horn (tri/flat/70.2/32/1/nobal)	tri	flat	70.2	32	1	no
TEM Horn (tri/curve/69/32/1/nobal)	tri	curved	69	32	1	no
TEM Horn (tri/flat/69/32/1/smlbal)	tri	flat	69	32	1	small
TEM Horn (tri/flat/69/32/1/bigbal)	tri	flat	69	32	1	big
TEM Horn (tri/curve/69/32/1/bigbal)	tri	curved	69	32	1	big
TEM Horn (tri/curve/69/20/1/bigbal)	tri	curved	69	20	1	big
TEM Horn (tri/curve/73.1/32/1/bigbal)	tri	curved	73.1	32	1	big
TEM Horn (tri/curve/100/32/1/bigbal)	tri	curved	100	32	1	big
TEM Horn (non-tri/curve/69/32/1/bigbal)	non-tri	curved	69	32	1	big
TEM Horn (non-tri/curve/69/20/1/bigbal)	non-tri	curved	69	20	1	big

Table 4.1. Summary of the changes in dimensional parameters for the TEM horn. The legend will be used in all the frequency response plots.

4.2.1 UWB TEM Horn Design: Phase I

The first phase of the design mainly sees the effects of the change in angular dimensions of the basic TEM horn. Contrasting results have been obtained through the change in feedpoint separations, the azimuth and elevation angles. The results from this phase verify the theories discussed in the previous chapter. A clear understanding on the design implications of this phase will aid the design of the TEM horn in the next phase.

Comparison between TEM Horns with Different Feed Separation

As mentioned in the earlier sections, the mode suppression of the TEM horn depends on the separation between its feedpoint. From (3.1), it can be seen that the separation between the feedpoint must be less than 25mm. In theory, a small separation produces high cut-off frequency. In this section, two different separations of 1mm and 4mm with same azimuth and elevation angles are simulated.

The simulation results in Fig 4.1 show a wider frequency response in the model with a 1mm separation. As suggested by theory, the model with a larger separation suffers from a gain drop at about 7.5GHz, which indicates its higher cut-off frequency. In Fig 4.3, the model with a 1mm separation also shows a better match to a 50Ω load compared to the model with a larger separation. This could be due to the accuracy of the *w/h*, especially at the feedpoint, where the difference in the separation is more pronounced in the *w/h* ratio. The model with a larger separation also produces a fair amount of reflection throughout the range of 400MHz to 10GHz.

From this simulation, it can be seen that a feedpoint separation of 1mm produces better performance in terms of gain and impedance response. This separation distance is not further reduced as its physical construction may be hard to realize. Therefore, all the subsequent models in the design process will be based on a feedpoint separation of 1mm.

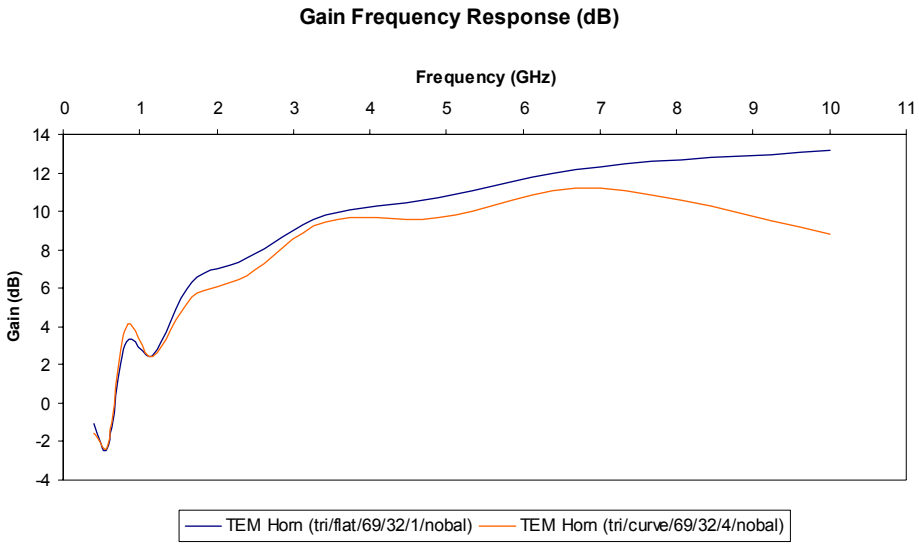

Fig 4.1 A comparison of gain frequency response between the simulated models with a feedpoint separation of 1mm and 4mm.

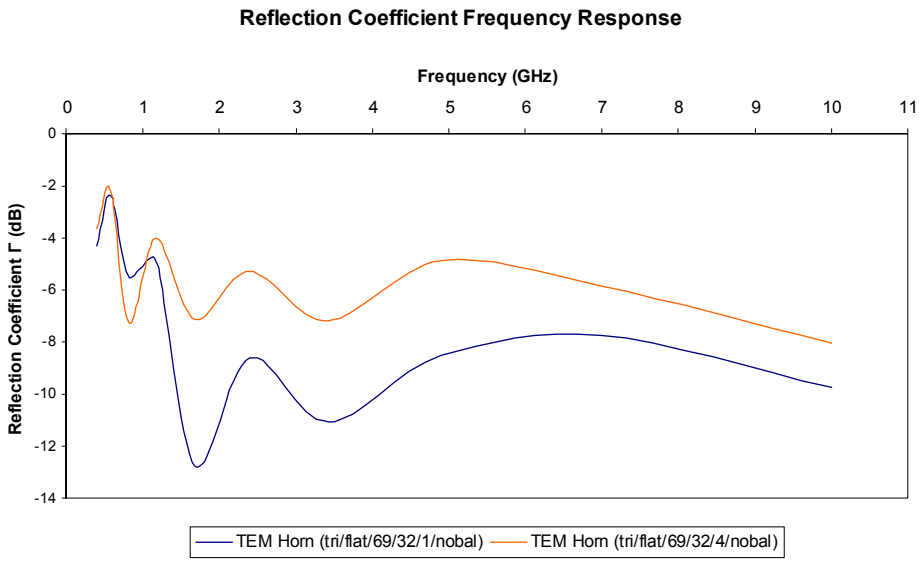

Fig 4.2 A comparison of reflection coefficient frequency response between the simulated models with a feedpoint separation of 1mm and 4mm.

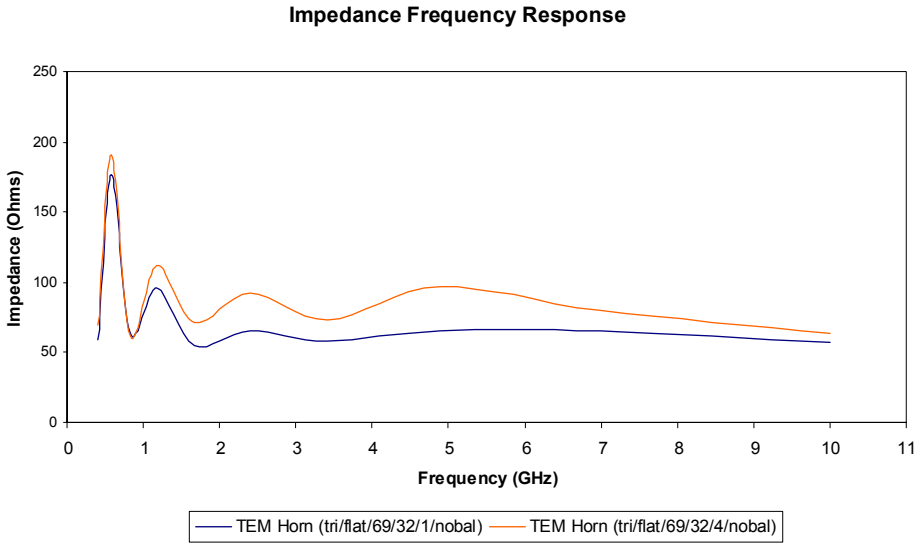

Fig 4.3. Impedance |Z| frequency response for TEM horns with a feedpoint separation of 1mm and 4mm.

.

Comparison between TEM Horns with Same *w/h* ratio, using Different Angles

From microstrip theory, it is known that the impedance of the TEM horn is dependent on the *w/h* ratio. The TEM horn is an aperture antenna, thus the size of the aperture directly affects the performance of the horn. The azimuth and elevation angles define the size of the aperture, which affects the *w/h* ratio, thus its impedance. This ratio can be kept constant by adjusting both azimuth and elevation angles accordingly using (3.2). Using $w/h = 4.8$, two models with different aperture sizes are simulated. The first model uses $\alpha = 69°$ and $\beta = 32°$, while the second model uses $\alpha = 43°$ and $\beta = 18.9°$.

The results in Fig 4.4 show that the smaller horn exhibits a lower gain frequency response over a band of 10GHz. This result is expected as the reduced aperture results in a wider beamwidth, which decreases the overall gain frequency response. In its impedance performance shown in Fig 4.6, the smaller horn exhibits lower impedances in the low frequency range. However, its impedance increases above 2.7GHz. Similar simulations using a fixed azimuth angle and reduced elevation angle produces similar

impedance performance. Thus, it can be concluded that a decrease in elevation angle reduces the impedance at lower frequencies.

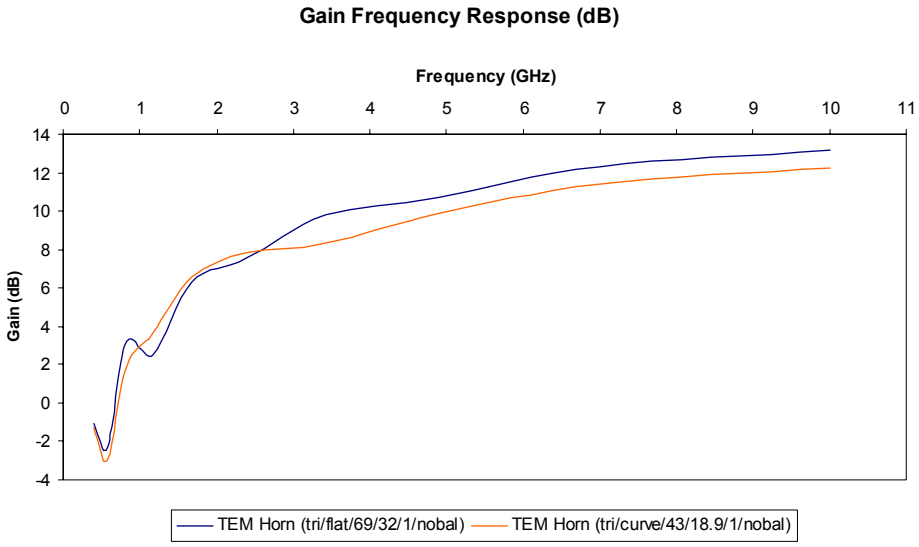

Fig 4.4. Gain frequency response for TEM horns with same *w/h* ratio using different azimuth and elevation angles.

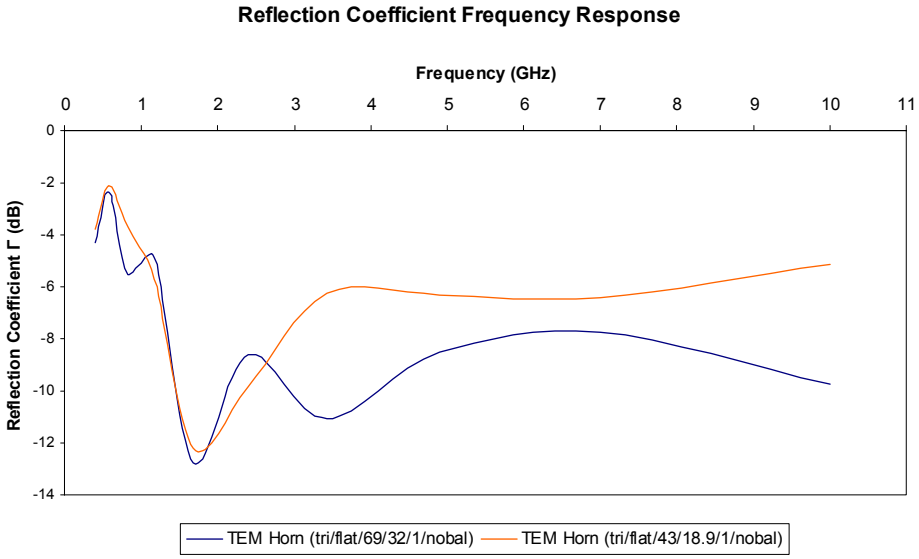

Fig 4.5. Reflection frequency response for TEM horns with same *w/h* ratio using different azimuth and elevation angles.

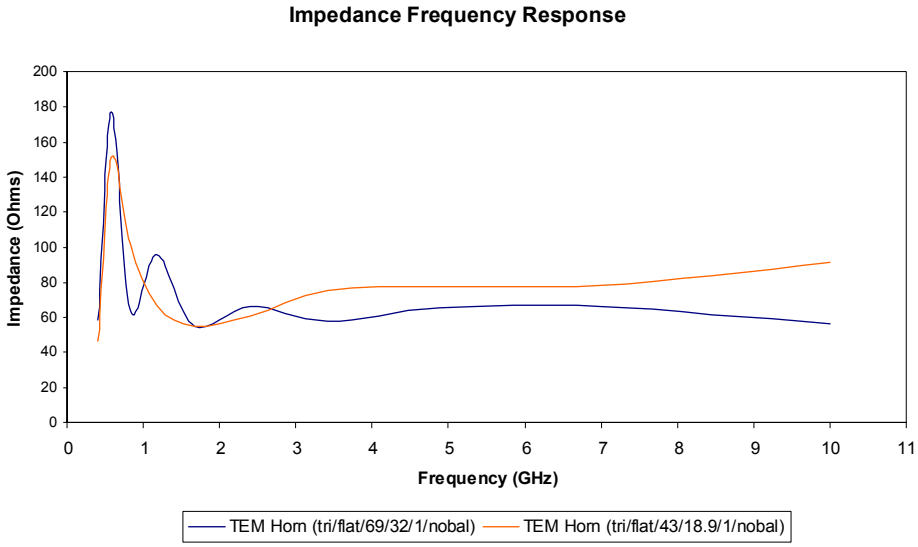

Fig 4.6. Impedance |*Z*| frequency response for TEM horns with same *w/h* ratio using different azimuth and elevation angles.

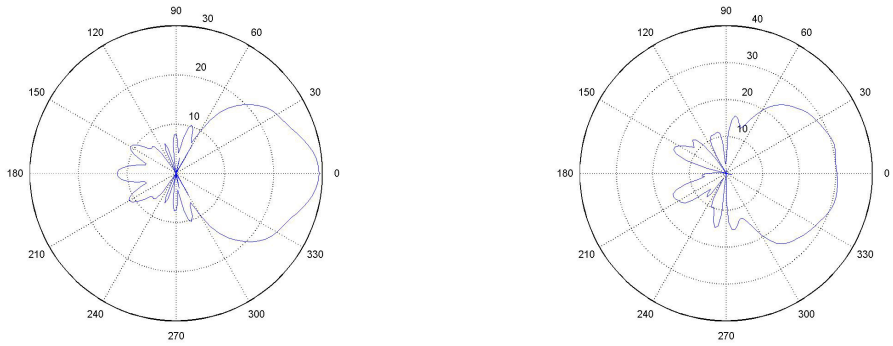

Fig 4.7. H-plane radiation pattern for TEM horn with α = 69, β = 32 at 2.4GHz (left) and 5GHz (right). These values are expressed in Gain+20dB.

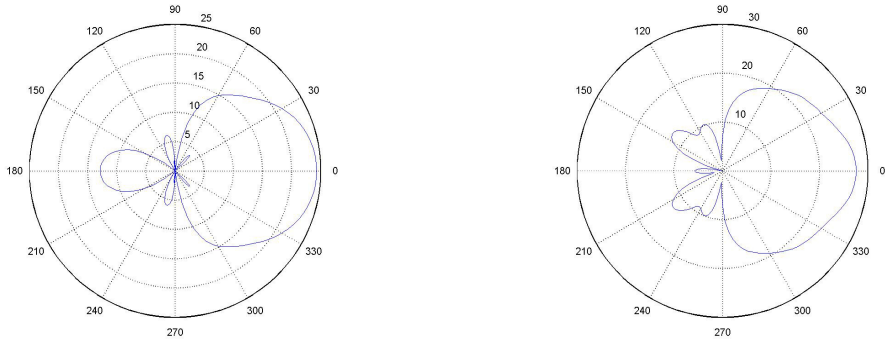

Fig 4.8. Radiation pattern for TEM horn with α = 43, β = 18.9 at 2.4GHz (left) and 5GHz (right). These values are expressed in Gain+20dB.

From the radiation patterns shown in Fig 4.7 and Fig. 4.8 for both horns, the smaller horn results in a narrower beamwidth with the increase in frequency. Ideally, the antenna is desired to exhibit a narrow beamwidth. However, this requirement is reversed when the SAR is used. By taking the average of multiple measurements across the area of detection, the SAR effectively behaves like an antenna with an extremely large aperture, thus a wide beamwidth will allow the SAR to collect more samples from a target.

Comparison between TEM Horns with Increased *w/h* ratio

As mentioned in the preceding chapter, the impedance of the TEM horn can be reduced by increasing its *w/h* ratio, which means an increase in the azimuth angle or decrease in the elevation angle. From the results of the initial design, it is apparent that some modifications have to be made to achieve a better impedance match. Results from these modifications will be used to isolate the effects of the changes in the *w/h* ratio on the antenna performance.

Three models with fixed elevation angle of, β = 32°, and azimuth angles of 69°, 70.2° and 78° are simulated in HFSS and the results shown in Fig 4.9. A 2dB decrease in gain is observed in the model with α = 78° above 5GHz. From Fig 4.11, is can also be seen

that the increase of *w/h* through an increase in azimuth angle results in a decrease in impedance at frequencies below 6GHz, above which the impedance begins to increase with frequency.

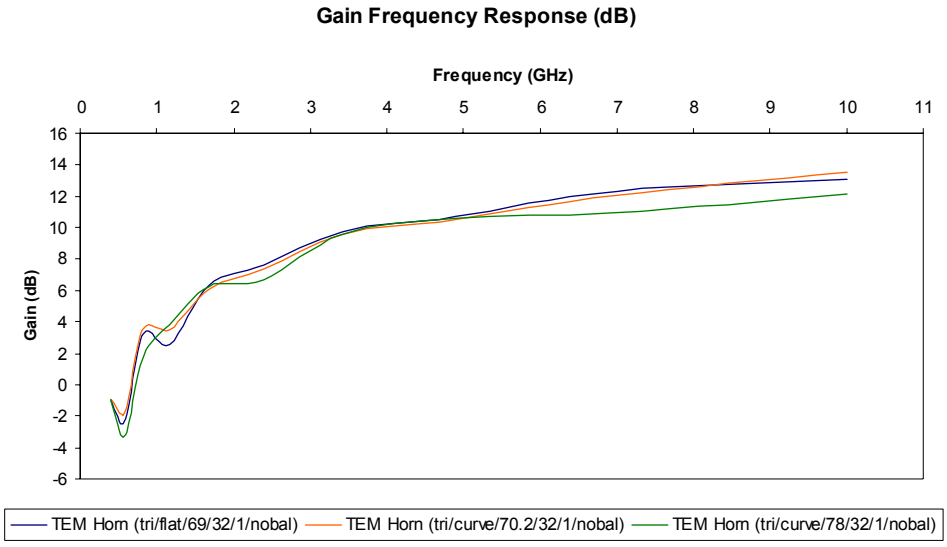

Fig 4.9. Gain frequency response for TEM horns using different *w/h* ratio.

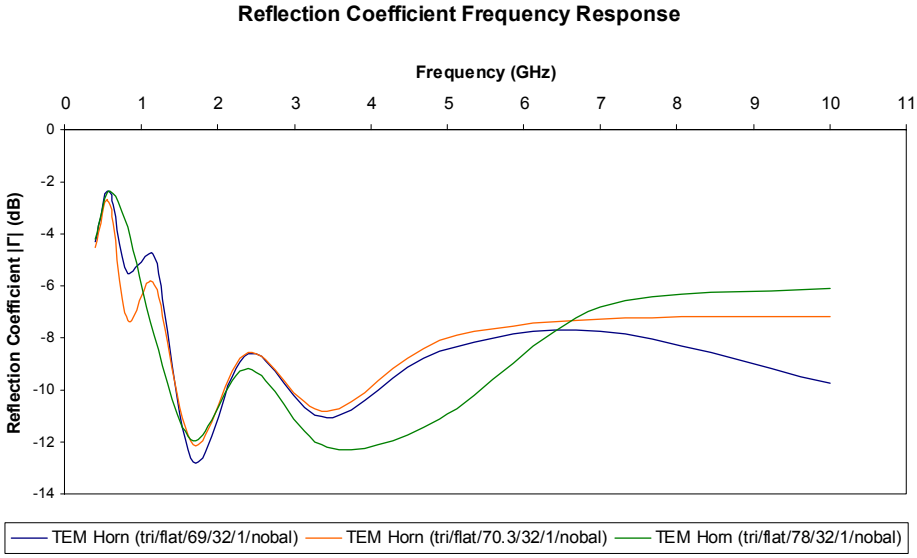

Fig 4.10. Reflection frequency response for TEM horns using different *w/h* ratio.

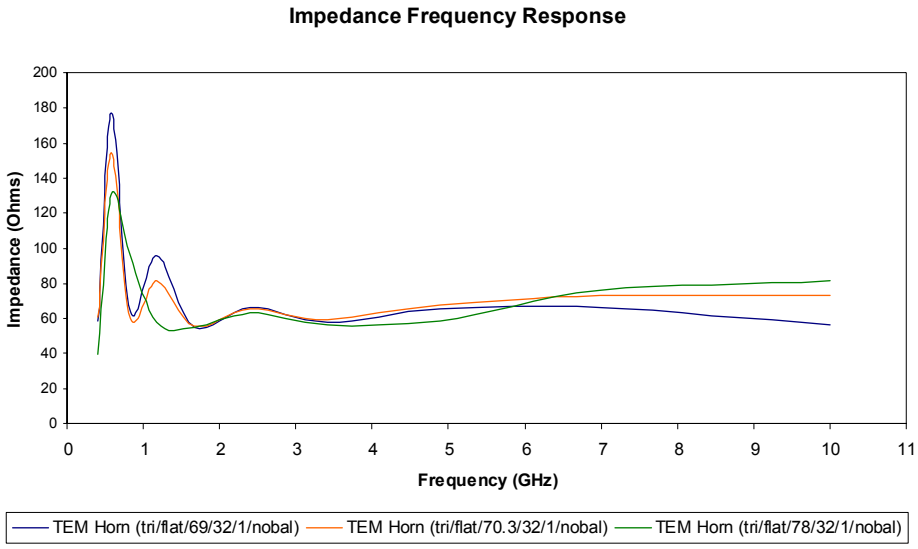

Fig 4.11. Impedance |*Z*| frequency response for TEM horns using different *w/h* ratio.

The radiation plots in Fig. 4.12 shows similar results for the initial design in Fig 4.7. The small change in azimuth angle did not result in a significant change in its radiation pattern compared to the change in its impedance frequency response. On the other hand, at an azimuth angle of 78°, the TEM horn produces lesser sidelobes as shown in Fig 4.13. Overall, the radiation patterns did not vary much with relatively small change in azimuth angles.

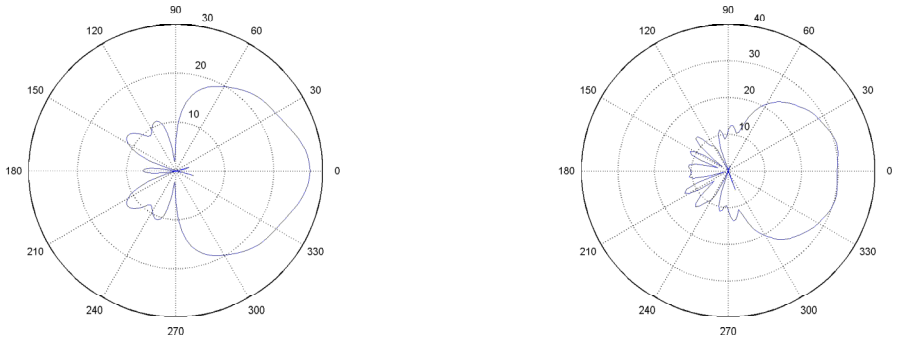

Fig 4.12. Radiation pattern for TEM horn with α = 70.2, β = 32 at 2.4GHz (left) and 5GHz (right). These values are expressed in Gain+20dB.

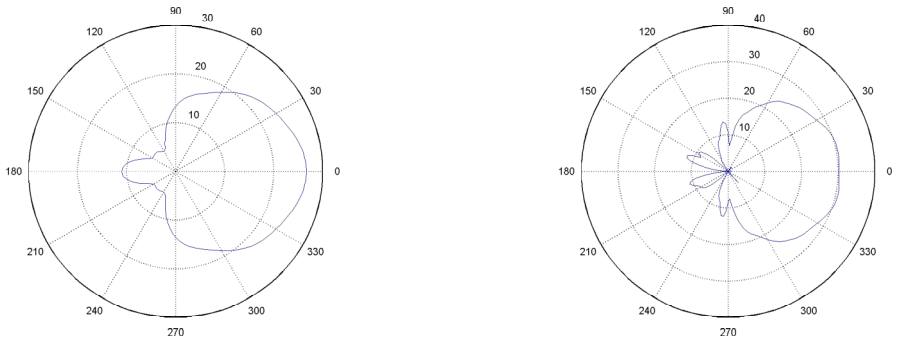

Fig 4.13. Radiation pattern for TEM horn with α = 78, β = 32 at 2.4GHz (left) and 5GHz (right). These values are expressed in Gain+20dB.

Comparison between TEM Horns with Curved Structure at Mouth

Having defined the angles of the horn, a curved structure is introduced to the flared end of its plates. If the azimuth angle is increased significantly, the EM fields at the edge of the horn take a longer time to radiate into free space than those near its boresight. Moreover, the lower cut-off frequency is determined by the length of the antenna plates; a flat edge at the mouth of the horn means that the lengths at the edges are longer than that from the boresight.

Results in Fig 4.14 show almost similar results in its gain frequency response with that without the curved structure. On the other hand, the impedance frequency response in Fig. 4.16 shows a significant reduction in reflection in its low frequency range. This phenomenon however reverses at about 1.5GHz, where its impedance begins to increase as a function of frequency.

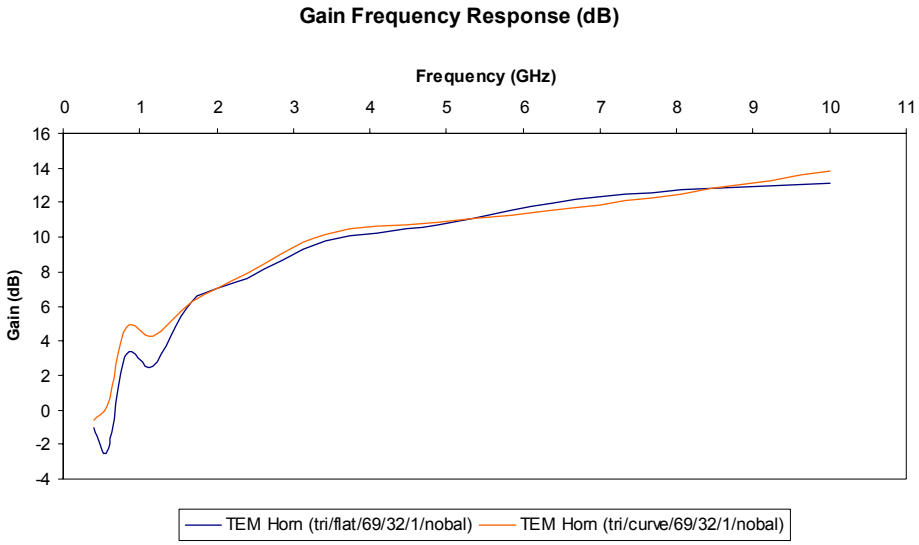

Fig 4.14. Gain frequency response for TEM horns with curved structure at mouth.

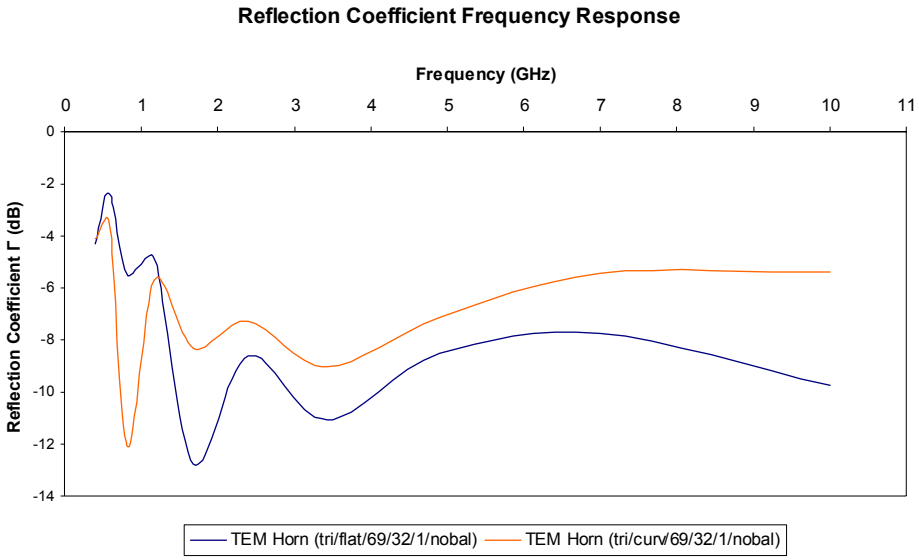

Fig 4.15. Reflection coefficient frequency response for TEM horns with curved structure at mouth.

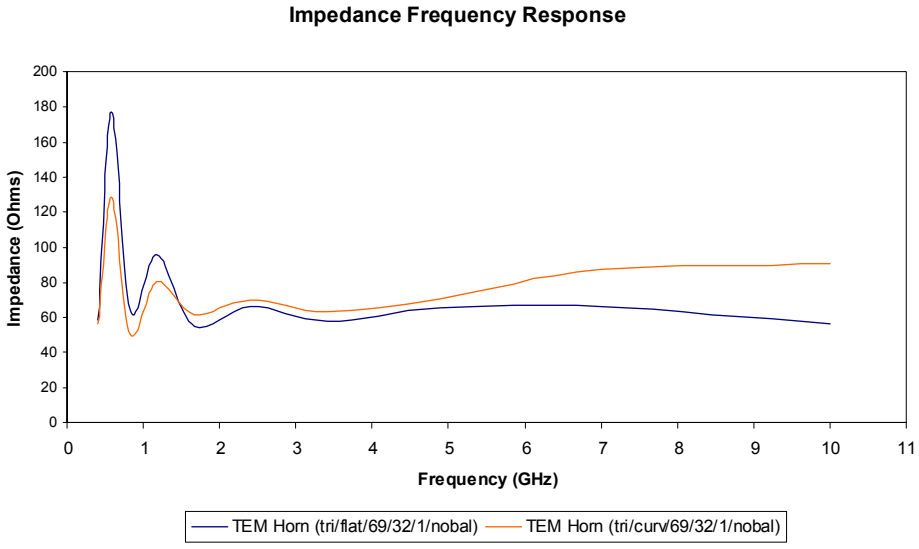

Fig 4.16. Impedance |Z| frequency response for TEM horns with curved structure at mouth.

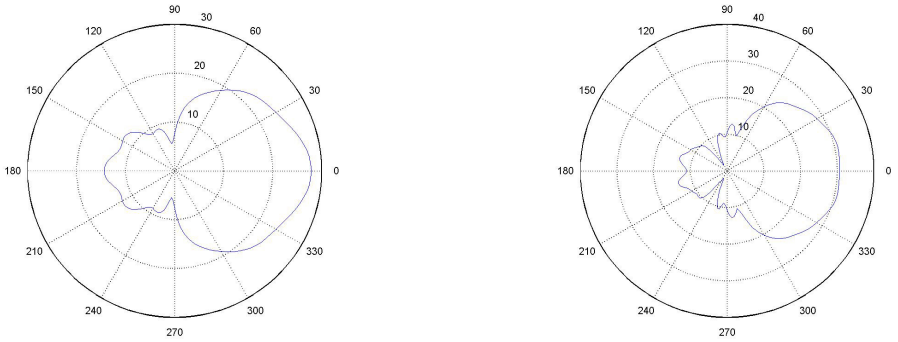

Fig 4.17. Radiation pattern for TEM horn with curved structure at mouth at 2.4GHz (left) and 5GHz (right). These values are expressed in Gain+20dB.

Summary

The initial model with parameters from [20] shows relatively high reflection and impedance throughout the entire range of frequencies. From all the results obtained in this phase, two methods of reducing the impedance from the initial model have been achieved. The impedance has shown a significant reduction at its lower frequencies by increasing the *w/h* ratio and including a curved structure at its flared end. Employing the curved structure into the initial design is used as the primary modification for the next phase with the *w/h* ratio providing a 2nd degree of freedom in impedance matching.

4.2.2 UWB TEM Horn Design: Phase II

Comparison between TEM Horns with Different Baluns

In the second phase, the wideband balun is incorporated into the design to reduce the net flow of current during the transition between the unbalanced medium to the balanced antenna. The balun is located near the feedpoint, where the section with the enlarged lower plate behaves like an unbalanced antenna. The transition of modes completes when the enlarged section gradually shapes towards the dimensions of a

balanced antenna. In this phase, two models using the initial design with balun radius or 4cm and 6cm are simulated.

Comparison of the results shows a better performance in the impedance frequency response at the high frequency region with the larger balun. This is due to the fact that a larger area is used for current dissipation, which generally affects only the impedance performance at high frequencies, since their wavelengths are relatively smaller than the size of the balun. Furthermore, the inclusion of the balun also results in a significant drop in the "peak" at about 600MHz in the impedance frequency response.

The radiation patterns between both models show almost similar characteristics, since the change in balun dimensions does not really affect the size of its aperture. However, comparison with the model without the balun shows a significant increase in sidelobes at 2.4GHz and a slight drop in boresight gain at 5GHz.

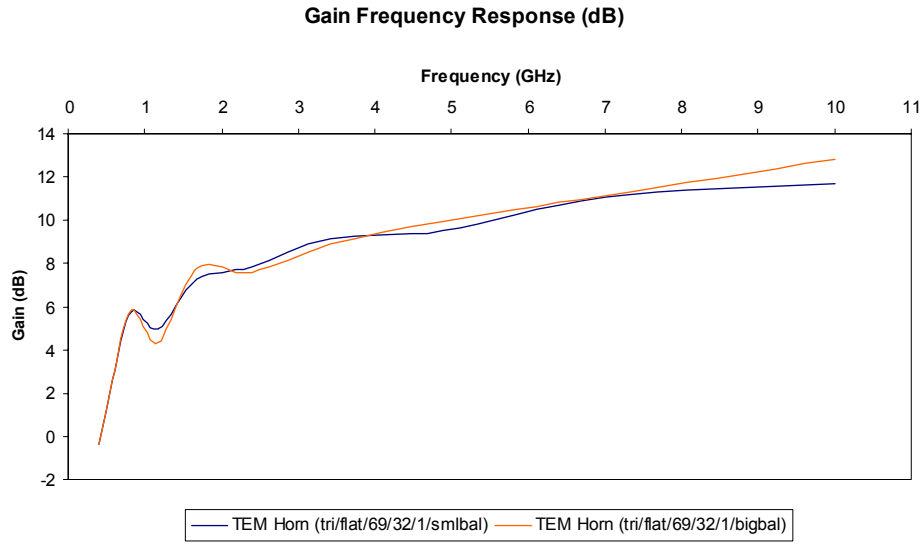

Fig 4.18. Gain frequency response for TEM horns with different balun dimensions.

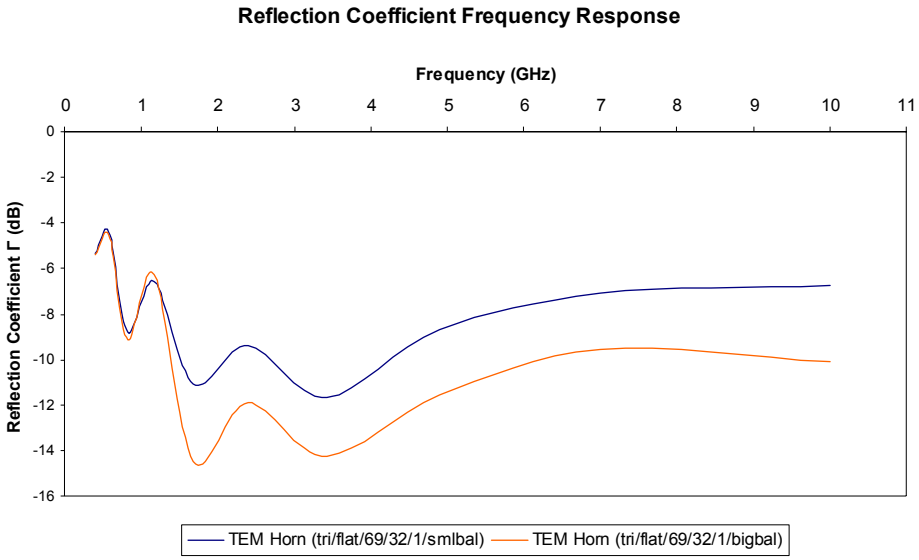

Fig 4.19. Reflection coefficient frequency response for TEM horns with different balun dimensions.

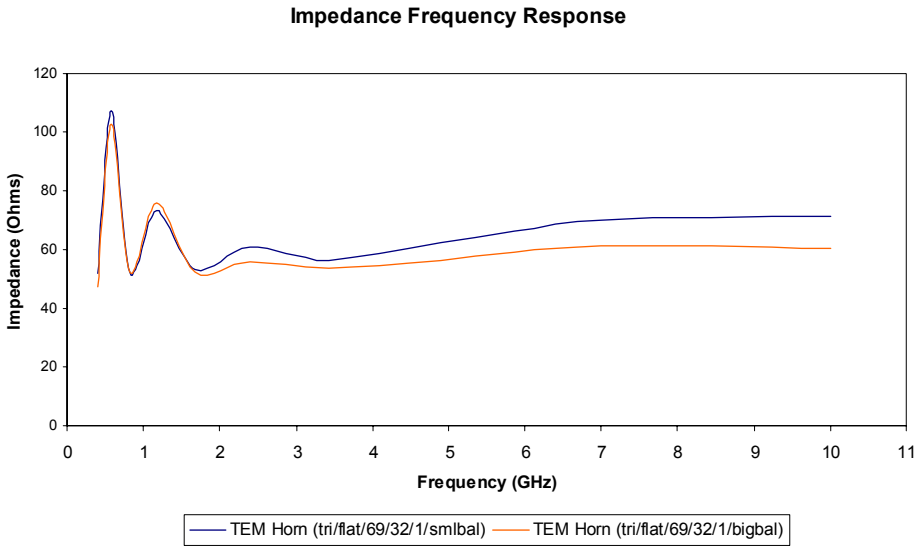

Fig 4.20. Impedance |Z| frequency response for TEM horns with different balun dimensions.

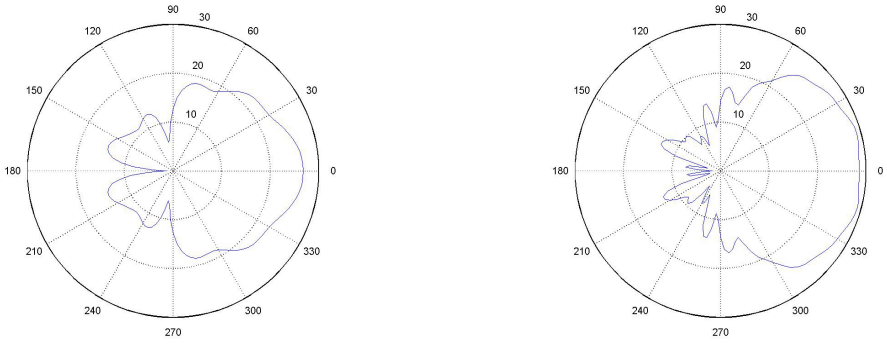

Fig 4.21. Radiation pattern for TEM horn with balun radius = 4cm at 2.4GHz (left) and 5GHz (right). These values are expressed in Gain+20dB.

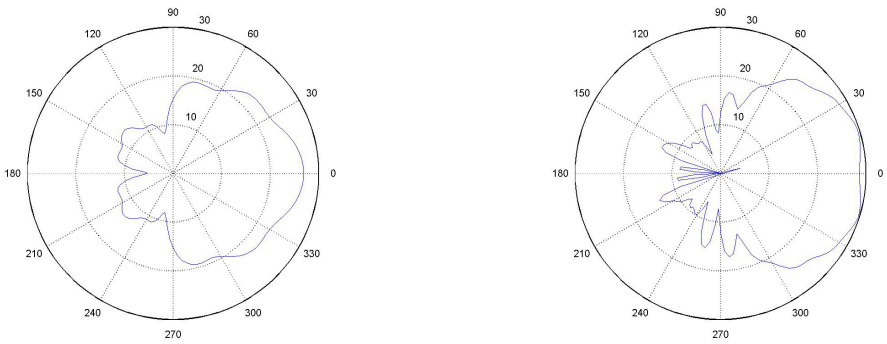

Fig 4.22. Radiation pattern for TEM horn with balun radius = 6cm at 2.4GHz (left) and 5GHz (right). These values are expressed in Gain+20dB.

Comparison between TEM Horns with Increased *w/h* with Balun

In this phase, the dimensions of the horns are changed by increasing their *w/h* ratio using the model with the balun with a radius of 6cm and a curved structure at its flared end. With the inclusion of the balun, a drop in impedance frequency response is achieved. Thus, the aim of this phase is to further reduce the impedance towards 50Ω by changing its *w/h* ratio as mentioned in the preceding section. These values are chosen in increasing steps from the initial *w/h* value of 4.8. The following *w/h* ratio of

5.4 and 8.6 for increased azimuth angles and 7.9 for decreased elevation angles are used in the simulation.

Simulation results from HFSS shows varying effects for different adjustments in the *w/h* ratio. The simulation results shows some unexpected outcomes as an increase in *w/h* did not improve the impedance response at frequencies below 1GHz, which has been the case for the models without the balun. At 2GHz, the reflection coefficient decreases with an increase in *w/h*, which are in good agreement with the theory. With frequencies between 3 – 5GHz, the impedance shows almost similar response for all the designs with increase *w/h* ratios, after which the impedance increases for models with higher *w/h* ratios.

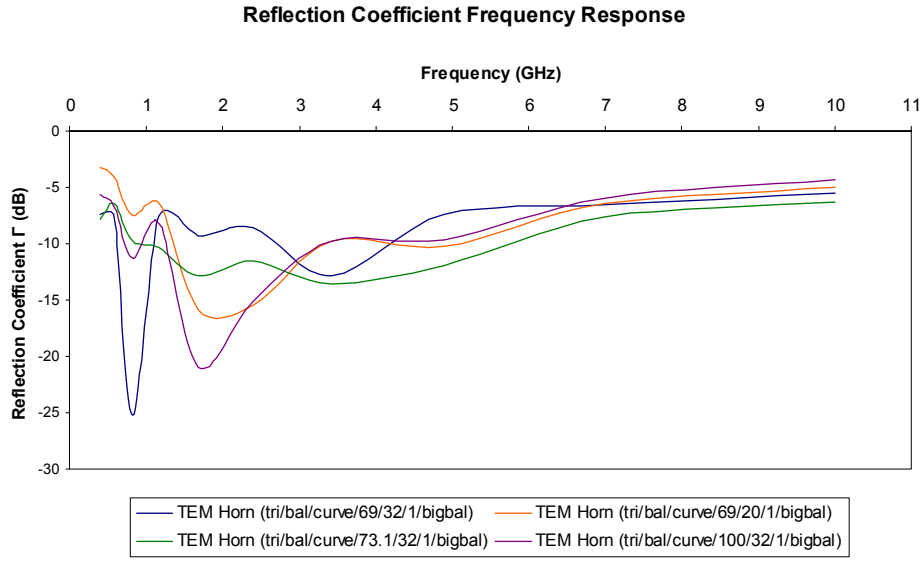

Fig 4.23. Reflection coefficient frequency response for TEM horns with different *w/h* ratios.

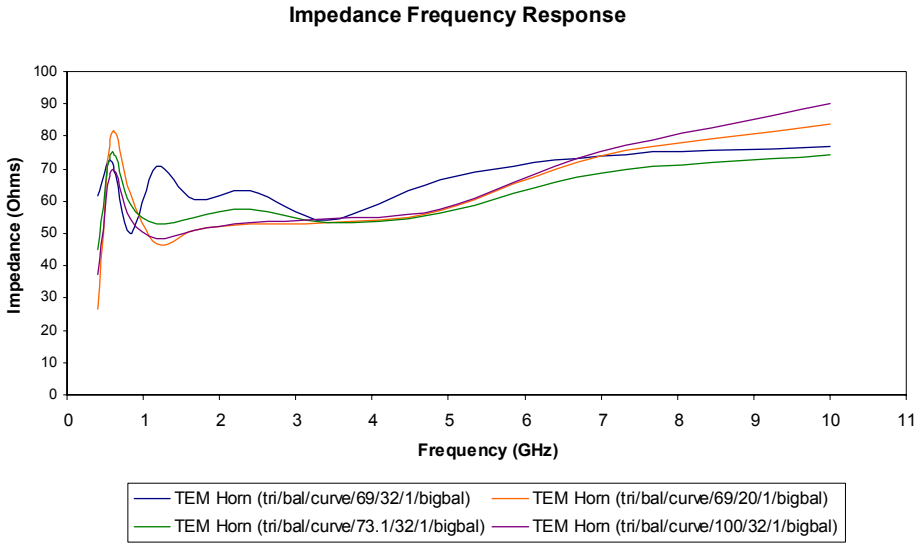

Fig 4.24. Impedance |Z| frequency response for TEM horns with different *w/h* ratios.

Summary

A general relationship can be derived from these results, although they did not show complete linear relationship between its impedance frequency response and its dependence on the *w/h* ratio across the entire range of frequencies. Results obtained in this phase show a trade-off in achieving a perfect impedance match between the lower and higher frequency range by using a higher *w/h* ratio. This leads to the development of the TEM horn using non-triangular plates.

4.2.3 UWB TEM Horn Design: Phase III

Comparison between TEM Horns with Triangular and Non-Triangular Plates

Simulations results from the preceding phases show that a conventional TEM horn design with two triangular shaped plates is unable to achieve a desired performance within the specified frequency range from 800MHz to 6GHz. From the preceding

section, the model with an added balun exhibits contradicting impedance performance between 400MHz to 10GHz. These results show a rising trend in the impedance response at high frequencies, while its impedance at lower frequencies generally produces more consistent response. Thus, non-triangular shaped plates are introduced to reduce the effects by the balun, which is responsible for the rise in impedance at high frequencies. As mentioned before, the higher cut-off frequency of the TEM horn depends on the construction of the feed, where the region around the feedpoint determines its performance at high frequencies. The inclusion of the wideband balun increases the impedance response of the horn at high frequencies since the balun effectively halves the *w/h* ratio of the antenna near the feedpoint. In order to compensate this effect, a larger *w/h* ratio is required between the top plate and its image. Thus, the plates are shaped in a particular way shown in Fig 3.6. This bell shaped plates sees a gradual increase in the width of the *w/h* ratio from the mouth of the horn to its feedpoint.

A comparison between the simulation results between the triangular and non-triangular shaped horn shows a significant increase in performance in impedance response over the entire frequency range. Results show that the impedance fluctuates between 45Ω and 55Ω from 800MHz to 6GHz. This results in less than -10dB of power reflected within the antenna. However, the gain suffers from a slight reduction of about 2dB between 3 – 4GHz. The radiation pattern shown in Fig. 4.29 also shows about 3dB decrease in gain at its boresight at 5GHz. Nonetheless, the non-triangular TEM horn model produces excellent matching for a very wide range of frequency.

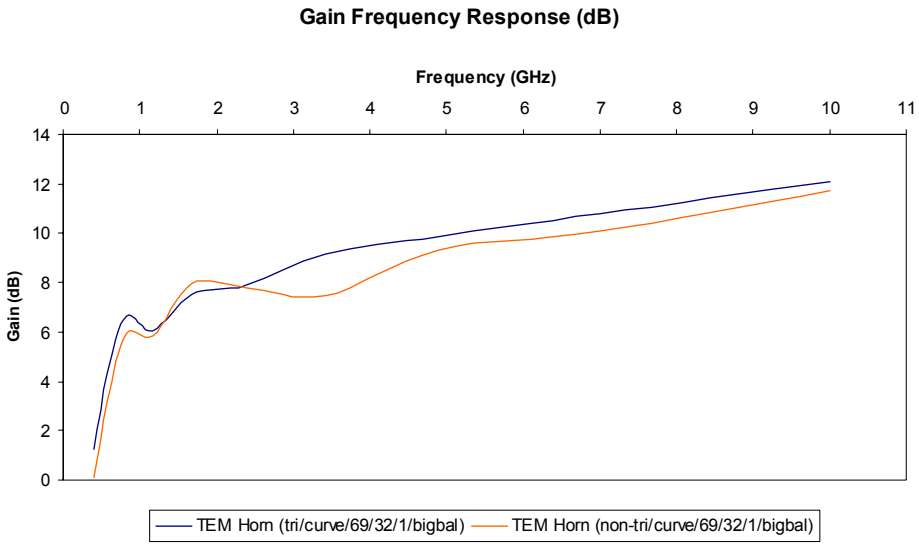

Fig 4.25. Gain frequency response for TEM horns with triangular and non-triangular shaped plates.

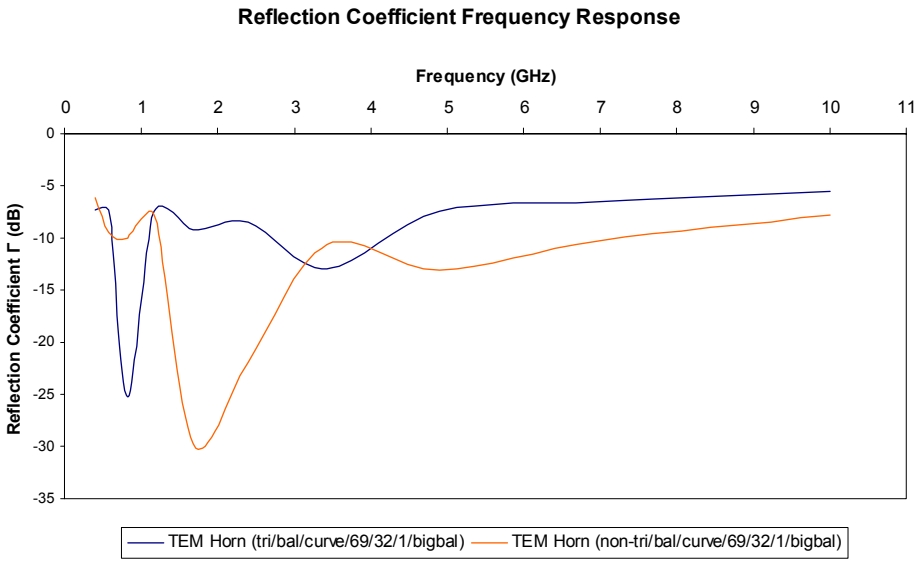

Fig 4.26. Reflection coefficient frequency response for TEM horns with triangular and non-triangular shaped plates.

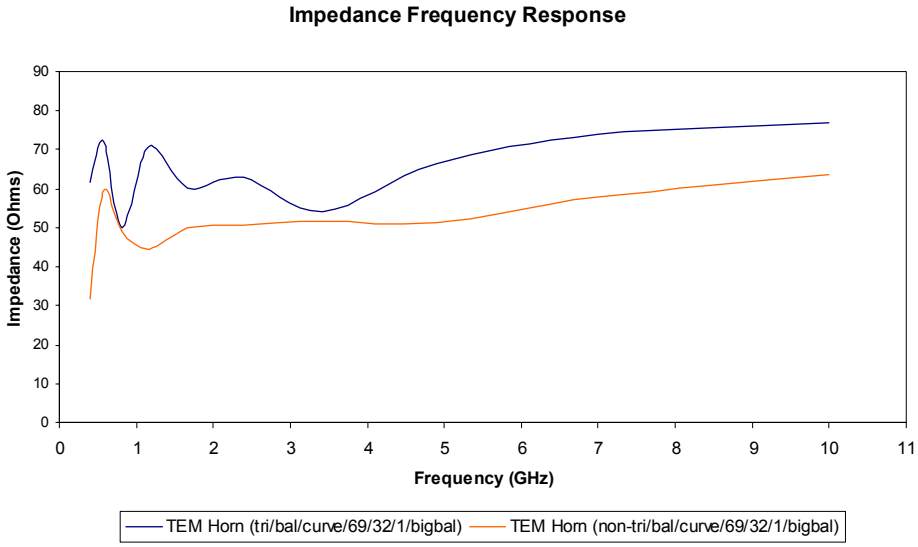

Fig 4.27. Impedance |Z| frequency response for TEM horns with triangular and non-triangular shaped plates.

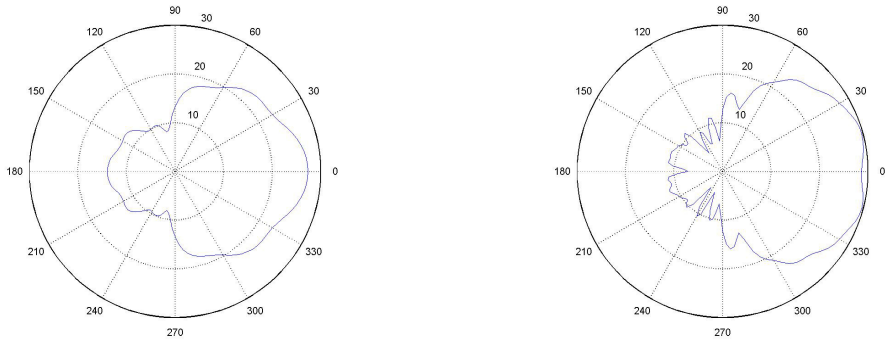

Fig 4.28. Radiation pattern for TEM horn with triangular plates at 2.4GHz (left) and 5GHz (right). These values are expressed in Gain+20dB.

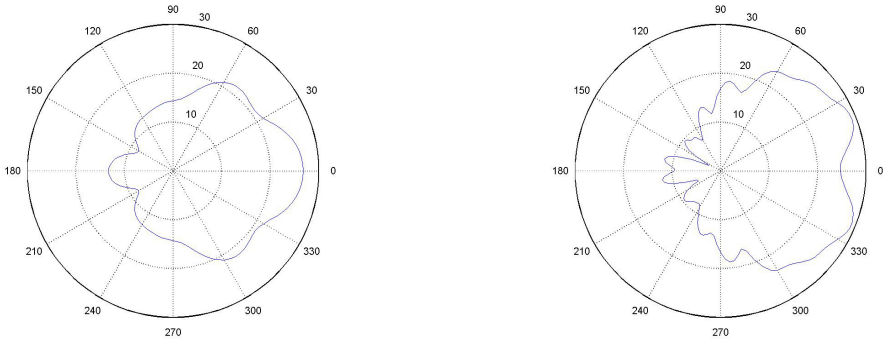

Fig 4.29. Radiation pattern for TEM horn with non-triangular plates at 2.4GHz (left) and 5GHz (right). These values are expressed in Gain+20dB.

Summary

From the simulation results, this TEM horn design exhibits a very good match with the 50Ω input coaxial cable and relatively constant gain between 800MHz and 6GHz. Despite the formation of a -3dB null at the boresight at 5GHz, this model is capable of radiating and receiving fast EM transients between 800MHz and 6GHz. Since the gain frequency response did not show any decline at the higher frequencies, this reduction in gain at the boresight might not cause a significant effect on the operation of a GPR that uses SAR imaging.

Comparison between the Final Design with Effect from Coaxial Cable

In the final design of the TEM horn, a coaxial cable is added in the simulation model to show the effectiveness of the balun. This is achieved by adding a piece of cylindrical conductor to the feedpoint of the horn. A radiation field plot on the H-plane is shown in Fig 4.30. This field plot shows very little E-fields radiating between the cylindrical structure and the feedpoint. These E-fields are the net flow current resulting from the transition from an unbalanced mode to a balanced mode. Theoretically, the balun should have an infinite ground plane. However, it is not practical to build an antenna

with even a very large lower plate, thus, this results in some net flow current at the outer layer of the coaxial cable. With this net flow current, the coaxial cable effectively behaves like an antenna, radiating unwanted signals that result in interference with the transmitted signals. From the results, it can be seen that the amount of radiation in the coaxial cable is negligible, thus proving the effectiveness of the balun.

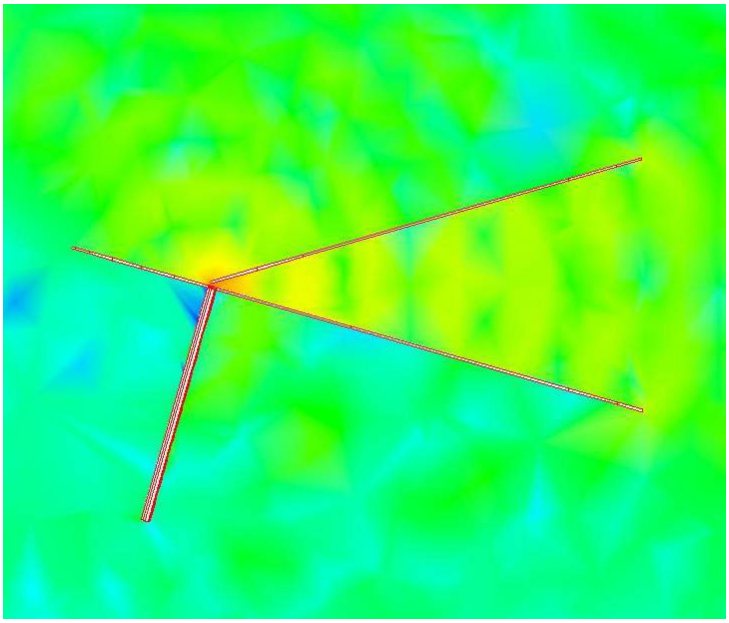

Fig 4.30. H-plane radiation field plots of the TEM horn with a cylindrical structure simulating a coaxial cable at its feedpoint. The net flow current in cable is shown in blue near the feedpoint.

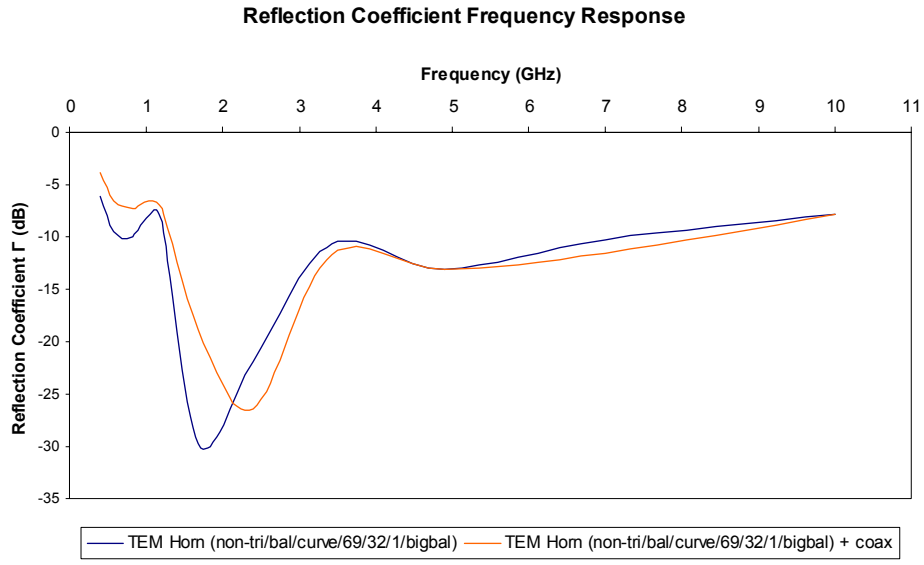

Fig 4.31. Reflection coefficient frequency response for final TEM horn design with and without coaxial cable.

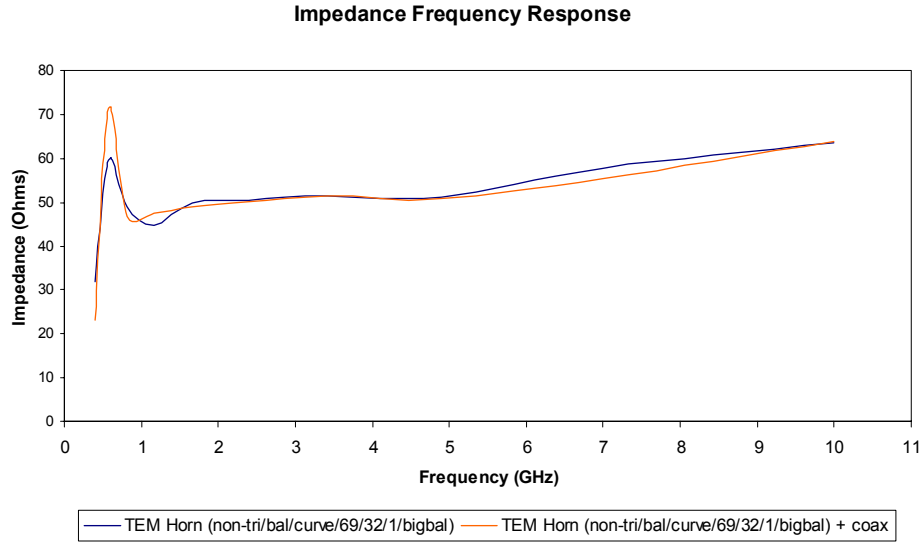

Fig 4.32. Impedance |*Z*| frequency response for final TEM horn design with and without coaxial cable.

4.3 The TEM Horn Foil Prototype

Simulation results from the previous sections show a much higher impedance frequency response using the antenna dimensions described in [20]. Furthermore, increasing the width in the *w/h* ratio did not see any significant improvement in reducing its overall impedance. To validate the integrity of HFSS's simulation results, a physical prototype is constructed and its measured results plotted against the simulated ones. This prototype is constructed based on the triangular shaped TEM horn with a balun described in Phase II of the preceding section.

4.3.1 Construction of the Foil Prototype

The foil prototype of the TEM horn is constructed using copper foils shown in Fig 4.33. Thin sheets of copper foils are cut into isosceles triangular shapes with the bottom plate shaped accordingly into one with an integrated balun. An azimuth angle of 69° is used for this prototype. Subsequently, these copper sheets are adhered to a piece of Styrofoam, which is shaped to give an elevation angle of 32°. This Styrofoam is used as a support for the copper sheets, since its relative dielectric constant is same as air.

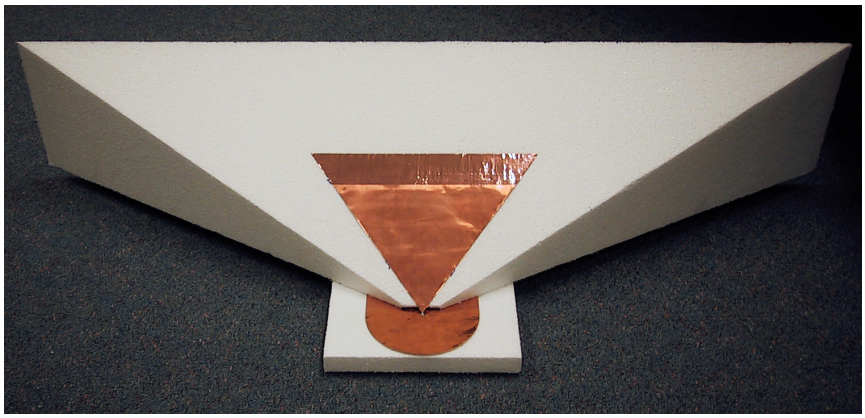

Fig 4.33. The Foil Prototype used for validating results from HFSS simulations.

The feedpoint of the TEM horn is constructed using a SMA stub contact panel socket from RS. Extra care was taken in the construction of the feedpoint since its preciseness will determine the antenna's performance at high frequencies. A section at the narrow end of the Styrofoam was truncated to allow space for the construction of the feed. The finished product is then tested with a HP8530 network analyzer in the anechoic chamber.

4.3.2 Measured Results

The impedance response of the TEM horn is measured using the HP8530 network analyzer, which is capable of giving impedance response over a user-specified range of frequencies. The network analyzer is first calibrated using short circuit, open circuit and broadband 50Ω stubs. This calibration compensates the attenuation and nonlinear effects in the cables and internal circuitries of the network analyzer. Once calibrated, the network analyzer is used to measure the impedance response of the TEM horn and a comparison between the measured and simulated results are shown in Fig 4.34.

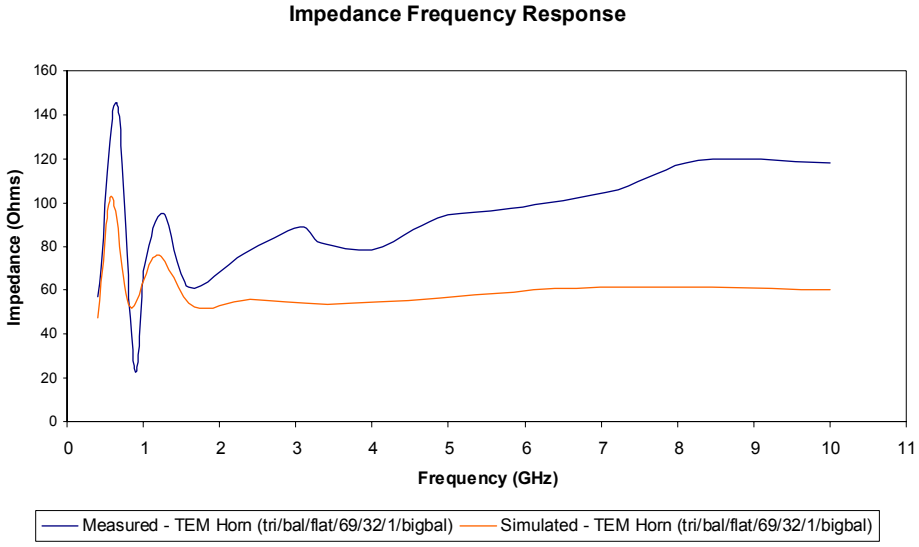

Fig 4.34. Comparison between the measured impedance |Z| frequency response of the foil prototype and its simulated equivalent.

Relatively similar impedance response is observed between the measured and simulated results. However, the measured impedance shows an increasing trend towards the higher end of the frequency range. The lack of preciseness in construction at its feed is deemed to be the cause of this discrepancy, since performance at high frequencies is extremely sensitive to the construction near the feedpoint region. Furthermore, the truncated section of the Styrofoam at the feedpoint region results in a lack of support on the flimsy copper material. Despite these discrepancies, the foil prototype exhibits similar trends in its impedance frequency response. Thus, it is sufficient to conclude that the results from HFSS simulations agree well with a practical model.

4.4 Summary

In this chapter, the evolution of a novel TEM horn design is described in three phases. Each design phase isolates the effects of dimensional changes on the antenna performance. Significant reduction in reflection within the antenna has been achieved by adding the wideband balun and shaping the antenna plates. In addition, the azimuth and elevation angles are modified throughout the entire design process to determine the dimensions that gives the best performance for each phase. The simulated results in HFSS for all models are in good agreement with theoretical reasoning. Results from HFSS simulations are also validated by a foil prototype, which provides a qualitative agreement with the simulated results.

Through a series of dimensional modifications, a UWB TEM horn using non-triangular plates was designed. These non-triangular plates were designed to compensate the effects of the wideband balun, which is essential in eliminating unwanted net flow current that results from an unbalanced-to-balanced transition from the coaxial cable to the antenna. Simulations in HFSS show that this model gives excellent matching over the range of 800MHz to an excess of 6GHz.

Chapter 5. Results: Final Design Prototype

Through a series of iterations, the final design is concluded using the TEM horn model with non-triangular plates. This model exhibits the best overall performance among the rest. Next, ways are devised to realize the physical construction of the antenna and methods of integrating this newly developed antenna onto the GPR system. This chapter will discuss various design aspect in constructing the TEM horn, which is fabricated by the staff in UQ Electrical Engineering Workshop.

Testing of the final physical prototype is conducted in an anechoic chamber, where its results will be compared against the simulated ones. A detailed discussion on the measured and simulated results will also be presented in this chapter to provide an argument on the discrepancies in results. Field results presented in this chapter serves as a measure on the success of this novel prototype.

5.1 Overall Physical Construction of the TEM Horn

5.1.1 Construction of the TEM Horn

The construction of the TEM horn is completely fabricated in the UQ Electrical Engineering Workshop, with the exception of the cable extension from the feedpoint to the panel socket at the plastic box. The completed version of the TEM horn is shown in

Fig. 5.1 and its design schematic can be found in Appendix B. The final design of the TEM horn consists of two bell shaped copper sheets separated by an elevation angle of 32°. This separation is held by a Styrofoam structure, cut to the specified elevation angle. The construction of this design is similar to the foil prototype, with the Styrofoam truncated at the narrowest section near the feedpoint to allow space for detailed work on the feedpoint. Styrofoam is chosen as a support since its relative dielectric constant is same as air, thus it does not affect the radiation characteristic of the antenna. A similar SMA stub contact panel socket used in the foil prototype is mounted onto the base of the bottom plate with its inner core soldered onto the tip of the top plate at its feedpoint. A separation of 1mm between both plates is used for reasons discussed in Chapter 4.

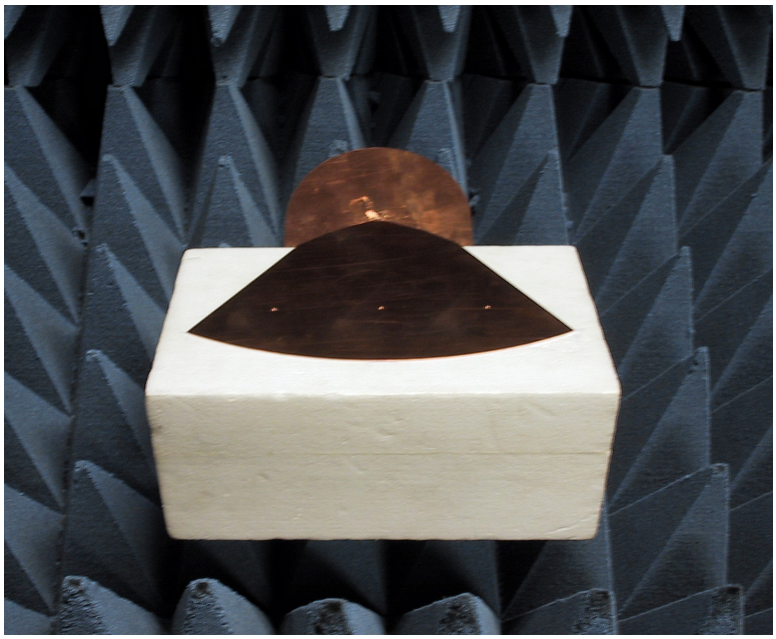

Fig 5.1. The final design prototype of the TEM horn. Picture taken against the background of the anechoic chamber.

5.1.2 Construction of the TEM Horn Holder

Integrating the TEM horn to the GPR system is not as straight forward as it seems. The most important consideration is the method of mounting the TEM horn without

affecting its performance. This proves to be a daunting task as the TEM horn is only connected by the tiny core of the panel socket and supported only by light Styrofoam. With some helpful advice from staff in the workshop, a box like structure is designed to hold the TEM horn shown in Fig. 5.2. A detailed schematic of this structure can be found Appendix B.

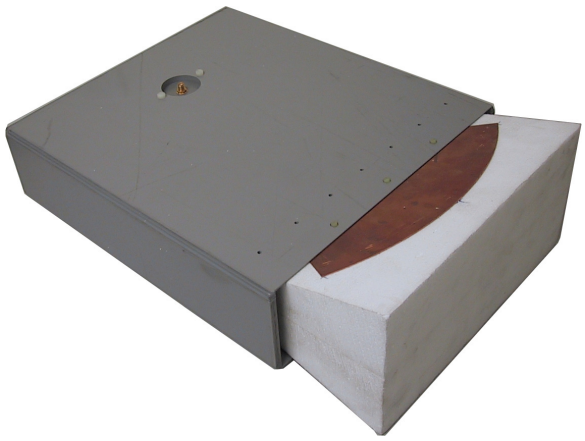

Fig 5.2. The final physical prototype with the plastic holder. The input SMA connector is shown on the top left corner of the picture.

This holder is made using 6mm plastic sheets and is designed to cover the entire TEM horn, leaving only one side of the box open for the mouth of the antenna. With this sturdy construction, the originally fragile TEM horn structure is now suitable for robust operations in rough terrains. The plastic box also acts as a medium for isolating any EM interference from metal structures such as the metal brackets and rails used for mounting the antenna.

In order to secure the TEM horn onto the box while still having the ability to remove it, three holes are drilled at the flared ends of each plate. These holes are small enough to avoid any significant changes in the antenna performance, since the holes are located near its flared ends, where its performance are less sensitive to small discontinuities. Before mounting the antenna into the box, a short coaxial cable extension that is capable of handling high frequency signals is connected to the socket of the TEM horn. This extension allows the antenna to be connected to the GPR system without the need to remove it from the box. Finally, the antenna is mounted onto the box, with the flared

ends of the plates secured by plastic screws. These plastic screws are used throughout the entire structure to avoid any unnecessary interference with the antenna operation.

5.2 Measurement Setup in the Anechoic Chamber

The anechoic chamber is an enclosure specially designed for taking RF measurements. Surrounded with walls that absorb radiation, this chamber creates a free-field environment, suitable for testing RF equipments, such as antennas. The walls of this chamber are covered with radiation-absorbing wedges to prevent multipath reflections when taking antenna measurements. In our study, only the far-field radiation patterns and gain frequency response are measured in the chamber. The impedance frequency response is measured using only the network analyzer.

Before any measurements are taken, the network analyzer is calibrated to compensate attenuation effects in the cables. An alternative method is used instead of the standard calibration procedure. First, a low loss, high frequency coaxial cable is connected between the sockets at both platforms. Then, the transmission loss, S_{12} of the total system is taken from 0 – 10GHz. This result will then be subtracted from the measured results for gain and radiation patterns. This method, however, neglects the loss of the cable, which is relatively small at low frequencies and about –1dB at high frequencies. Nonetheless, this method provides an easy way of calibrating the system with relatively good accuracy. Calibration for measurement of impedance frequency response follows the exact procedure of those described in Chapter 4 for the foil prototype.

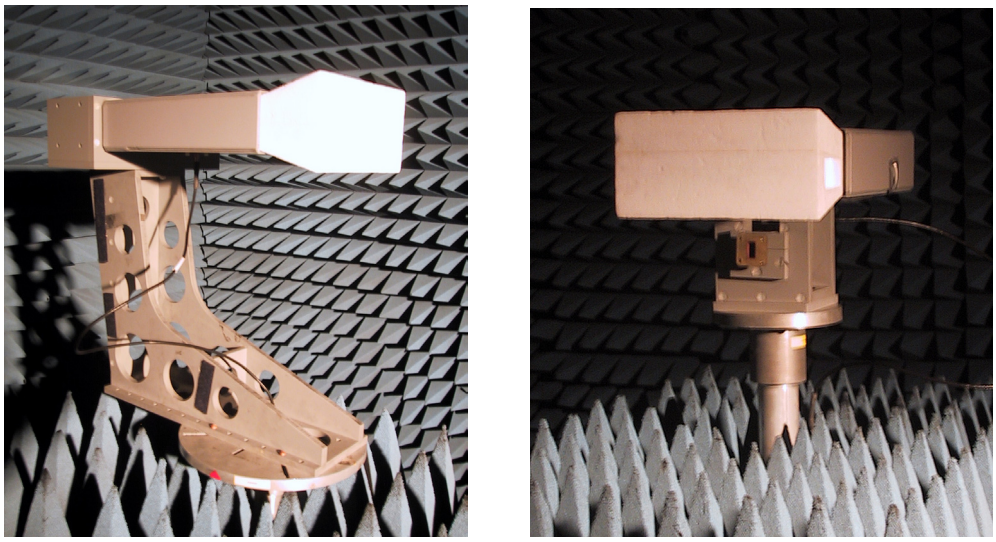

Fig 5.3. Mounting the TEM horn prototype in the anechoic chamber. The (a) measured antenna is mounted on the rotational platform and the (b) reference antenna on the translational platform.

Two platforms, each located at opposite ends of the anechoic chamber, are used to hold the antennas. The reference and the measured antennas are mounted on the translational and rotational platforms respectively. Mounting the reference TEM horn is relatively easy, as the platform remains stationary throughout the measurement procedure, thus the antenna can be secured on the raised flange using sticky tapes. On the other hand, the measured antenna has to be secured onto a bracket as shown in Fig 5.3 because the antenna will be rotated for measurement of the radiation pattern. Furthermore, the antenna has to be positioned such that its phase center coincides with the rotational axis of the platform to ensure that it is rotated around the axis, giving a more accurate reading of the radiation pattern. After securing both antennas, the translational platform is raised so that the both antennas are at equal height. This ensures the measurements taken are referenced directly from its boresight, hence giving a maximum reading. This procedure is repeated for measurements in cross and horizontal polarizations by changing the orientation of the antennas.

Having positioned the antennas into place, the measurements are taken via the network analyzer. A switchbox that is synchronized with the network analyzer is used to control the movement of the rotational platform. After the network analyzer is properly

configured, the rotational platform is set to run for one complete revolution with 1.2° steps. The radiation pattern, expressed in transmission loss, S_{12} is then read off the network analyzer and saved for further post processing. Taking the gain measurement is a much simpler task. By reading the transmission loss from the network analyzer console, the S_{12} values from 0 – 10GHz is calculated using the Friis' formula,

$$P_R = P_T G_T G_R \left(\frac{\lambda}{4\pi R} \right)^2 \tag{5.1}$$

where P_T and P_R are the transmitted and received power respectively. Similarly, G_T and G_R are the gains of the transmitting and receiving antennas. R is the distance between both horns in the anechoic chamber, which is found to be 2.5m. Since the transmission loss can be expressed as the ratio, P_R / P_T and the gain for both antennas are assumed equal; the gain of each horn can be expressed as,

$$G = \sqrt{S_{12}} \left(\frac{4\pi R}{\lambda} \right) \tag{5.2}$$

Obtaining the calibrated gain values is then just a matter of subtracting the calibration values off this calculated gain at their corresponding frequencies. Similarly, angular gain values for the radiation patterns are obtained using the same formula. Finally, the resulting sets of values are plotted in polar format using MATLAB.

5.3 Lab Results and Analysis

The results obtained in from the network analyzer are post processed with methods mentioned in the previous section before presented in this section. These results will be analyzed in detail before a comparison is made between the measured values and the simulated ones.

5.3.1 Measured Results in Anechoic Chamber

Gain

For a wideband antenna, a gain with flat response over the operating frequency range is desired. Putting them together, this gain frequency response over a range of frequencies determines its gain bandwidth. Bandwidth is usually defined as the -3dB points from its maximum value. However, this definition imposes strict limits to an antenna with wide range of operating frequencies. This is especially true with practical measurements in wideband antennas, where a short pulse-like gain response resulting from constructive interference will result in an inaccurate representation of the gain bandwidth. Thus, in our study, the definition of gain will be relaxed to compensate any irregularities in our measurements.

The measured results in gain frequency response is post processed and shown in Fig 5.4. In this plot, it is observed that a high level of attenuation is experienced in the lower frequency region. At about 800MHz, the gain reaches unity, after which it begins to rise and reaches a peak of 11.7dB before rolling off exponentially at about 5GHz. Taking the -3dB points off the maximum gain results in a bandwidth of only 1.8GHz, which does not even come close to the 5.2GHz bandwidth in the specifications. However, using a relaxed definition, a bandwidth of 3GHz can be achieved by taking the -3dB points from an averaged peak value. This value gives a more practical representation of the bandwidth.

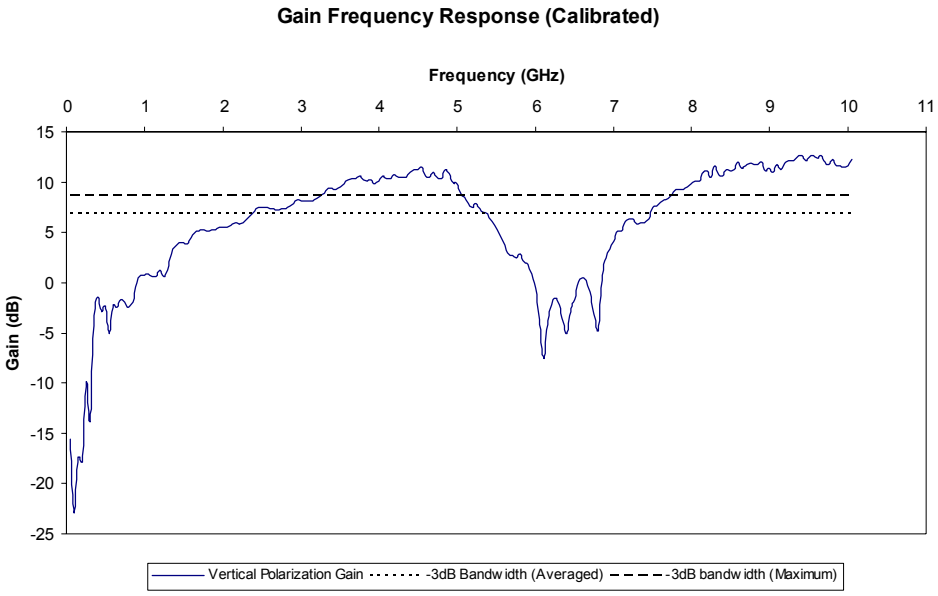

Fig 5.4. The impedance frequency response of the measured results for the TEM horn. The difference in bandwidth using different reference points is shown in this figure.

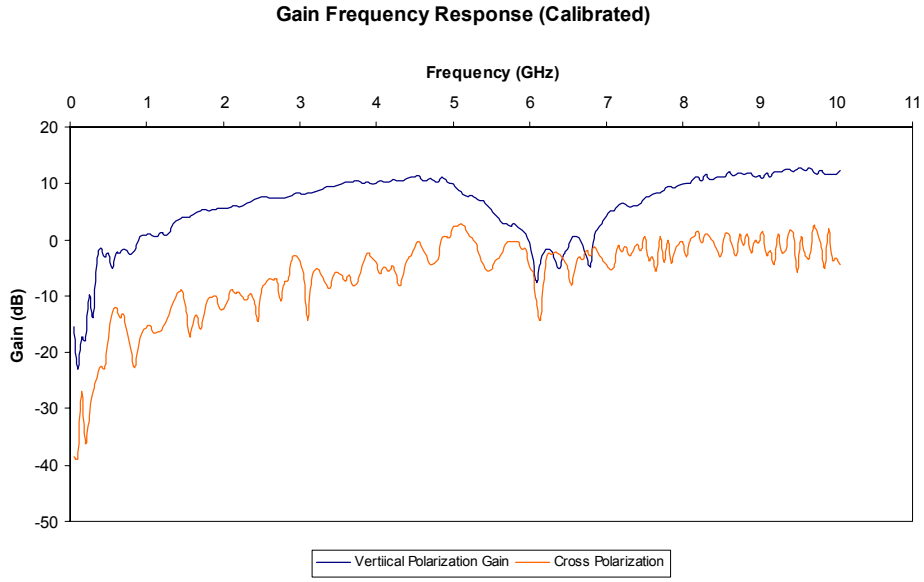

Fig 5.5. The gain frequency response of the measured results for the TEM horn with both co-polarized and cross-polarized orientation.

The gain response for cross polarization is obtained by taking measurements with the measured antenna tilted 90° off its boresight axis. From the results in Fig 5.5, it can be seen that the cross polarization gain of the TEM horn is below -5dB. The cross polar gain in this antenna is not critical as it does not generally degrade the performance of the UWB GPR.

Impedance

In the earlier section, discussions on the construction of the TEM horn show that the TEM horn itself lacks the mechanical strength to be useful in any field applications. In order to protect the TEM horn in rough terrains, part of the horn, including the feedpoint is contained within the plastic box. Therefore, a short coaxial cable extension is used to link the feedpoint to a panel socket located at the bottom of the plastic box. This extra length of cable introduces an electrical delay, which in turn changes the phase of the signals from the feedpoint.

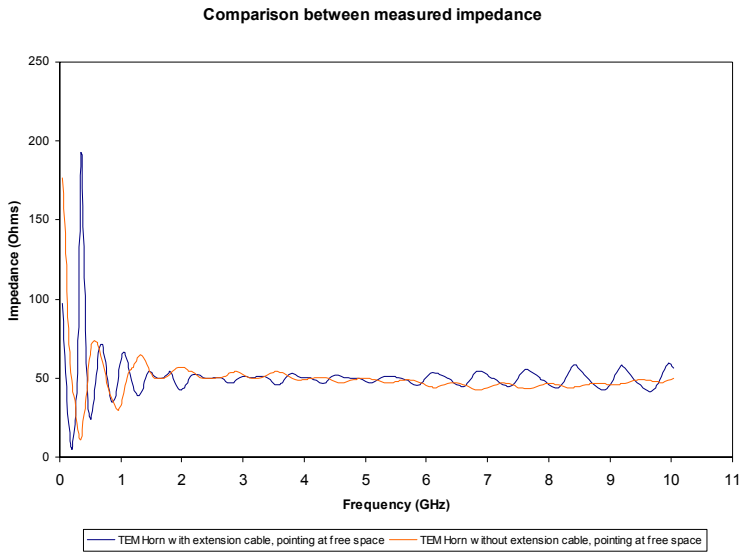

Fig 5.6. The impedance |*Z*| frequency response of the measured results for the TEM horn. This plot shows a comparison between the TEM horn measured with and without the extended coaxial cable.

As shown in Fig 5.6, the TEM horn exhibits good matching at about 50Ω with and without the extension cable. For measurements taken at the end the extension cable, the impedance shows more pronounced oscillations about 50Ω, especially towards the higher frequencies. Nonetheless, it produces a good impedance match, with values between 45Ω and 55Ω. This corresponds to a reflection coefficient below -7dB ranging from 800MHz up to 10GHz. On the other hand, the results for the model measured directly at its feedpoint exhibit a more damped impedance frequency response compared to the model measured from the end of the extension. The damped effect is attributed to the absence of the extra electrical length from the extension cable. However, small amounts of oscillations still exist. This may be due to the extra length of the pin in the SMA connector. Due to its operation in extremely high frequencies, this pin still contributes a significant amount of electrical length, which explains the existence of the fluctuations. Similarly, a comparison between the reflection coefficients of the antenna shows no significant effects to the extension cable.

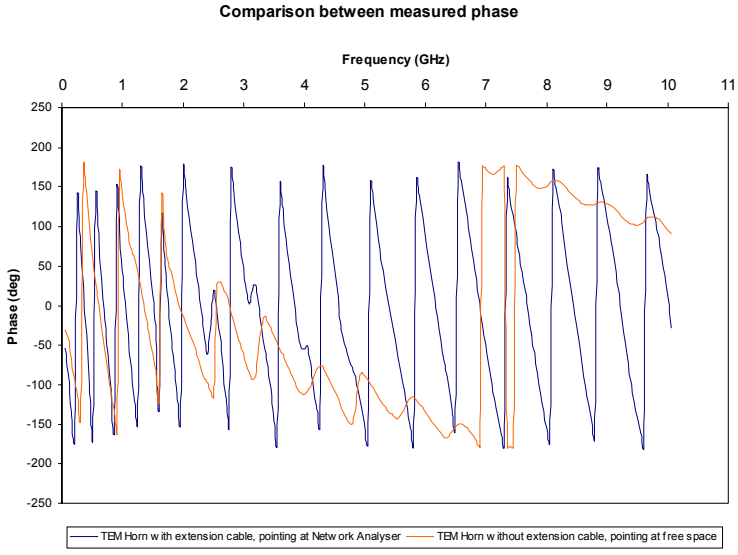

Fig 5.7. The phase frequency response of the measured results for the TEM horn. This plot shows a comparison between the TEM horn measured with and without the extended coaxial cable.

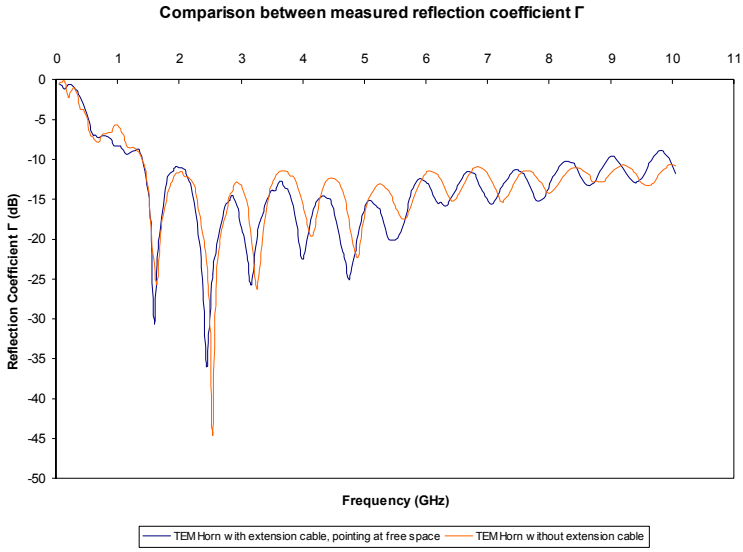

Fig 5.8. The reflection coefficient frequency response of the measured results for the TEM horn. This plot shows a comparison between the TEM horn measured with and without the extended coaxial cable.

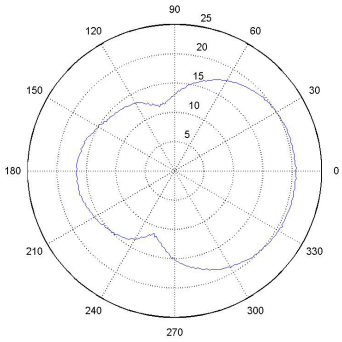

(a)

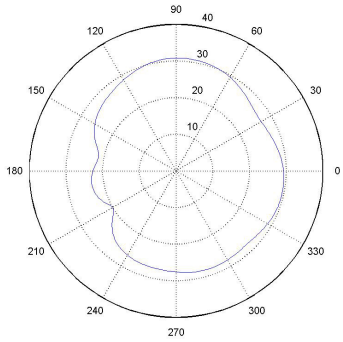

(d)

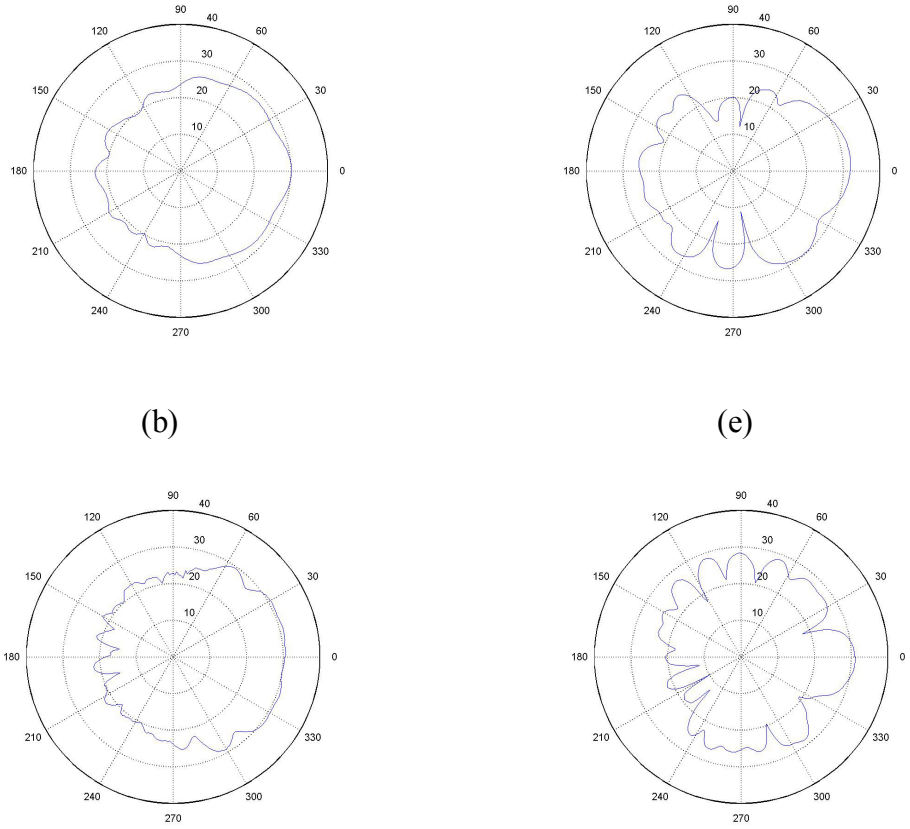

Fig 5.9. The above plots show the measured radiation patterns of the TEM horn. The left and right column shows radiation patterns at frequencies of 1GHz, 3GHz and 5GHz for the H-plane and E-plane respectively. These values are expressed in Gain+20dB.

Radiation Patterns

The radiation patterns in the H-plane show a wide beamwidth symmetric about its boresight for all frequencies measured. At 1GHz, the gain at boresight is about 1dB, which is relatively low. However, the gain increases with frequency, with values approaching 10dB at 3GHz and 5GHz. At all the measured frequencies, the TEM horn exhibits a very wide beamwidth of about 120°. The antenna also shows good suppression of sidelobes, with magnitudes generally falling below 0dB.

In the E-plane, the antenna produces non-symmetrical radiation patterns about its boresight. This is expected as the wideband balun contributes to the non-symmetrical structure of the antenna when referenced from its E-plane. The angular gain at boresight for the 1GHz, 3GHz and 5GHz is found to be about 10dB, 12dB and 11dB respectively. From the radiation pattern, it is observed that there is a mass concentration of sidelobes at the feedpoint above the balun, indicated by the 150° mark in the radiation plots. This is due to the excess radiation caused by current dissipating through the balun shown in Fig 4.24. The beamwidth at 1GHz, 3GHz and 5GHz are about 120°, 60° and 30° respectively.

5.3.2 Discussion of Results

Overall, the measurements in the final TEM horn prototype produced satisfactory results although some outcomes were unexpected. The main parameters under investigation are the gain frequency response, impedance frequency response, reflection coefficient frequency response and its beamwidth. This section will discuss the measured results and a comparison with the simulated results from HFSS.

Gain

As mentioned earlier Chapter 4, the gain given in HFSS is referenced with the maximum value in the radiation pattern instead of its value at boresight. To provide a quantitative comparison between both measured and simulated results, the simulated gain has to be approximated in the radiation plots. A comparison on the gain frequency response between the measured and simulated results shows a relatively similar trend in the response curve. However, the simulated results show a more subdued fluctuation in gain performance between 5 – 7GHz. The significant drop in gain at these frequencies was not accurately reflected in the plots. Careful investigation on the simulated results show that due to the lack of sampled points, the frequency response in this range are completely omitted, thus generating erroneous data in the simulation results. Thus, the simulated results do not represent a true reflection of the actual performance of the

antennas due to the lack of sampling points. However, simulated results at the low frequency region, where more log sampling points are concentrated show a higher gain than the measured results for the final design prototype. An investigation on the beamwidth at 1GHz did not provide any source on this discrepancy. However, it can be observed that the simulated results have a trend of producing similar frequency responses as the measured results, but at a lower frequency as shown in Fig 5.13. This may have resulted in the difference observed in the lower frequency region. Although the simulated results only show qualitative agreement with the measured results due to a lack of sampling points, it still provides a very good approximation on the performance of the TEM horn.

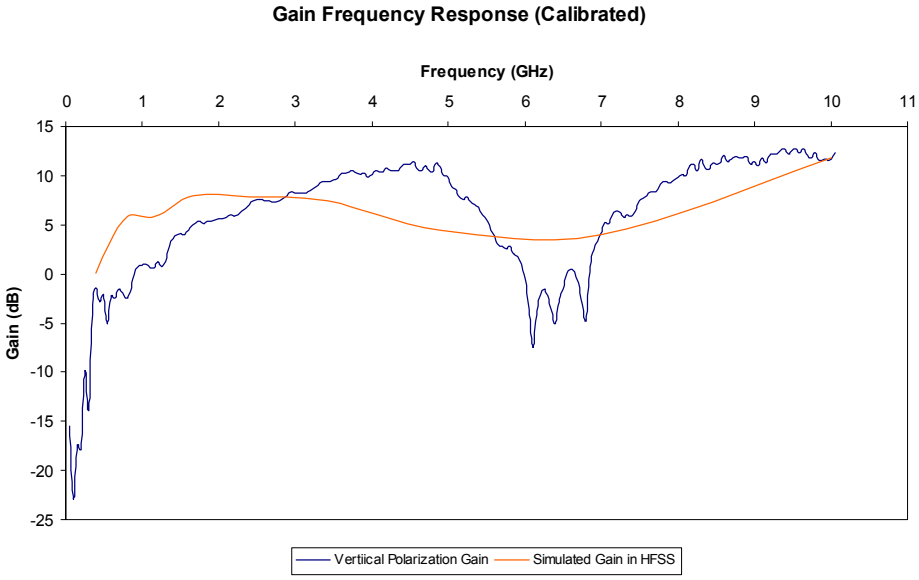

Fig 5.10. The impedance frequency response for the measured and the simulated results for the TEM horn prototype.

Impedance

The impedance frequency response of the antenna has the biggest impact on the antenna performance. A mismatch in the antenna will result in ringing problems, which causes incorrect information to be fed to the GPR system. A false target indication due

to antenna ringing may be fatal in landmine detection applications. Therefore, the impedance is the foremost parameter to be optimized, and sometimes result in some trade-off in performance in other aspects, such as gain and beamwidth.

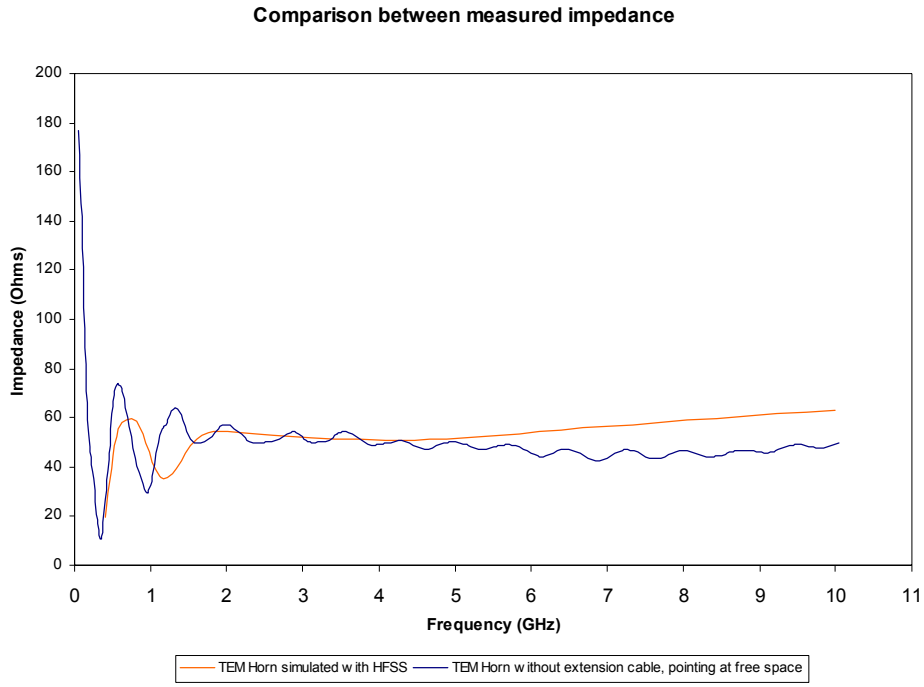

Fig 5.11. The impedance |Z| frequency response of the measured and simulated results for the TEM horn. The measured results from the model without the extension cable is used.

From the previous section, it can be seen that the impedance frequency response of the antenna for both the TEM horn with the and without the extension cable gave very similar results, except for some oscillations at high frequencies due to the extra length of cable. In HFSS, the TEM horn is simulated using a point source at its feed. Thus, in order to provide the comparison with best accuracy, the measured result without the extended cable will be used. The result of this comparison is shown in Fig 5.11. From this comparison, it can be concluded that the simulation results gave a very accurate prediction of the measured impedance response. The only discrepancy occurs above 5GHz, where the simulated result rises with frequency. The constant performance in impedance frequency response in the final design prototype will provide a good match with the 50Ω load, minimizing errors due to reflections.

Reflection Coefficient

An alternative method to quantify the performance of the antenna is through its reflection coefficient. This parameter is related to the impedance of the antenna and the load, and is often used to characterize the performance of the antenna. Generally, only the magnitude of the reflection coefficient is analyzed. The reflection coefficient of a transmitting antenna defines the percentage of incident power reflected back to the feed. In our study, if the TEM horn is mismatched, a high reflection coefficient will result at the frequency where the mismatch occurs. When power is reflected back to the antenna at its antenna-air interface, a fraction of the power will be reflected back to the aperture. This causes a fraction of the transmitted power to resonate within the horn, thus resulting in serious signal distortions if the reflection coefficient is large. Reflections within the antenna contribute to the overall ringing problem in a UWB GPR system. Since there is nothing much one can do to reduce the reflections at the antenna-air and air-ground interface, the only way to reduce ringing is to minimize its contribution to the phenomenon. This is achieved by a good impedance match at the feedpoint of the TEM horn.

As shown in Fig 5.12, the measured reflection coefficient agrees very well with the simulated values. The exponential decreases in the measured values are due to a near perfect match at those frequencies. In the simulated results, however, these were not shown due to the lack of sampled points. Overall, the TEM horn performs very well in its reflection coefficient response over a wide range of frequencies.

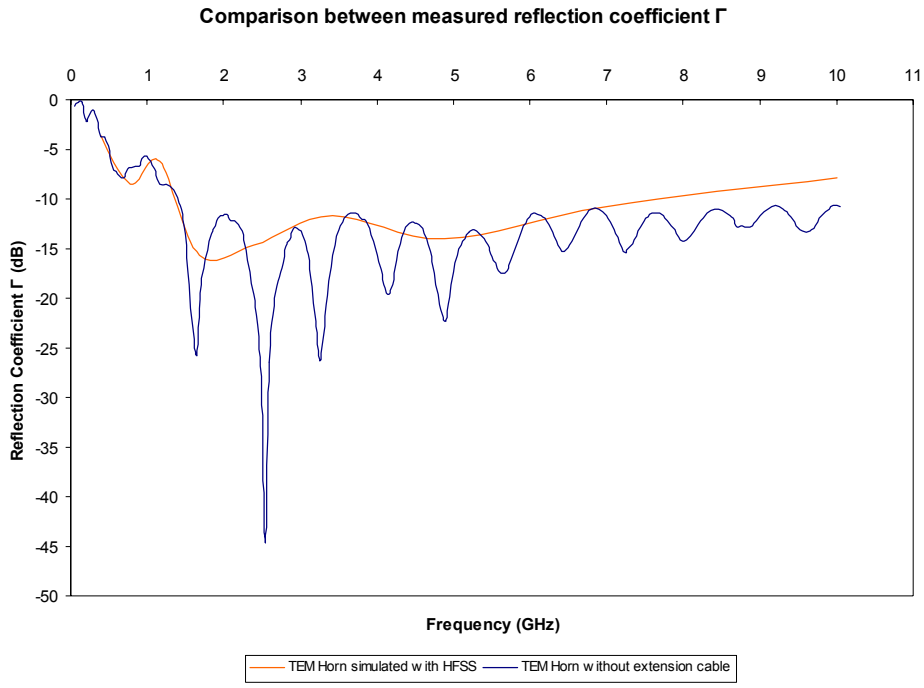

Fig 5.12. The reflection coefficient frequency response of the measured and simulated results for the TEM horn.

Radiation Patterns

The beamwidth of the UWB TEM horn plays a crucial role in determining the performance of the GPR system. Recall from Chapter 1 that the TEM horn will be integrated with a SF-GPR using SAR processing. The SAR processing of the GPR system uses the averages of a series of echoed pulses to detect a single object. This calls for an antenna with wide beamwidth so as to provide maximum coverage over the area under test.

From the results in the simulation shown in Fig 5.13(b), a 5dB drop in gain at its boresight at 5GHz is observed. Although the measured results at 5GHz did not show any drop in gain, it can deduced from the gain frequency response in Fig 5.14 that there will be a significant drop in gain at the boresight between 5 – 7GHz. In HFSS, the gain is referenced from the maximum value, regardless of direction. Therefore, an analysis on the results in Fig 5.13 shows that despite the formation of a null at its boresight, the

sidelobes generates a relatively high gain. With the formation of the null at boresight, the overall beamwidth of the antenna reduces by the fraction where the null exist. In general, this is highly undesirable in any radar system. However, the SAR utilizes an extremely broad beamwidth in detecting a target, thus the reduction in beamwidth only affects a fraction of the data collected off the reflected object at its corresponding frequency. As a result, this reduction in gain does not cause a significant decline in the performance of the GPR.

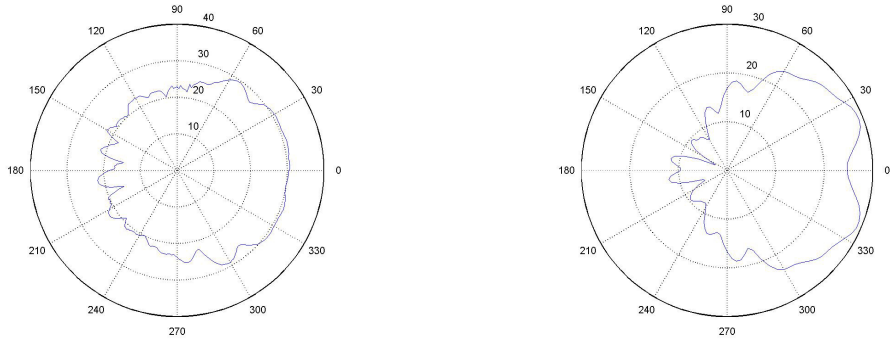

(a) (b)

Fig 5.13. The radiation patterns of the (a) measured and (b) simulated results for the final design prototype at 5GHz. These values are expressed in Gain+20dB.

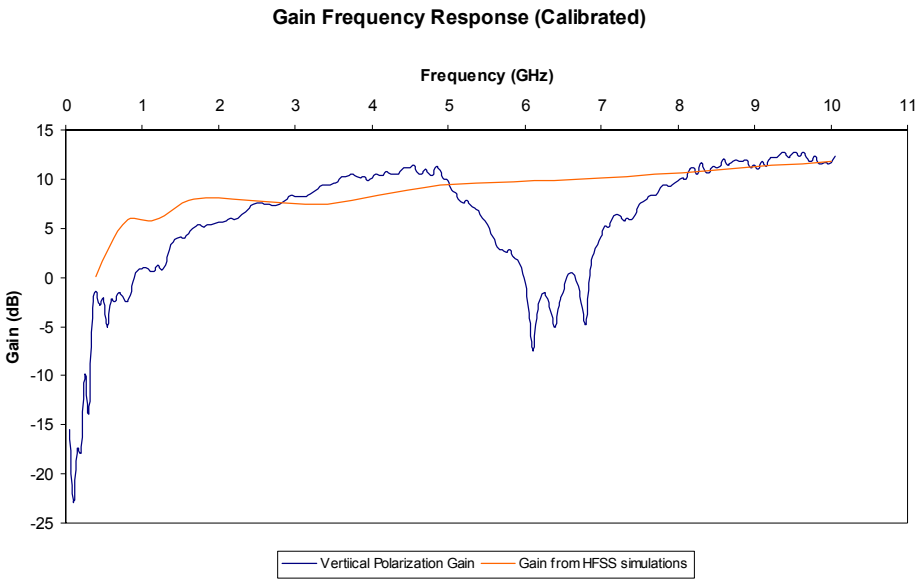

Fig 5.14. The gain frequency response of the measured and simulated results for the TEM horn. The measured gain is referenced from its boresight while the simulated gain is referenced from its maximum value.

5.4 Field Results and Analysis

5.4.1 Field Test Setup

With the success in the measurement results, the TEM horn prototype is integrated with the GPR system to measure its field performance. The GPR system from the UQ Mining Sensors Group CSSIP consists of a network analyzer, a PC and the antennas. These equipments are mounted onto a trolley and placed onto a set of tracks in the field shown in Fig 5.15. The network analyzer is used for performing FFT conversions from frequency to time domain as the trolley is moved down the tracks. These results are further SAR processed by the PC to produce a SAR filtered image. An example of the raw SAR image is shown in Fig 1.3. Subsequently, these results are post processed using more complex algorithms to provide an accurate location of the target.

(a) (b)

Fig. 5.15. The field setup of the GPR. The (a) GPR is mounted on a trolley and pushed along the rails while the (b) network analyzer and the PC do the computations.

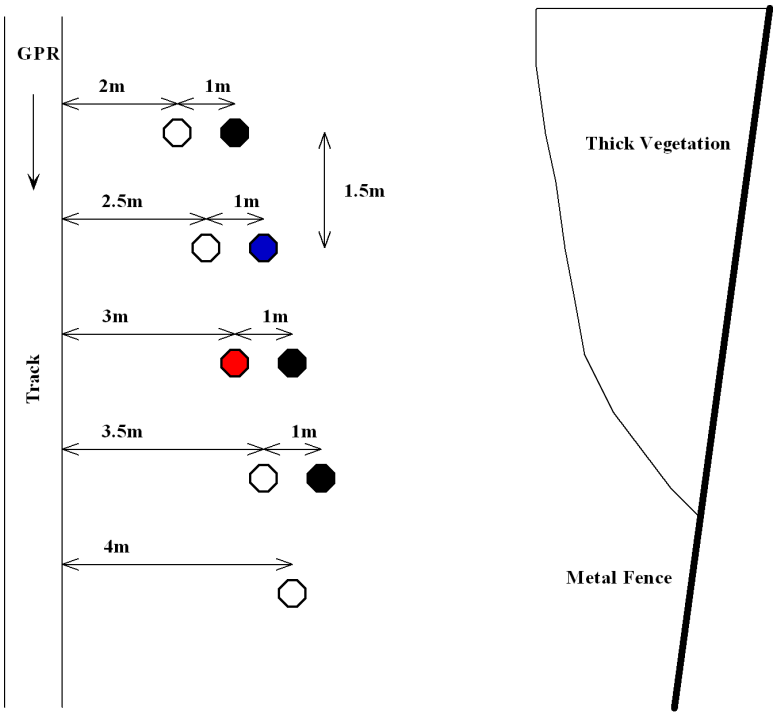

Fig 5.16. Position of the dummy landmines during field testing. The shaded circles indicate metal spheres while the rest indicates plastic cylinders. The red circle indicates a larger metal sphere and the blue circle indicates the "landmine" to be buried.

Several solid plastic cylinders and metal spheres about 10cm in diameter are placed along the path of the radar's radiation field. These objects are equally spaced with incremental distance from the radar as it moves towards the end of the track shown in Fig 5.16. The systematic placement of these objects allows us to identify them in the resulting plots of this test. Before the test begins, a survey on the surrounding environment shows extremely high moisture content in the soil due to rain prior to the day of the test. This means that there is a high chance that the GPR may not be able to detect the objects if they are buried underground, since EM pulses are susceptible to high attenuation in wet soil.

5.4.2 Measured Results from Field Testing

Several sets of measured results are taken during the field test, each with different parameters shown in Table 5.1. Its corresponding SAR processed results are shown in Fig 5.17 with circles to indicate the position of the objects. The SF-GPR is configured to transmit pulses from 1GHz to 5GHz.

Figure	Antenna	Polarization	Height (cm)	Comments
5.16 (a)	TEM Horn	Vertical	70	All surface objects
5.16 (b)	TEM Horn	Vertical	90	All surface objects
5.16 (c)	TEM Horn	Horizontal	82	All surface objects
5.16 (d)	TEM Horn	Horizontal	82	With buried object
5.16 (e)	Double Ridged Horn	Vertical	90	With buried object
5.16 (f)	Double Ridged Horn	Vertical	90	With buried object

Table 5.1. Parameters for different sets of measurement results.

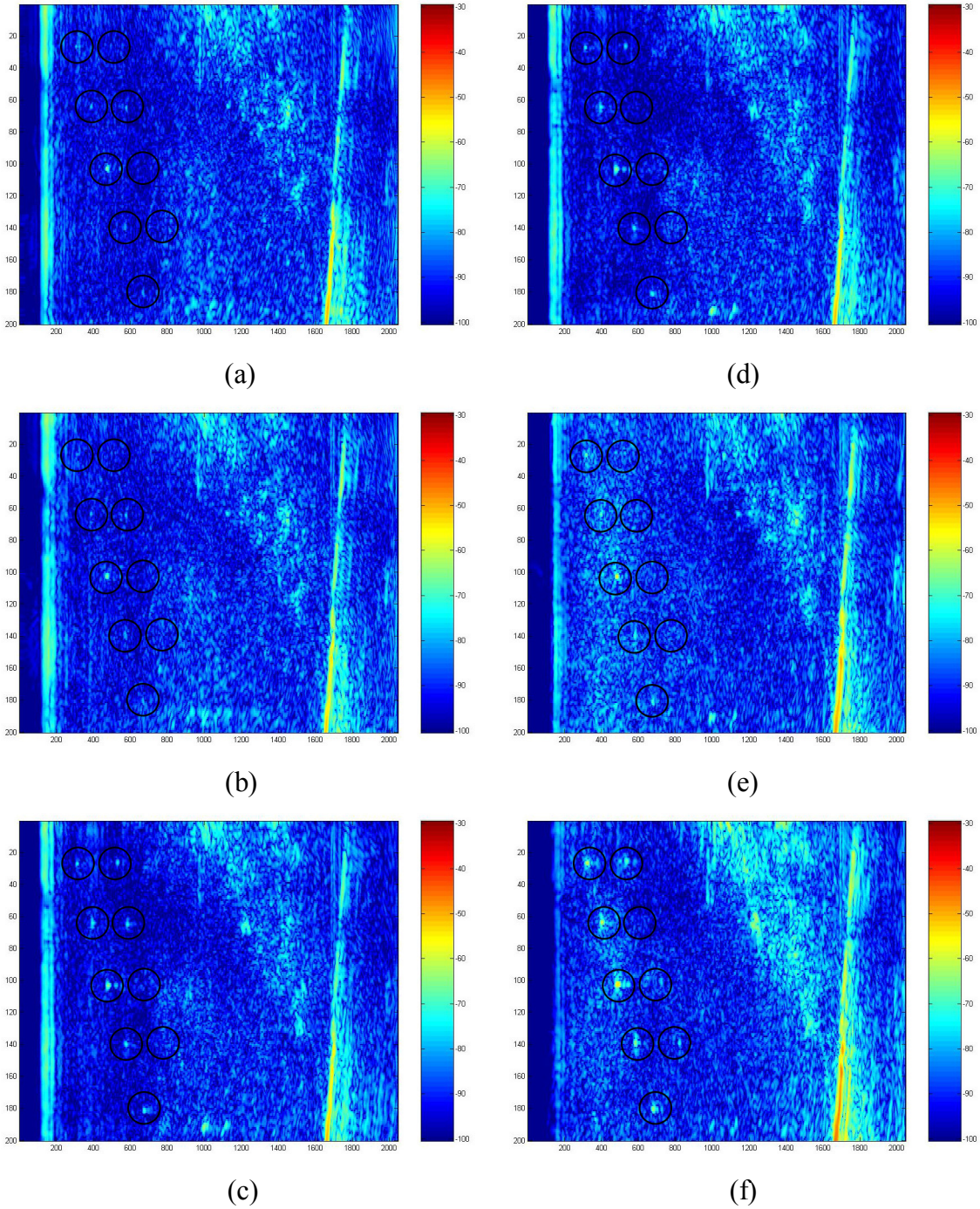

Fig 5.17. The SAR images using the TEM horn and double ridged horns in various polarizations and heights.

The SAR processed results shown in Fig 5.16(a) using vertical polarized TEM horn at 70cm above ground shows very weak reflections on most targets, except for the large metal sphere. From Fig 5.16(b), results for the same configuration with the height

raised produced similar results. In Fig 5.16(c), a much higher reflection from the objects results from the horizontally polarized antennas. As seen from the graphical plot, almost all the targets are clearly visible, except for the one behind the large sphere and the one furthest from the track.

With these results, a further step is taken by burying a small metallic sphere shallowly as indicated in Fig 5.16. Unfortunately, results shown in Fig 5.16(d) indicate an absence in reflection from the buried object due to extremely lossy soil. With the metal sphere still buried underground, similar measurements were taken using the double ridged horns. The measured results using vertically polarized double ridged horns in Fig 5.16(e) shows a relatively high level of clutter around the surface objects but shows no signs of the buried object. Furthermore, this vertically polarized antenna also show a lack of reflections for the object behind the large metal sphere and the furthest metal sphere. A brief comparison between the results shows that this antenna achieves a higher received power compared to the TEM horn. Finally, the measured results from the horizontally polarized double ridged horns exhibit a high contrast between the ground and the surface objects. However, the buried object still remains undetected.

5.4.3 Discussion of Results

From the results in the preceding section, it is obvious that a horizontally polarized antenna produces better results. The increased in performance is attributed to the structures of the surrounding vegetation and the targets. All objects possess their unique polarization signature and these signatures provide information on the way radiation scatters off its surface. Thus, different antenna polarizations result in the difference in reflection intensity of the object. Furthermore, when the wave hits an object, its reflected wave may go through a series of multipath reflections before it gets received by the antenna. These multipath reflections sometimes result in a change in polarization, which goes undetected when using a co-polar antenna configuration.

The results in our field experiment show that short grass near the targets reflects better with vertically polarized waves while the thicker vegetation near the fence exhibits

higher scattering intensity with a horizontally polarized wave. This is particularly obvious when the double ridged horn is used. For the TEM horns, a less pronounced effect is observed with the change in polarization. This may be attributed to its non-constant gain frequency response. The lower frequencies, which mainly affect the detection of larger structures, such as the thick vegetation, are unable to produce any significant effects due to its low gain. Contrastingly, the higher frequencies, which generally affect small objects, such as the targets, result in a more pronounced effect due to its high gain.

In all except the 5.16(f), the metallic sphere furthest from the track went undetected. A survey on the test area suggests that the low hanging branches above that particular object may have contributed clutter that interferes with its detection. In addition, the moisture on these branches further increased the magnitude of its interference. However, in Fig 5.16(f), the object results in a relatively weak indication using horizontally polarized wave. This may be attributed to a higher gain with the double ridged horn antennas. The field results also show an absence of the target behind the large metal sphere. This target may be obscured by reflections from the large metal sphere, which greatly reduces its magnitude of reflection.

Overall, the TEM horn prototype performs comparatively well with the double ridged horns over a frequency range of 1 – 5GHz. Due to the lack of gain at low frequencies, the TEM horn produces less changes in large objects with a change in polarization.

5.5 Summary

A novel design of the TEM horn is being designed and developed. The physical construction of this antenna includes a plastic box-like structure, which is designed to hold the antenna onto the GPR system and provide shielding against EM interference as well as protection in rough terrains. Testing of this TEM horn prototype is accomplished in the anechoic chamber and results show relatively good frequency response for its impedance, gain and beamwidth. These results also provide good

agreement with the simulated results, even though there were some discrepancies found in its gain frequency response. Field testing using these novel antennas has shown comparatively good results with the double ridged horns as a benchmark.

Chapter 6. Evaluation

Development of these TEM horns did not stop with the final design. Evaluation work has been carried out even after the antenna has been sent for fabrication. Compiling results from past simulations, methods are employed in an attempt to correct the imperfection in its performance. Although these improved versions will not be fabricated, its evaluation allows us to predict the magnitude of improvement over the current version. This chapter provides an insight to the imperfections of the current prototype and the evaluation models that address some of these problems.

6.1 Analysis of Areas for Improvement

From the preceding chapter, the prototype has produced results that are in good agreement with the simulated model. However, due to limitations in the simulation program and the lack of computing power, several problems were overlooked. The foremost problem that plagues the current prototype is its gain frequency response at boresight between the frequency ranges from 5 – 7GHz. Measured results from the prototype showed a more pronounced dip in gain over that frequency range due to the lack of sampling points. A thorough investigation on all existing and new simulation results shows that this dip may be attributed to the inclusion of the balun and the non-triangular shape of the antenna plates. From the radiation patterns in Fig. 6.1(a), a slight dip in gain at the boresight can be observed at 5GHz with the inclusion of the balun. Furthermore, this dip becomes more pronounced using the model with non-triangular

plates shown in Fig. 6.1(b). The radiation patterns suggest that null at boresight is caused by an angular deviation of the main lobe at 5 – 7GHz, which results in splitting of the beam. In order to remedy this problem, the aperture length is reduced so that the formation of this null will not occur at the wavelengths corresponding to these frequencies as suggested in theory in Chapter 2. This change in aperture affects the azimuth and elevation angles, dimensions of the balun and the overall shaping parameters of the non-triangular plates.

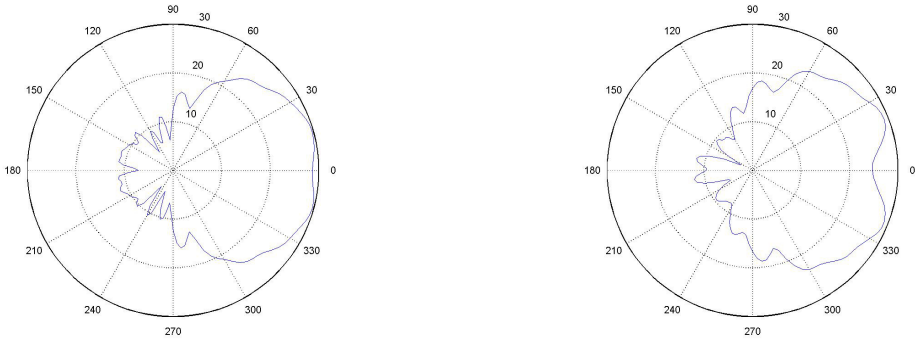

Fig 6.1. Radiation patterns for the TEM horn with triangular and non-triangular plates at 5GHz. These values are expressed in Gain+20dB.

The second consideration is to increase the frequency impedance performance of the antenna at high frequencies. From the initial designs, it was assumed that a separation of 1mm at the feedpoint is sufficient to maximize the high frequency performance as well as keeping its physical construction mechanically possible. An evaluation on the physical prototype reveals that this separation can be further reduced due to the physical properties of the SMA stub panel sockets. An excess length from the pin to the Teflon layer means that the feedpoint separation can be effectively reduced to zero shown in Fig. 6.2.

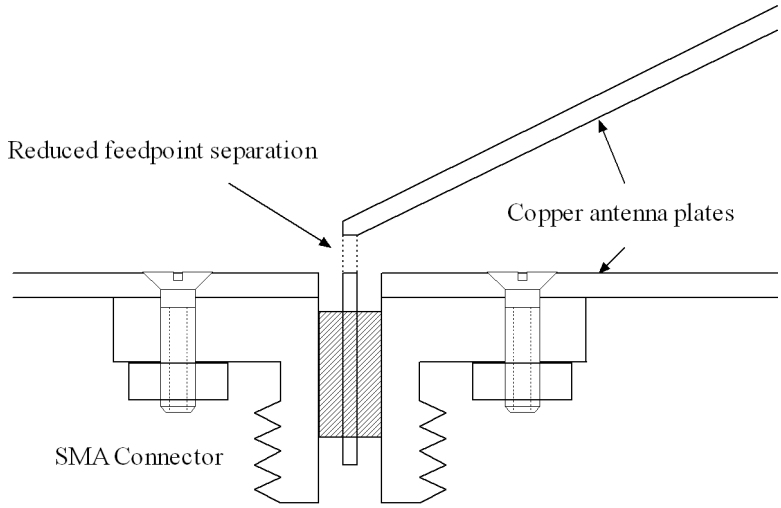

Fig 6.2. A cross section view of the feedpoint. The dotted line shows the reduced feedpoint separation and the shaded area shows the Teflon layer.

6.2 Simulated Results of Improved Models

From the discussion in the last section, several changes were made to the prototype design and simulated in HFSS. Simulated results from two models are shown here to show the effects of the modifications made. The first model is designed using the same parameters of the final prototype with its feedpoint separation, $B = 0$. Simulation results from Fig. 6.3 show a decrease in impedance from 1 – 10GHz, which is particularly significant above 5GHz. The change in feedpoint separation gives the impedance frequency response a constant performance over more than three octaves. However, this change also shows a slight overall reduction in impedance throughout the entire range of frequencies. The gain performances are not shown because they are not susceptible to slight changes in feedpoint separation as discussed in Chapter 4.

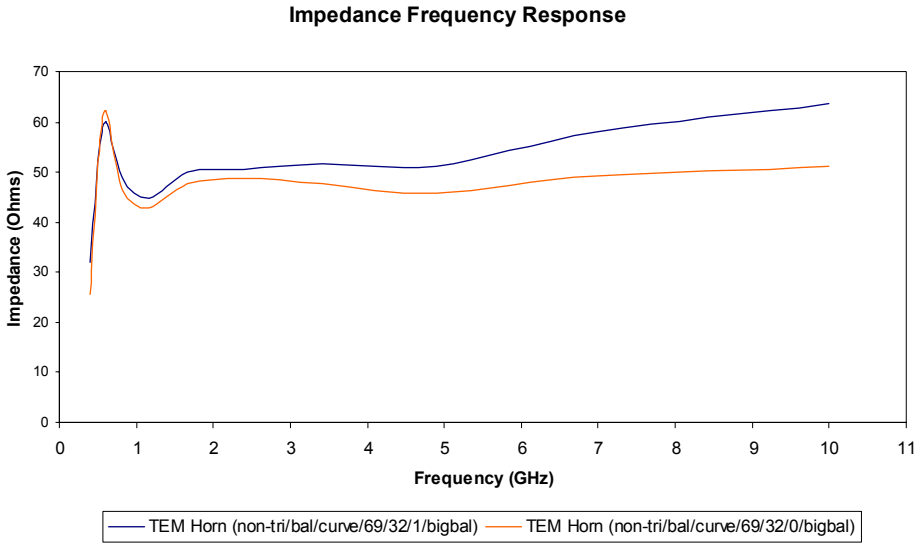

Fig. 6.3. Impedance |Z| frequency response for TEM horns with different feedpoint separations.

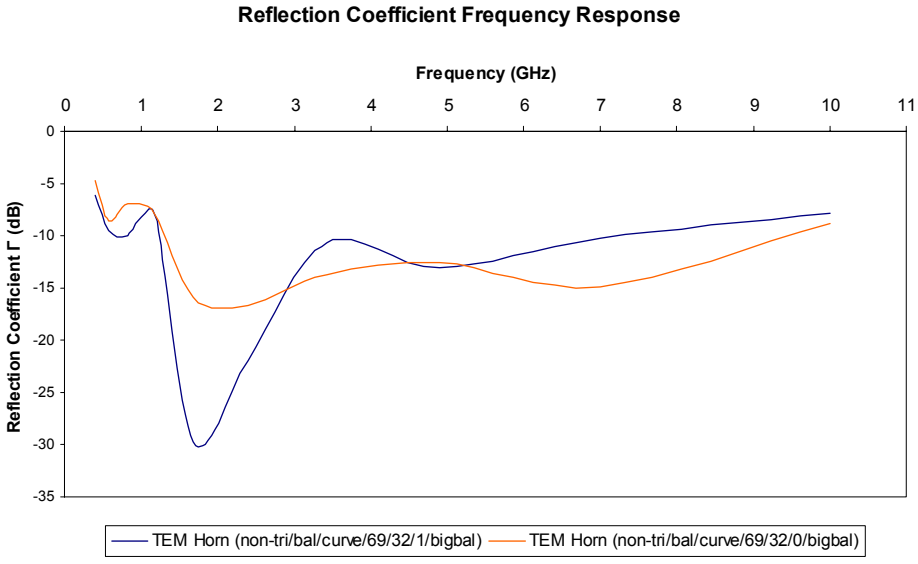

Fig. 6.4. Reflection coefficient frequency response for TEM horns with different feedpoint separations.

The second model in this evaluation phase consists of changes in both the azimuth and elevation angles and the feedpoint separation. Changes in *w/h* ratio, dimensions of

balun and the shaping parameters of the non-triangular plates are made to fine tune the performance of this model. Through a series of design iterations, the design with the following dimensions are found to produce the best overall performance,

- Azimuth angle, $\alpha = 54.2°$
- Elevation angle, $\beta = 20°$
- Radius of balun, $r = 50$cm
- Feedpoint separation, $B = 0$

The simulated results from this evaluative model in Fig 6.5 show a reduction in overall impedance frequency response as compared to those from the final prototype. However, this slight decrease in impedance is still within the tolerable levels above 1.5GHz. From the gain frequency response in Fig 6.7, the evaluation model shows a constant performance from 2GHz before experiencing a drop in gain about 7GHz.

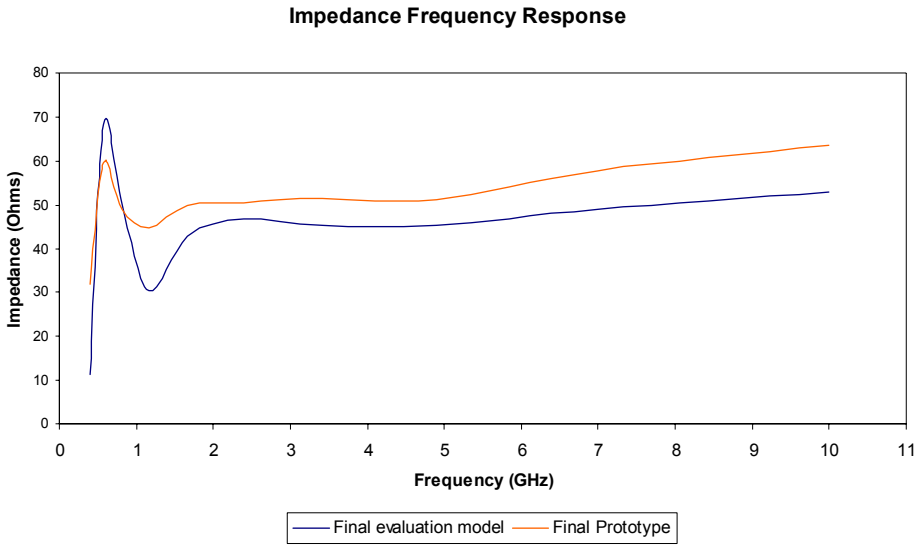

Fig. 6.5. Comparison of impedance |Z| frequency response for TEM horns for the final prototype and the final evaluation model.

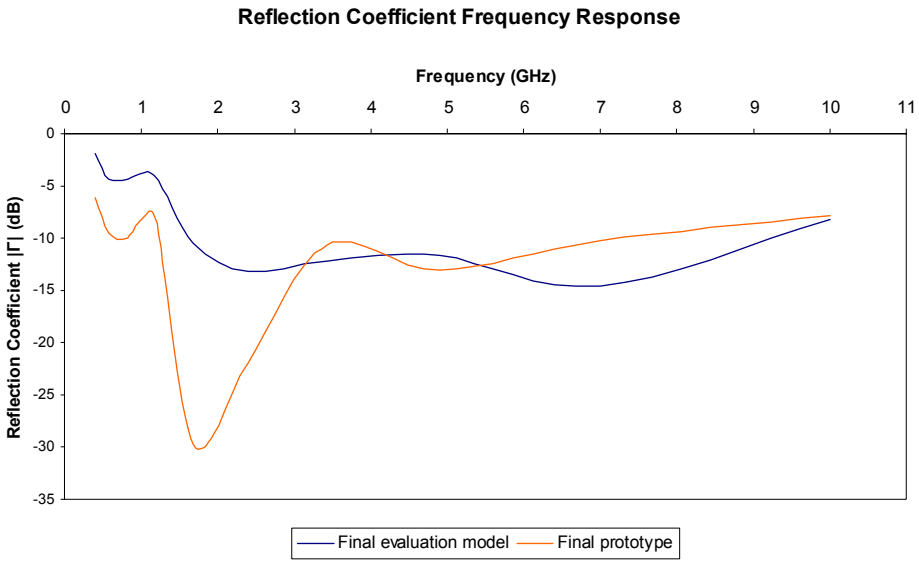

Fig. 6.6. Comparison of reflection coefficient frequency response for TEM horns for the final prototype and the final evaluation model.

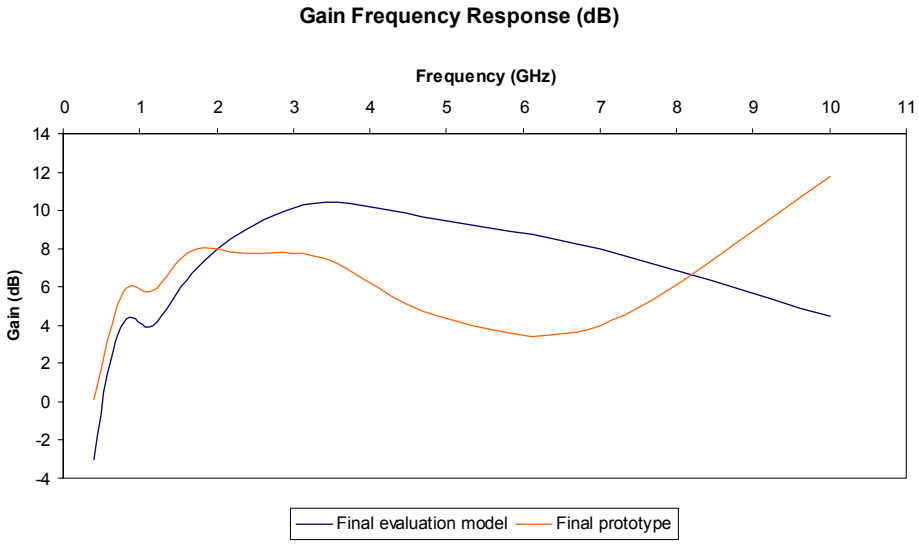

Fig. 6.7. Comparison of the gain frequency response for TEM horns for the final prototype and the final evaluation model.

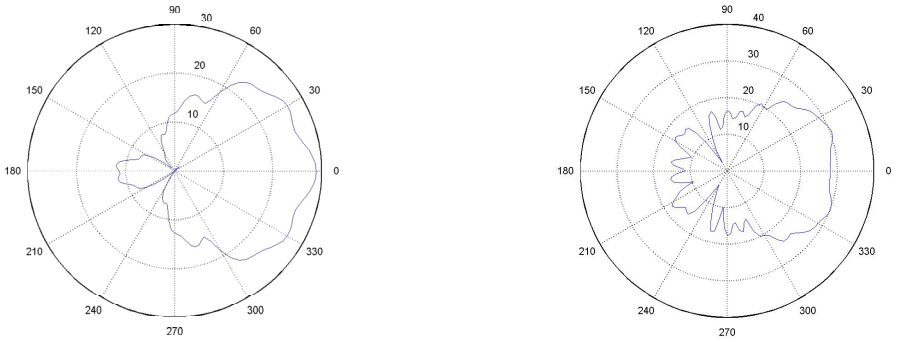

Fig. 6.8. Radiation patterns of the final evaluation model at (left) 5GHz and (right) 7GHz. These values are expressed in Gain+20dB.

6.3 Discussion

From the results of the new model, an increase in gain frequency performance over the final prototype is observed. This increase in performance results in a trade-off in its impedance frequency response. However, the decrease is insignificant and is kept within tolerable levels. Since there is a direct dependence between the beamwidth, wavelength and the size of its aperture at its corresponding frequency, thus, the reduction in aperture size in the evaluation model results in the formation of the null at a frequency above 7GHz. This effectively increases the gain bandwidth of the TEM horn by 2GHz at the upper end of the frequency range. In addition, the reduction in separation distance at the feedpoint contributes to an improved performance in impedance frequency response. Overall, this evaluation model has proven that an improvement in performance can be achieved over the final prototype, which exhibits a relatively high degradation in gain from 5 – 7GHz.

6.4 Summary

An evaluation model of the TEM horn is developed in this chapter in an attempt to improve the performances over the final prototype. Through intuitive reasoning and analysis of previous simulation results, an improved version of the final prototype is successfully modeled in HFSS. This model exhibits relatively flatter gain frequency response over its predecessor. With a reduction in aperture size, the improved model produces almost a twofold increase in gain bandwidth by eliminating the drop in gain from 5 – 7GHz that is present in the final prototype. Furthermore, it was also shown that further decrease in feedpoint separation results in an increase the performance of the impedance frequency response. This evaluation version serves as a starting point for any future development of this TEM horn model.

Chapter 7. Conclusions and Future Work

7.1 Conclusion

Analysis of Ultra-Wideband antennas departs from conventional understanding of antenna operations, which transmits data through sinusoidal waveforms. The requirements for such wideband characteristics simply mean that a carrier free signal or impulse waveform is transmitted. A special category of antennas, known as the frequency independent antennas are employed to radiate fast EM transients required in applications such as UWB GPRs. One such candidate is the TEM horn, which produces relatively high gain and wide beamwidth over a wide range of frequencies. These characteristics make it an ideal antenna for a UWB GPR system using SAR imaging.

In this thesis, a novel UWB TEM horn has been presented. Based on empirical methods, this new model has been developed through numerous iterations on a software simulation package. The design methodology of this new prototype has been based on mostly intuitive reasoning and a clear understanding of electromagnetic waves and fields. Through a series of carefully planned simulations, an analysis of the TEM horn is achieved based on simulated results. The accuracy of this experimental analysis of the TEM horn has been proven in this thesis from its measured results.

Through this thesis, a different approach to the design of an UWB TEM horn has been developed based on purely empirical methods. In conclusion, the aim of this thesis has

been achieved through the completion of a successful design and a complete analysis on its results.

7.2 Future Work

In the evaluation of this thesis, work to increase the performance of the intended design is disrupted due to the lack of time. However, this could be taken as the starting point of any future work. A continuation of this work can be summarized in the following points,

1. Based on the evaluation model, the overall reduction in impedance frequency response can be corrected by using a lower *w/h* ratio. This decrease will further give room for reducing the aperture size, which will give rise to frequency at which the null occurs.
2. The detection process is conducted in close proximity with the targets. This means that the antenna may be radiating in the near-field region, where the radiation fields are spherical. Ideally, a planar wave is desired. This can be achieved through a gradual taper of a short section of the antenna plates towards $\beta = 0°$ at its flared ends.
3. From the results achieved, it can be seen that the change in dimensions of the antenna do not usually improve the performance at lower frequencies. Thus, a vast improvement in antenna performance can be achieved if the dip at 5 – 7GHz is eliminated. With this, the length of the antenna can be scaled, thus shifting its frequency response towards the lower end by the scaling factor. A suggested solution is to taper the antenna plates into a teardrop shape with its length increased. This massive reduction in aperture may eliminate the null from the frequencies of interest.

Appendix A

Simulation results from HFSS do not give the impedance |Z| frequency response of the antenna. Thus, its given S_{11} parameter, referenced with 50Ω is post processed using transmission line equations to give the value of the impedance. The values from HFSS can be obtained in the polar format,

$$|\Gamma| \angle \theta$$

Since the reflection coefficient S_{11} is expressed in,

$$S_{11} = \Gamma = |\Gamma| e^{j\theta}$$

And

$$e^{j\theta} = cos\,\theta + j\,sin\,\theta$$

Thus, the value of Γ is obtained in its complex form. Following this, the antenna's impedance $|Z_L|$ can be calculated using,

$$|Z_L| = Z_o \frac{1+\Gamma}{1-\Gamma}$$

These values are plotted in Microsoft Excel and plotted against frequency.

Appendix B

In this section, the schematics for the TEM horn prototype and its holder will be shown. These schematics are drawn to scale.

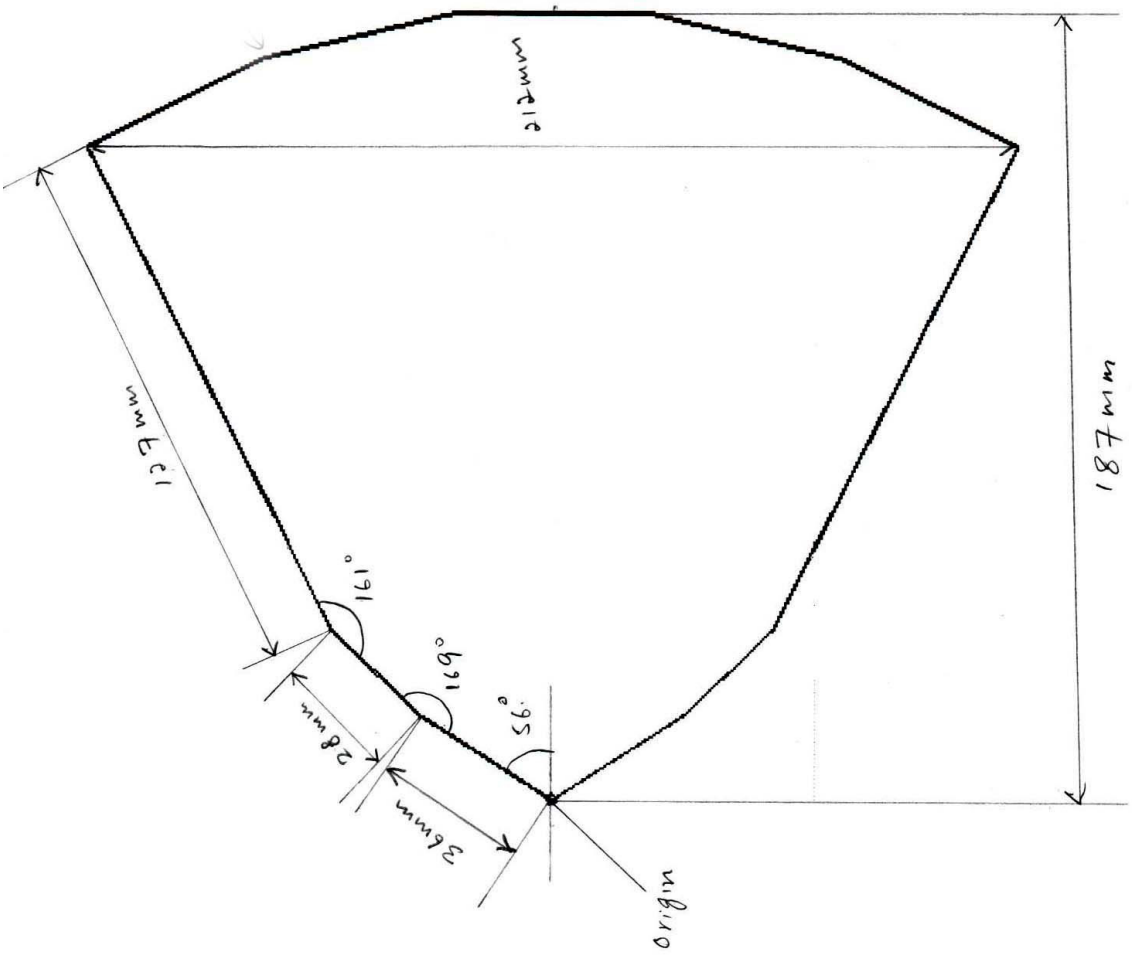

B.1. Top plate of the TEM horn prototype.

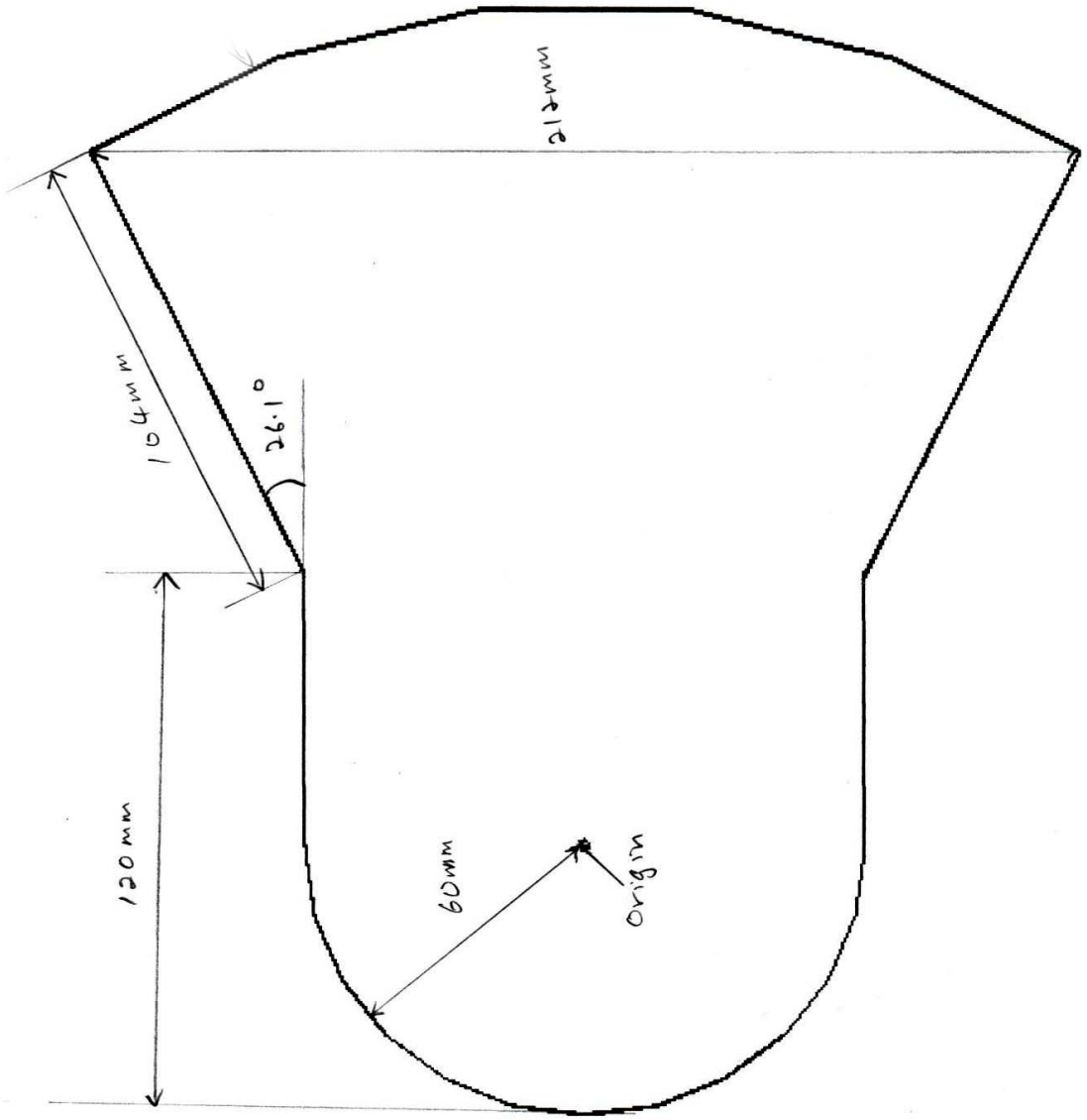

B.2. Bottom plate of the TEM horn prototype.

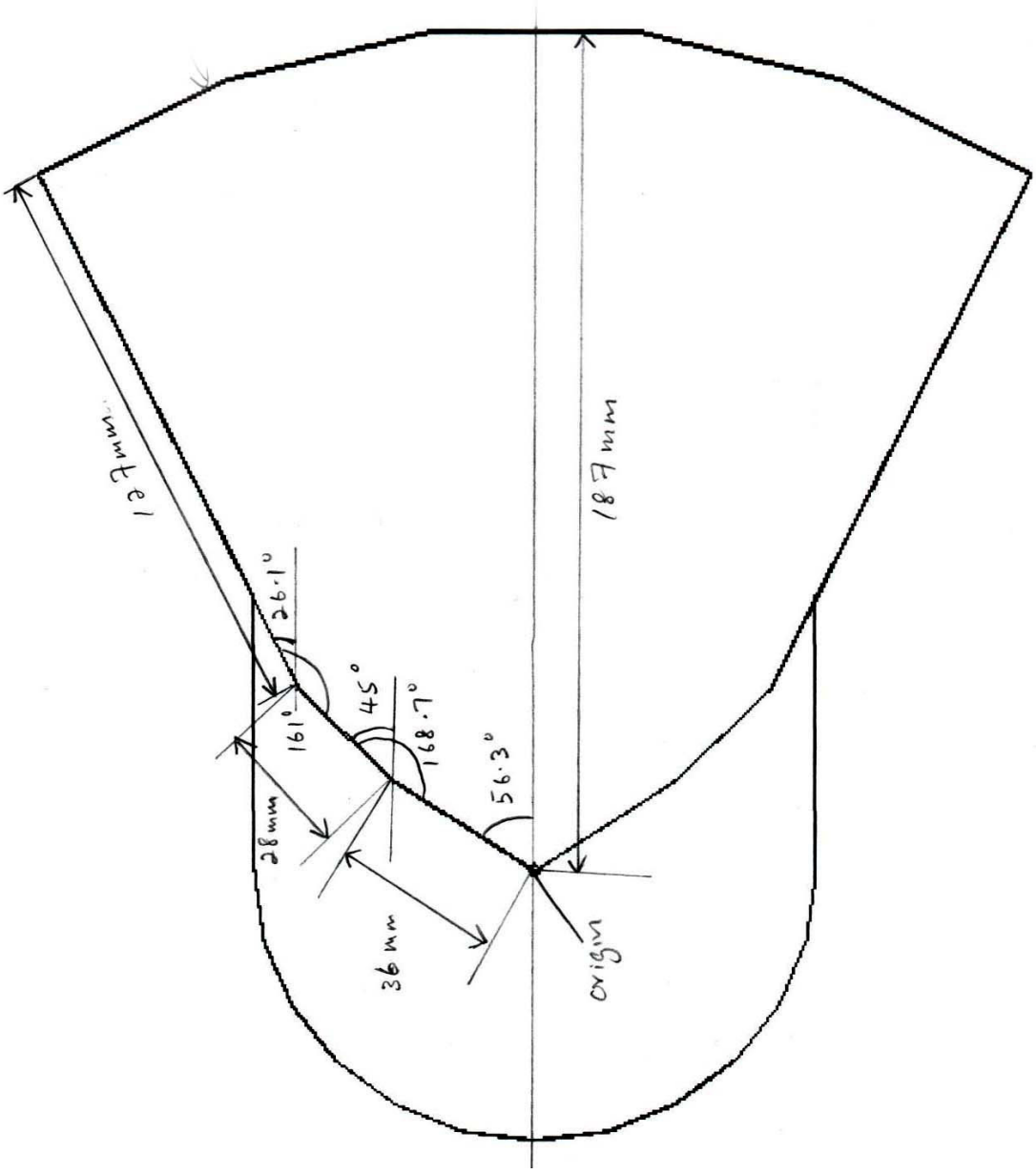

B.3. Top view of the TEM horn prototype.

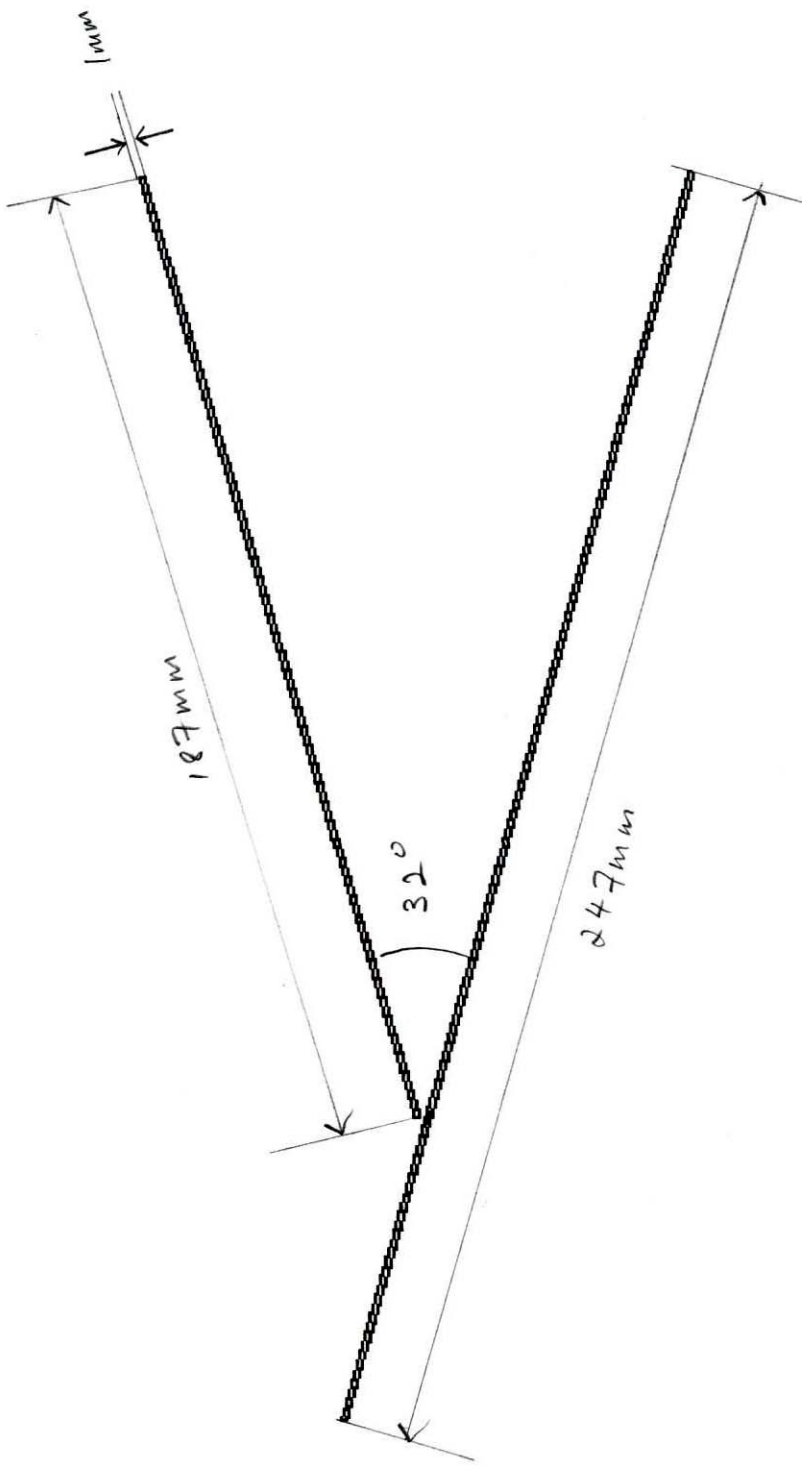

B.4. Side view of the TEM horn prototype.

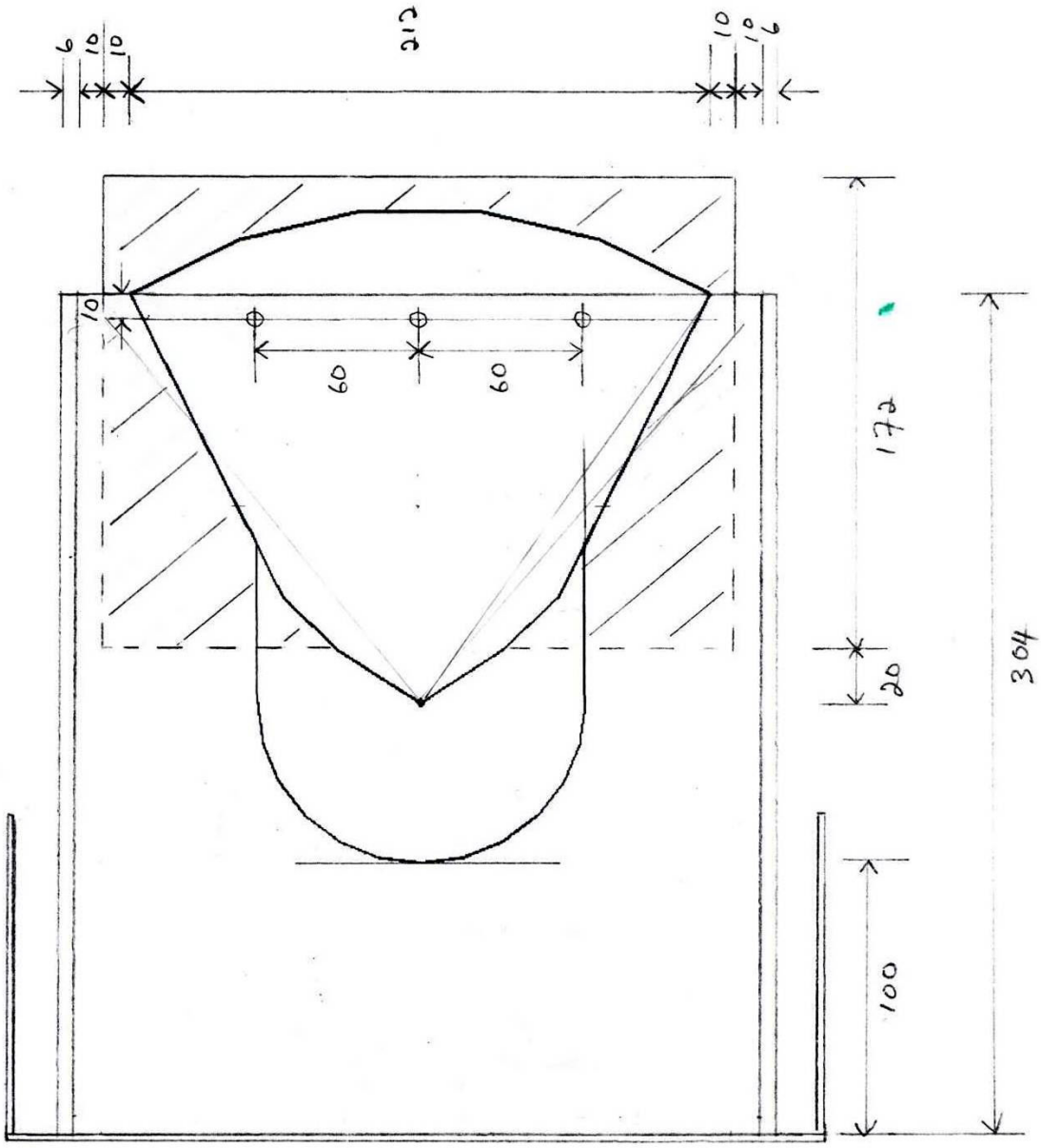

B.5. Top view of the TEM horn prototype with in the plastic holder and bracket.

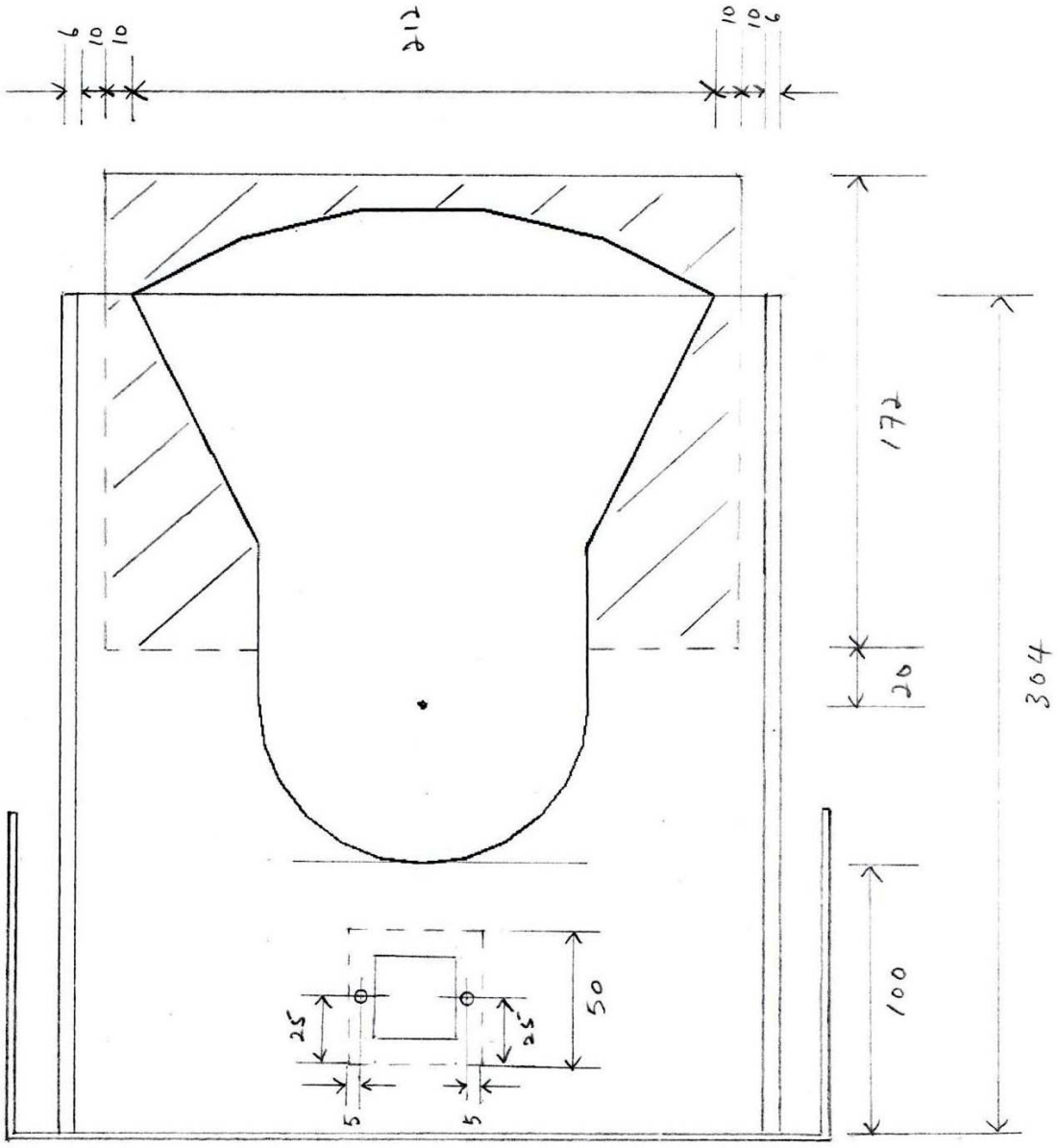

B.6. Bottom view of the TEM horn prototype in the plastic holder and bracket.

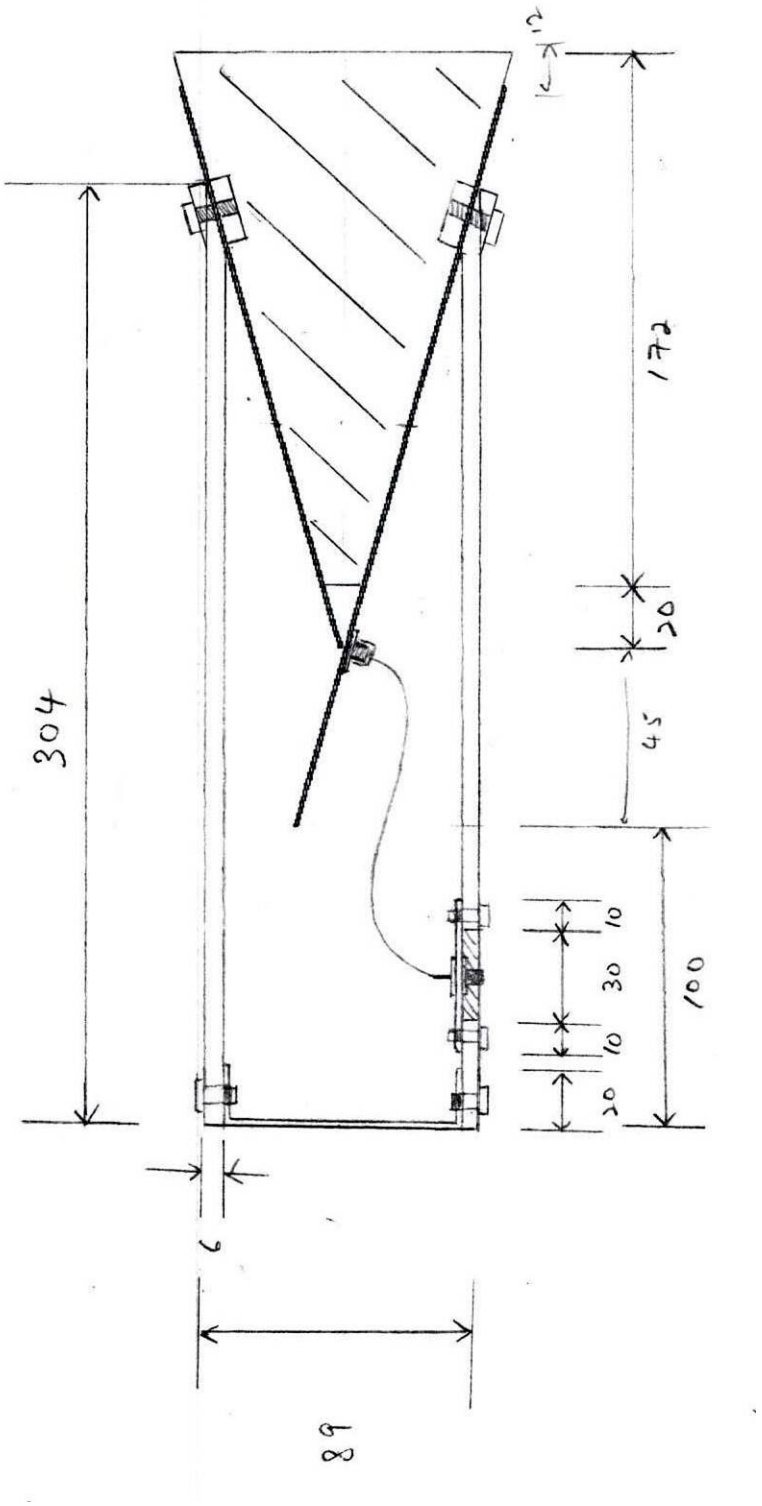

B.7. Side view of the TEM horn prototype in the plastic holder and bracket.

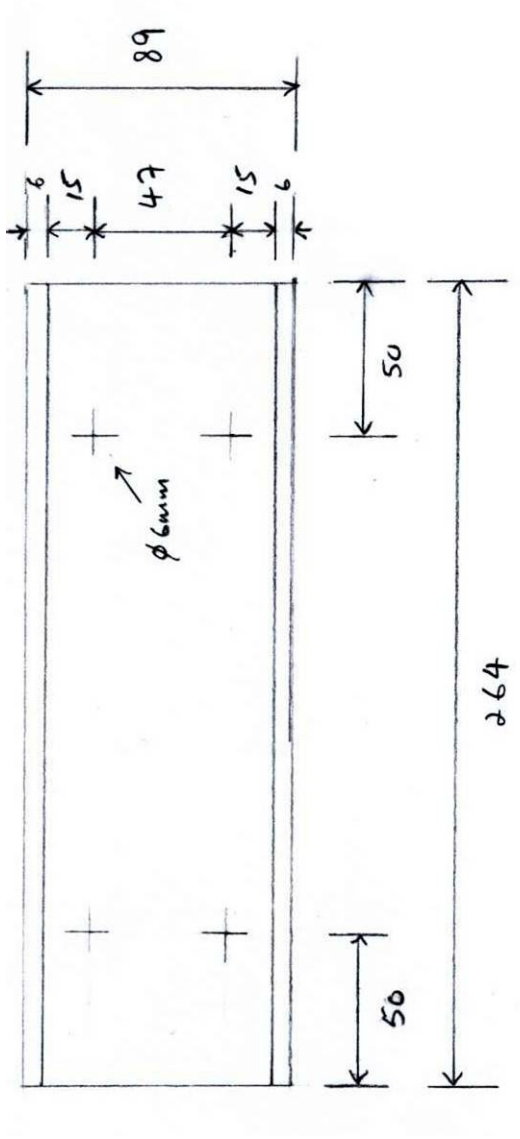

B.8. Back view of the TEM horn prototype in the plastic holder and bracket.

References

[1] US Department of State, "Hidden Killers 1998: The Global Landmine Crisis," Http://www.state.gov/www/global/arms/rpt_9809_demine_ch3a.html (current Oct. 21, 2001).

[2] United Nations Foundation - Impact of the Global Landmine Crisis, http://www.unfoundation.org/campaigns/landmines/index.asp (current Oct. 21, 2001).

[3] M. Charlton, "Small-Scale Soil-Moisture Variability Estimated using Ground Penetrating Radar," *Proc. 8th Int. conf. GPR,* Gold Coast, Australia, May 23-26, 2000, pp. 798-804.

[4] B. Scheers, *Ultra-Wideband Ground Penetrating Radar, with Application to the Detection of Anti Personnel Landmines*, Royal Military Academy, Brussels, Belgium, Dept. Electrical Engineering and Telecommunication, 2001.

[5] M. Cherniakov, L. Donskoi, " Frequency Band Selection of Radars for Buried Object Detection," *IEEE Transactions on Geoscience and Remote Sensing*, vol. 37, no. 2, pp. 838 - 845, March 1999.

[6] L. Donskoi, *Modeling and Optimisation of Stepped-Frequency Ground Penetrating Radar***,** University of Queensland. School of Computer Science and Electrical Engineering, 1998.

[7] V. Rumsey, *Frequency Independent Antennas*. New York: Academic Press, 1966.

[8] M. Kanda, "The Effects of Resistive Loading of "TEM" Horns," *IEEE Transactions on Electromagnetic Compatibility*, Vol. EMC-24, No. 2, May 1982, pp. 245-255.

[9] G. F. Stickley, D. A. Noon, M. Cherniakov, and I. D. Longstaff, "Preliminary field results of an ultra-wideband (10-620 MHz) stepped-frequency ground penetrating radar," in *Proc. IGARSS'97*, vol. III, pp. 1282-1284.

[10] S. Evans and F.N. Kong, "TEM Horn Antenna: Input Reflection Characteristics in Transmission," *IEE Proceedings*, vol. 130, Pt. H, No. 6, Oct. 1983, pp. 403-409.

[11] P.J. Gibson, "The Vivaldi Aerial," in *Proc. 9th Eur. Microwave Conf.*, Brighton, U.K., Sept.. 1979, pp. 101-105.

[12] B. Stockbroêckx and A. V. Vorst, "Copolar and Cross-Polar Radiation of Vivaldi Antenna on Dielectric Substrate," *IEEE Transactions on Antennas and Propagation*, vol. 48, No. 1, January 2000, pp. 19-24.

[13] T. P. Montoya and G. S. Smith, "Vee Dipoles with Resistive Loading for Short-Pulse Ground-Penetrating Radar," *Microwave and Optical Technology Lett*, vol. 13, No. 3, pp. 132-137, Oct. 1996.

[14] C. C. Chen, "A New Ground Penetrating Radar Antenna Design – The Horn-Fed Bowtie (HFB)," *AMTA'97*, vol. XXII, pp. 67-74.

[15] C. Nguyen, J.S. Lee and J.S. Park, "Ultra-Wideband Microstrip Quasi-Horn Antenna," *Electronics Letters*, Vol. 37, No. 12, 7th Jun. 2001, pp. 731-732.

[16] C. Leat, Private Correspondent with the Author 30th Oct. 2001.

[17] B. Scheers, M. Acheroy, A.V. Vorst, "Time domain simulation and characterisation of TEM horns using a normalised impulse response," *IEE Proceedings: Microwave Antennas Propag.*, vol. 147, No. 6, Dec 2000, pp. 463-468.

[18] I. White, "Balanced to Unbalanced Transformers," *Radio Communications*, Vol. 65, No. 12, Dec 1989, pp. 39-42.

[19] Mini-Circuits, "RF Transformers, Wideband," http://www.minicircuits.com/dg02-208.pdf (current Nov. 1, 2001).

[20] K.L. Shlager, G.S. Smith and J.G. Maloney, "Accurate Analysis of TEM Horn Antennas for Pulse Radiation," *IEEE Transactions on Electromagnetic Compatibility*, vol. 38, No. 3, Aug. 1996, pp. 414-423.

[21] E.O. Hammerstad and O. Jensen, "Accurate models for microstrip computer-aided design," *IEEE Int. Microwave Symp. Dig*., pp.407-409, 1980.

[22] D.M. Pozar, *Microwave Engineering, Second Edition*, John Wiley & Sons Inc, 1998.

[23] C.A. Balanis, *Antenna Theory: Analysis and Design*, John Wiley & Sons Inc, 1997.

[24] F.T Ulaby, *Fundamentals of Applied Electromagnetics*, Prentice Hall, 1999.

[25] J. D. Taylor, *Introduction to Ultra-Wideband Radar Systems*. Orlando, FL: CRC, 1995.

[26] J.D. Kraus, *Antennas*, 2nd edition, McGraw-Hill, New York, 1988.